Polymer Process Partitioning: Extruding Plastic Pipe

By

Chaimongkol Saengow

A thesis submitted to the Graduate Program in Chemical Engineering in conformity with the requirements for the Degree of Doctor of Philosophy.

Queen's University

Kingston, Ontario, Canada

September 2016

Abstract

When plastic pipe is solidified, it proceeds through a long cooling chamber. Inside this chamber, inside the hollow extrudate, the plastic is molten, and this inner surface solidifies last. Sag, the flow due to the self-weight of the molten plastic, then happens in this cooling chamber, and sometimes, thickened regions (called *knuckles*) arise in the lower quadrants, especially of large diameter thick-walled pipes. To compensate for sag, engineers normally shift the die centerpiece downward. This thesis focuses on the consequences of this decentering. Specifically, when the molten polymer is viscoelastic, as is normally the case, a downward lateral force is exerted on the mandrel. Die eccentricity also affects the downstream axial force on the mandrel. These forces govern how rigidly the mandrel must be attached (normally, on a spider die). We attack this flow problem in eccentric cylindrical coordinates, using the Oldroyd 8-constant constitutive model framework. Specifically, we revise the method of Jones (1964), called polymer process partitioning. We estimate both axial and lateral forces. We develop a corresponding map to help plastics engineers predict the extrudate shape, including extrudate knuckles. From the mass balance over the postdie region, we then predict the shape of the extrudate entering the cooling chamber. We further include expressions for the stresses in the extruded polymer melt. We include detailed dimensional worked examples to show process engineers how to use our results to design pipe dies, and especially to suppress extrudate knuckling.

Statement of Originality

I hereby certify that all of the work described within this thesis is the original work of the author. Any published (or unpublished) ideas and/or techniques from the work of others are fully acknowledged in accordance with the standard referencing practices.

Chaimongkol Saengow

September, 2016

Acknowledgment

We thank the Royal Golden Jubilee Program of the Thailand Research Fund for a grant (Contract No. PHD/0116/2554). The financial support from Rajamangala University of Technology Lanna is also appreciated. A.J. Giacomin is indebted to the Faculty of Applied Science and Engineering of Queen's University at Kingston, for its support through a Research Initiation Grant (RIG). This thesis was undertaken, in part, thanks to support from the Canada Research Chairs program of the Government of Canada for the Natural Sciences and Engineering Research Council of Canada (NSERC) Tier 1 Canada Research Chair in Rheology. This thesis was also undertaken, in part, thanks to support from the Discovery Grant program of the Natural Sciences and Engineering Research Council of Canada (NSERC).

We thank Prof. Jessada Tariboon of Faculty of Applied Science of King Mongkut's University of Technology North Bangkok, Thailand, and Mr. Peter H. Gilbert of the Chemical Engineering Department of Queen's University, Canada, for their helpful discussion. We thank Dean Sandra M. den Otter and Ms. Monica Corbett of School of Graduate Studies of Queen's, and Prof. Petch Jearanaisilawong of Graduate College of KMUTNB for their help on cotutelle agreement and MOU between Queen's and KNUTNB. We thank Prof. Aristides Docoslis of Chemical Engineering Department for his help on course load reduction at Queen's University. We thank Prof. Niwat Moonpa of Rajamangala University of Technology Lanna for his endeavor on offering us the great scholarship. We are indebted to Prof. P.R. Williams and Dr. D.J. Curtis of the

College of Engineering, Swansea University for their generous help with our literature review.

CONTENTS

Abstract ii

Statement of Originality iii

Acknowledgment iv

List of Figures viii

List of Tables xii

Chapter 1 Introduction 1

Chapter 2 Literature Review and Background 14

2.1 Eccentric Cylindrical Coordinates System 16

2.2 Oldroyd Constitutive Equation 18

2.2.1 Oldroyd Model 19

2.2.2 Oldroyd Model Constants 20

Chapter 3 Polymer Process Partitioning 29

3.1 Analytical Solution Method 31

3.2 Form of the Solutions 34

Chapter 4 Extrusion Die Analysis 37

4.1 Velocity Profile 37

4.1.1 Validation 45

4.2 Extrudate Shape 46

4.3 Shear Stress in Die Annulus 50

4.4 Axial Force on Mandrel 52

4.5 Lateral Force on Mandrel 54

4.6 Worked Example 57

Chapter 5 Extrudate Knuckling from Viscoelasticity 80

5.1 Extrudate Knuckling 81

5.2 Postdie Region 84

5.3 Results 85

5.4 Worked Example 87

Chapter 6 Conclusion 95

References 98

Appendix I. Solving Eq. (68) 112

Appendix II. $C_{mn,\ell}$ 118

Appendix III. $\phi'(\xi)$ and $\psi'(\xi)$ 125

Appendix IV. Relationship between θ and $\tilde{\theta}$ 130

List of Figures

Figure 1: Pipe extrusion line. 5
Figure 2: End view of pipe extrusion die defining the die dimensions. 6
Figure 3: Side view of pipe extrusion die (left), defining the die dimensions, and the postdie region (right). The mandrel and barrel surfaces correspond to $\xi = \xi_i$ and $\xi = \xi_o$. Solid-body motion, $v_z(\xi,\theta) = V$, in the cooling chamber (right). 7
Figure 4: Eccentric cylindrical coordinates showing the circles of constant eccentric radial coordinate (**black**), ξ, and the circles of constant eccentric angular coordinate (**green**), θ. **Cyan** example between $\xi = 0.2$ and $\xi = 0.4$. 8
Figure 5: Differential volume element of the molten plastic in eccentric cylindrical coordinates (cyan). Edges of differential surface element through which melt flows labeled $\left[a/\left(1+\xi^2-2\xi\cos\theta\right)\right]d\xi$ and $\left[a\xi/\left(1+\xi^2-2\xi\cos\theta\right)\right]d\theta$. Cylindrical shell of constant eccentric cylindrical radial coordinate ξ parallels $z-$axis, and intersects $x-$axis at $x = a/\left(1-\xi^2\right)$. This cylindrical shell contains surface element whose edges are dashed and labeled $\left[a\xi/\left(1+\xi^2-2\xi\cos\theta\right)\right]d\theta$ and dz. 9
Figure 6: Sag without knuckling. 10
Figure 7: Knuckling from sag (slump). Δ and Δ_p are the thickness of the extrudate that leaving the die, and entering the cooling chamber. 11
Figure 8: The shifted Cartesian coordinates, $(\tilde{x},\tilde{y})$, *versus* the Cartesian coordinates in Figure 4, (x,y). The origin of the cylindrical coordinates, $(r,\tilde{\theta})$, is located at $(x,y) = \left(a\xi/\left[1-\xi^2\right],0\right)$. 12
Figure 9: Measured wall thickness distribution of pipe with knuckles (**red**) with ten specific angular positions, for both eccentric cylindrical, θ, [Table 4] and cylindrical, $\tilde{\theta}$, coordinates. **Black** circles are drawn using $(\xi_i,\xi_o) = (0.0592, 0.0740)$ 13
Figure 10: Dimensionless shear stress *versus* Weissenberg number with curves of constant $\sigma = \frac{1}{100}, \frac{1}{9}, \frac{1}{4}, 1$ from bottom to top [Eq. (33)]. **Blue** curve (second from the bottom) shows the critical value of σ for shear-stress monotonicity [Eq. (34)]. 27
Figure 11: Dimensionless viscosity curves for shear thinning ($\sigma = \frac{1}{2}, \frac{3}{4}$), Newtonian ($\sigma = 1$) and shear thickening ($\sigma = \frac{5}{4}, \frac{3}{2}$) behaviors. **Blue** dots indicate inflections given by Eq. (37). 28
Figure 12: ξ_i and ξ_o *versus* aspect ratio, $\kappa \equiv R_i/R_o$ with curves of constant ϵ 63

Figure 13: The effectiveness of our rapid convergence approximation [Eq. (88)] (**blue**) that improved upon the Jones [16] truncation [Eq. (83)] (**red**) to the Newtonian contribution to the velocity profile. The dashed **black** curves are the exact expression [Eq. (75)]. 64

Figure 14: For shear-thinning fluid ($\sigma = \frac{1}{2}$, $S = \frac{1}{5}$), dimensionless axial velocity profiles, $\breve{v}_z$ *versus* ξ, around the eccentric annulus (curves of constant eccentric angular coordinate $\theta = 0, \frac{1}{6}\pi, \frac{1}{3}\pi, \frac{2}{3}\pi, \frac{5}{6}\pi, \pi$ from top to bottom) for the particular die shape $\xi_i = \frac{1}{5}$ and $\xi_o = \frac{2}{5}$. **Black** indicates ours [Eq. (62) with Eqs. (75) and (92)] and **red**, Jones's (Eq. (58) in [16] with Eqs. (49)-(51) and (53)-(57) in [16]). Discrepancies illustrate improvement from rapid convergence approximation [Eq. (88)]. 65

Figure 15: For Newtonian fluid ($\sigma = 1$, $S = \frac{1}{5}$), dimensionless axial velocity profiles, $\breve{v}_z$ *versus* ξ, around the eccentric annulus (curves of constant eccentric angular coordinate $\theta = 0, \frac{1}{6}\pi, \frac{1}{3}\pi, \frac{2}{3}\pi, \frac{5}{6}\pi, \pi$ from top to bottom) for the particular die shape $\xi_i = \frac{1}{5}$ and $\xi_o = \frac{2}{5}$. **Black**, ours [Eq. (62) with Eqs. (75) and (92)] closely matched **red**, Jones's (Eq. (58) in [16] with Eqs. (49)-(51) and (53)-(57) in [16]). 66

Figure 16: For shear-thickening fluid ($\sigma = \frac{3}{2}$, $S = \frac{1}{5}$), dimensionless axial velocity profiles, $\breve{v}_z$ *versus* ξ, around the eccentric annulus (curves of constant eccentric angular coordinate $\theta = 0, \frac{1}{6}\pi, \frac{1}{3}\pi, \frac{2}{3}\pi, \frac{5}{6}\pi, \pi$ from top to bottom) for the particular die shape $\xi_i = \frac{1}{5}$ and $\xi_o = \frac{2}{5}$. **Black** indicates ours [Eq. (62) with Eqs. (75) and (92)] and **red**, Jones's (Eq. (58) in [16] with Eqs. (49)-(51) and (53)-(57) in [16]). Discrepancies illustrate improvement from rapid convergence approximation [Eq. (88)]. 67

Figure 17: For shear-thinning fluid ($\sigma = \frac{1}{2}$, $S = \frac{1}{5}$), dimensionless axial velocity profiles, $\breve{v}_z$ *versus* ξ, around the eccentric annulus (curves of constant eccentric angular coordinate $\theta = 0, \frac{1}{6}\pi, \frac{1}{3}\pi, \frac{2}{3}\pi, \frac{5}{6}\pi, \pi$, top to bottom) for the particular die shape $\xi_i = \frac{1}{5}$ and $\xi_o = \frac{3}{5}$. **Black** indicates ours [Eq. (62) with Eqs. (75) and (92)] and **red**, Jones's (Eq. (58) in [16] with Eqs. (49) through (51) and (53)-(57) in [16]). Discrepancies illustrate improvement from rapid convergence approximation [Eq. (88)]. 68

Figure 18: For Newtonian fluid ($\sigma = 1$, $S = \frac{1}{5}$), dimensionless axial velocity profiles, $\breve{v}_z$ *versus* ξ, around the eccentric annulus (curves of constant eccentric angular coordinate $\theta = 0, \frac{1}{6}\pi, \frac{1}{3}\pi, \frac{2}{3}\pi, \frac{5}{6}\pi, \pi$ from top to bottom) for the particular die shape $\xi_i = \frac{1}{5}$ and $\xi_o = \frac{3}{5}$. **Black**, ours [Eq. (62) with Eqs. (75) and (92)] closely matched **red**, Jones's (Eq. (58) in [16] with Eqs. (49) through (51) and (53) through (57) in [16]). 69

Figure 19: For shear-thickening fluid ($\sigma = \frac{3}{2}$, $S = \frac{1}{5}$), dimensionless axial velocity profiles, $\breve{v}_z$ *versus* ξ, around the eccentric annulus (curves of constant eccentric angular coordinate $\theta = 0, \frac{1}{6}\pi, \frac{1}{3}\pi, \frac{2}{3}\pi, \frac{5}{6}\pi, \pi$ from top to bottom) for the particular die shape $\xi_i = \frac{1}{5}$ and $\xi_o = \frac{3}{5}$. **Black** indicates ours [Eq. (62) with Eqs. (75) and (92)] and **red**, Jones's [Eq. (58) in [16] with Eqs. (49) through (51) and (53) through (57) in [16]]. Discrepancies illustrate improvement from rapid convergence approximation [Eq. (88)]. 70

Figure 20: Dimensionless speed, $\breve{v}_z$, over the pipe cross section (30 contours of constant $\breve{v}_z$). Oldroyd 8-constant fluids: shear-thinning, $\sigma = \frac{1}{2}$ (left) *versus* Newtonian, $\sigma = 1$ (right). $S = \frac{1}{20}$, $\xi_i = \frac{1}{10}$ and $\xi_o = \frac{1}{5}$. The **black** near-wall regions are nearly motionless, and the **red**, highest speed ($\breve{v}_{z,\max} = 9.77\times10^{-3}$ for $\sigma = \frac{1}{2}$, $\breve{v}_{z,\max} = 9.45\times10^{-3}$ for $\sigma = 1$). 71

Figure 21: Dimensionless speed, $\breve{v}_z$, over the pipe cross section (30 contours of constant $\breve{v}_z$). Oldroyd 8-constant fluids: shear thickening, $\sigma = \frac{3}{2}$ (left) *versus* Newtonian, $\sigma = 1$ (right). $S = \frac{1}{20}$, $\xi_i = \frac{1}{10}$ and $\xi_o = \frac{1}{5}$. The **black** near-wall regions are nearly motionless, and the **red**, highest speed ($\breve{v}_z = 9.14\times10^{-3}$ for $\sigma = \frac{3}{2}$, $\breve{v}_z = 9.45\times10^{-3}$ for $\sigma = 1$). 72

Figure 22: Comparison between our dimensionless axial velocity profiles and well-known solution at evaluates at $\theta = 0$ (corresponding to $\beta = \pi$ in Eq. (25) of [37]) for die shape $R_i = 80\text{cm}$, $R_o = 100\text{cm}$ and $\delta = 3.5\text{cm}$ for Newtonian fluid $\sigma = 1$. **Black**, ours and **Blue**, well-known solution. Slight discrepancy due to our improvement upon the lubrication approximation. 73

Figure 23: Newtonian, $\breve{Q}_0$ (**blue**), and non-Newtonian variable, $\breve{Q}_1$ (**green**), contributions to volumetric flow rate *versus* ξ_i with $\xi_o = 0.02, 0.04, 0.06, 0.08, 0.10$ isopleths [Eqs. (123) and (124)]. 74

Figure 24: Newtonian, $\breve{Q}_{\theta,0}(0)$ (**blue**), and non-Newtonian variable, $\breve{Q}_{\theta,1}(0)$ (**green**), contributions to volumetric flow rate evaluating at $\theta = 0$, *versus* ξ_i, with $\xi_o = 0.02, 0.04, 0.06, 0.08, 0.10$ isopleths [Eqs. (129) and (130)]. 75

Figure 25: Newtonian, $\breve{Q}_{\theta,0}(\pi)$ (**blue**), and non-Newtonian variable, $\breve{Q}_{\theta,1}(\pi)$ (**green**), contributions to volumetric flow rate evaluating at $\theta = \pi$, *versus* ξ_i, with $\xi_o = 0.02, 0.04, 0.06, 0.08, 0.10$ isopleths [Eqs. (129) and (130)]. 76

Figure 26: Newtonian, $\mathbb{S}_0$ (**blue**), and non-Newtonian variable, $\mathbb{S}_1$ (**green**), contribution to maximum shear stress *versus* ξ_i, with $\xi_o = 0.02, 0.04, 0.06, 0.08, 0.10$ isopleths [Eqs. (139) and (140)]. 77

Figure 27: Newtonian, $\mathbb{F}_0$ (**blue**), and non-Newtonian variable, $\mathbb{F}_1$ (**green**), contribution to axial force *versus* ξ_i, with $\xi_o = 0.02, 0.04, 0.06, 0.08, 0.10$ isopleths [Eqs. (148) and (149)]..... 78
Figure 28: Newtonian, χ_0 (**blue**), and non-Newtonian variable, χ_1 (**green**), contribution to lateral force coefficient *versus* ξ_i, with $\xi_o = 0.02, 0.04, 0.06, 0.08, 0.10$ isopleths [Eq. (162) and (163)]. 79
Figure 29: Thickness distribution of the extrudate entering the cooling chamber, $\Delta_p = R_{op} - R_{ip}$, (**blue**) predicted from Eq. (213) [with Eq. (193)] using $P = 8.46\times10^5\,\text{Pa/m}$, $\eta_0 = 9.6\,\text{MPa·s}$, $V = 1.98\times10^{-5}\,\text{m/s}$, $R_i = 0.351\,\text{m}$, $R_o = 0.44\,\text{m}$, $R_{op} = 0.44\,\text{m}$, $\delta = 0.0118\,\text{m}$, $\lambda_1 = 2.38\,\text{s}$, $\lambda_2 = \mu_0 = \mu_1 = \mu_2 = \nu_1 = \nu_2 = 0$ *versus* the die shape (**red**). 89
Figure 30: Newtonian contribution to the extrudate shape gradient. Four sets of increasing parametrized curves of ξ_i from top to bottom [Eq. (201)]. ξ_o is increasing from bottom to top..... 90
Figure 31: Non-Newtonian contribution to extrudate shape gradient. Four sets of increasing parametrized curves of ξ_i (top to bottom). ξ_o is increasing from bottom to top. Dashed curves are for the negative part of $-\partial\langle\breve{v}\rangle_{\theta,1}/\partial\theta$ [Eq. (202)]. 91
Figure 32: Knuckling suppression map of the critical values of $(1-\sigma)S$, $\mathbb{K}$, *versus* inner contour, ξ_i, parametrized with ξ_o [Eq. (205)]. **Black** dot illustrates the critical value for Figure 33. 92
Figure 33: Suppressing extrudate knuckles. **Blue** curves are the Newtonian (negative) contribution to extrudate shape gradient [Eq. (201)], and the **green** ones, non-Newtonian [Eq. (202)], using $(\xi_i, \xi_o) = (0.01, 0.02)$. Critical value is $\mathbb{K} = 0.00263$. Suppressing by decreasing $(1-\sigma)S$. Dashed curves are for the negative part of $-\partial\langle\breve{v}\rangle_{\theta,1}/\partial\theta$. 93
Figure 34: Average velocity of each slice θ *versus* eccentric angular position, θ, with curves of constant $(1-\sigma)S = 0.00557$, 0.02, 0.04, 0.06, 0.08 [Eq. (205)]. The smoothest curve, $(1-\sigma)S = \mathbb{K} = 0.00557$, represents the critical extrudate knuckling..... 94

List of Tables

Table 1: Dimensional Variables.....xiii
Table 2: Dimensionless Variables and Groups xvi
Table 3: Symbol Correspondence between this Thesis and Jones [16].....xix
Table 4: Solid pipe thickness profile (see APPENDIX E of [7]). 4
Table 5: Literature on Analytical Solutions for Flow between Straight Eccentric Cylinders. 25
Table 6: Models included in the Oldroyd 8-constant model (see TABLE 8.1-1 of [31] and TABLE 7.3-2 of [32]). 26

Table 1: Dimensional Variables

Name	Unit	Symbol	Ref.
Any coordinates, i-th		x_i	(18)
Any tensor, ik-th component		b_{ik}	(18)
Area on mandrel per unit length	L	Z	(152)
Area, $\xi\theta-$plane	L^2	$A_{\xi\theta}$	(13)
Area, $\theta z-$plane	L^2	$A_{\theta z}$	(14)
Area, slice $\tilde{\theta}$ of each extrudate	L^2	$A_{\mathrm{e}\tilde{\theta}}$	(209)
Area, slice $\tilde{\theta}$ of each postdie extrudate that entering cooling chamber	L^2	$A_{\mathrm{p}\tilde{\theta}}$	(142)
Axial force	ML/t^2	F_z	(142)
Axial velocity	L/t	v_z	(59)
Boltzmann constant	ML^2/t^2T	k	(52)
Cartesian coordinates	L	x, y, z_{C}	Figure 3, Figure 4
Characteristic time, rigid dumbbell model	t	λ	(52)
Characteristic time, elastic dumbbell model	t	λ_H	(53)
Characteristic velocity	L/t	$W \equiv a^2P/4\eta_0$	(59)
Confocal length	L	a	(7)
Corotational derivative	t^{-1}	$\mathscr{D}/\mathscr{D}t$	(18)
Crossover angular frequency	t^{-1}	ω_c	Section 4.6
Density	M/L^3	ρ	Section 4.6
Die land length	L	L	Figure 3
Eccentric cylindrical coordinate, axial direction	L	z	Figure 3
Eccentricity	L	δ	Figure 2
Extra stress tensor	M/Lt^2	τ_{ik}	(15)
First normal stress coefficient	M/L	$\Psi_1 \equiv (\tau_{11}-\tau_{22})/\dot{\gamma}^2$	(39)
First normal stress coefficient, zero shear rate	M/L	$\Psi_{10} \equiv 2\eta_0(\lambda_1-\lambda_2)$	(44)
Infinite shear rate viscosity	M/Lt	η_∞	(31)
Lateral force	ML/t^2	F_x	(150)

Magnitude of the rate of deforma-tion tensor, inflection point	t^{-1}	$\dot{\gamma}_{\mathrm{i}}$	(36)
Magnitude of the rate of deformation tensor	t^{-1}	$\dot{\gamma}$	(27)
Minus the imaginary part of complex viscosity	M/Lt	η''	Section 4.6
Molar concentration of dumbbells	L^{-3}	$\overline{n}$	(52)
Oldroyd coefficient	t	μ_0	(15)
Oldroyd coefficient	t	μ_1	(15)
Oldroyd coefficient	t	μ_2	(15)
Oldroyd coefficient	t	ν_1	(15)
Oldroyd coefficient	t	ν_2	(15)
Oldroyd coefficient, relaxation time	t	λ_1	(15)
Oldroyd coefficient, retardation time	t	λ_2	(15)
Oldroyd shear thickening constant	t^2	σ_2	(26)
Oldroyd shear thinning constant	t^2	σ_1	(25)
Pressure gradient in die land	M/Lt^2	$P \equiv -dp/dz$	(61)
Radius of curvature of the free extrudate	L	r_0	(132)
Radius, die barrel	L	R_o	Figure 2
Radius, die mandrel	L	R_i	Figure 2
Radius, postdie extrudate, entering cooling chamber	L	R_{ip}	(213)
Radius, postdie extrudate, entering cooling chamber	L	R_{op}	(213)
Rate of deformation tensor	t^{-1}	$\dot{\gamma}_{ik}$	(17)
Real part of complex viscosity	M/Lt	η'	Section 4.6
Scale factor, eccentric angular cylindrical coordinate	L	h_θ	(12)
Scale factor, eccentric radial cylindrical coordinate	L	h_ξ	(11)
Second normal stress coefficient	M/L	$\Psi_2 \equiv \left(\tau_{22} - \tau_{33}\right)/\dot{\gamma}^2$	(40)
Second normal stress coefficient, , zero shear rate	M/L	Ψ_{20}	(45)

Steady shear viscosity function	M/Lt	η	(24)
Steady shear viscosity, viscosity curve inflection	M/Lt	η_{i}	(37)
Steady shear viscosity, solvent viscosity	M/Lt	η_s	Remark to Table 6
Steady shear viscosity, polymer contribution	M/Lt	η_p	Remark to Table 6
Temperature	T	T	(52)
Thickness, extrudate	L	Δ	Figure 7
Thickness, postdie extrudate, entering cooling chamber	L	Δ_{p}	Figure 7
Total stress tensor	M/Lt^2	π_{ij}	(16)
Velocity, pipe take-off	L/t	V	Figure 3
Volumetric flow rate	L^3/t	Q	(118)
Vorticity tensor	t^{-1}	ω_{ij}	(19)
Zero shear viscosity	M/Lt	η_0	(15)

Legend: $M \equiv$ mass; $L \equiv$ length; $t \equiv$ time; $T \equiv$ temperature

Table 2: Dimensionless Variables and Groups

Name	Symbol	Ref.
Aspect ratio	$\kappa \equiv R_i / R_o$	(82)
Average velocity at angular position θ	$\langle \breve{v}_z \rangle_\theta$	(125)
Average velocity at angular position $\tilde{\theta}$	$\langle \breve{v}_z \rangle_{\tilde{\theta}}$	(210)
Average velocity at angular position θ, Newtonian contribution	$\langle \breve{v}_z \rangle_{\theta,0}$	(194)
Average velocity at angular position θ, non-Newtonian variable	$\langle \breve{v}_z \rangle_{\theta,1}$	(195)
Axial force	$\mathbb{F}$	(145)
Axial force, Newtonian contribution	$\mathbb{F}_0$	(148)
Axial force, non-Newtonian variable	$\mathbb{F}_1$	(149)
Axial velocity	$\breve{v}_z \equiv 4\eta_0 v_z / a^2 P$	(59)
Axial velocity, Newtonian contribution	v_0	(75)
Axial velocity, non-Newtonian variable	v_1	(92)
Axial velocity, non-Newtonian variable, particular solution, m-th group, n-th harmonic	$v_{1p,n}^{(m)}$	(97)-(103), (104)-(109), (110)-(115)
Complex conjugate of zeta	$\zeta^* \equiv \xi e^{-i\theta}$	(67)
Complex zeta	$\zeta \equiv \xi e^{i\theta}$	(66)
Constant, m-th group, n-th harmonic, ℓ-th element	$C_{n,\ell}^{(m)}$	(259)-(261), (262)-(267), (268)-(273)
Cylindrical coordinate, angular	$\tilde{\theta}$	Figure 8
Cylindrical coordinate, angular, extrudate knuckling.	$\tilde{\theta}_{\mathrm{K}}$	(207)
Drawdown ratio	$\mathrm{DDR} \equiv \langle \breve{v}_z \rangle_{\tilde{\theta}} / \breve{V}$	(214)
Dimensionless parameter in elastic dumbbell	b	(53)
Discrepancies between the left and right sides of Eq. (70)	ε	(70)
Eccentric angular cylindrical coordinate	θ	Figure 4
Eccentric angular cylindrical coordinate, extrudate knuckling.	θ_{K}	(208)
Eccentric radial cylindrical coordinate	ξ	Figure 4
Eccentric radial cylindrical coordinate, inner contour	ξ_i	(80)
Eccentric radial cylindrical coordinate, outer contour	ξ_o	(81)

Eccentricity	$\epsilon \equiv \delta / R_o$	(82)
Extrudate shape gradient	$\mathrm{ESG} \equiv \partial \langle \breve{v}_z \rangle_\theta / \partial \theta$	(196)
Flow rate at angular position θ	$\breve{Q}_\theta(\theta)$	(127)
Integration coefficient, Newtonian contribution, n-th harmonic	α_n	(77)
Integration coefficient of Jones, Newtonian contribution, n-th harmonic	$\alpha_{\mathrm{J}n}$	(85)
Integration coefficient, Newtonian contribution, n-th harmonic	β_n	(78)
Integration coefficient of Jones, Newtonian contribution, n-th harmonic	$\beta_{\mathrm{J}n}$	(86)
Integration coefficient, non-Newtonian variable, n-th harmonic	A_n	(95)
Integration coefficient, non-Newtonian variable, n-th harmonic	B_n	(96)
Kronecker delta	δ_{ik}	(16)
Lateral force	χ	(161)
Lateral force, Newtonian contribution	χ_0	(162)
Lateral force, non-Newtonian variable	χ_1	(163)
Lateral force, non-Newtonian variable, higher order term	χ_2	(164)
Non-Newtonian coefficient	$(1-\sigma)S$	(62)
Non-Newtonian coefficient, critical value	$\mathbb{K}$	Figure 32
Oldroyd constant ratio	$\sigma \equiv \sigma_2 / \sigma_1 = \eta_\infty / \eta_0$	(30),(31)
Order of the expansion of Eq. (58)	$\mathscr{o}$	(58)
Power-law index	n	(38)
Pressure gradient squared	$S \equiv \sigma_1 a^2 P^2 / 16 \eta_0^{\,2}$	(60)
Shear stress	$\mathbb{S} \equiv \sqrt{\sigma_1}\, \tau_{\xi z} / \eta_0$	(135)
Shear stress, maximum	$\mathbb{S}_{\mathrm{m}} \equiv \sqrt{\sigma_1}\, \tau_{\xi z,\mathrm{m}} / \eta_0$	(141)
Shear stress, maximum, Newtonian contribution	$\mathbb{S}_0$	(139)
Shear stress, maximum, non-Newtonian variable	$\mathbb{S}_1$	(140)
Spatial function of axial velocity, Newtonian contribution, n-th harmonic	ϕ_n	(76)
Spatial function of axial velocity of Jones, Newtonian contribution, n-th harmonic	$\phi_{\mathrm{J}n}$	(84)
Spatial function of axial velocity, non-Newtonian variable, n-th harmonic	ψ_n	(93)

Spatial function of axial velocity, non-Newtonian variable, n-th harmonic	$\psi_n^{(m)}$	(94)
Velocity gradient, n-th harmonic, Newtonian contribution	$K_n \equiv \phi_n'(\xi_i)$	(148)
Velocity gradient, n-th harmonic, non-Newtonian variable	$L_n \equiv \psi_n'(\xi_i)$	(149)
Velocity vector	$\breve{\mathbf{v}}$	(54)
Velocity, pipe take-off	$\breve{V} \equiv 4\eta_0 V / a^2 P$	(210)
Volumetric flow rate	$\breve{Q}$	(120)
Volumetric flow rate of wedge $d\theta$ at angular position θ, Newtonian contribution	$\breve{Q}_{\theta,0}(\theta)$	(129)
Volumetric flow rate of wedge $d\theta$ at angular position θ, non-Newtonian variable	$\breve{Q}_{\theta,1}(\theta)$	(130)
Volumetric flow rate, Newtonian contribution	$\breve{Q}_0$	(123)
Volumetric flow rate, non-Newtonian variable	$\breve{Q}_1$	(124)
Weissenberg number	$\mathrm{Wi} \equiv \sqrt{\sigma_1}\dot{\gamma}$	(28)
Weissenberg number, viscosity curve inflection	$\mathrm{Wi}_\mathrm{i} \equiv \sqrt{\sigma_1}\dot{\gamma}_\mathrm{i}$	(36)

Table 3: Symbol Correspondence between this Thesis and Jones [16]

Variable name	This thesis	Jones [16]
Axial velocity	v_z	w
Axial velocity, dimensionless	$\breve{v}_z$	w'
Axial velocity, Newtonian contribution	v_0	w_0
Axial velocity, non-Newtonian variable	v_1	w_1
Confocal length	a	d
Eccentric angular cylindrical coordinate	θ	φ
Eccentric radial cylindrical coordinate	ξ	r
Eccentricity	δ	h
Extra stress tensor	τ_{ij}	p'_{ij}
Inner contour	ξ_i	a
Magnitude of rate of strain tensor	$\dot{\gamma}$	γ
Magnitude of rate of strain tensor, dimensionless	$\breve{\gamma}$	γ'
Outer contour	ξ_o	b
Steady shear viscosity function	$\eta(\dot{\gamma})$	$F(\gamma)$

Chapter 1 Introduction

Extrusion dies are the metal channels that shape the cross section of extruded molten polymers. When plastic pipe is solidified, it proceeds through a long cooling chamber (see Figure 1). Inside the chamber, on the inner side of the extrudate, the plastic is molten, and this inner surface solidifies last. By *extrudate*, we mean the molten plastic that just emerged from the extrusion die, and the term *pipe* refers to the completely solidified extrudate. The flow due to sag of the molten plastic then happens inside this cooling chamber (and to thin on top). By *sag*, we mean the gravitational flow in the cooling chamber of the molten extrudate [1,2,3,4,5,6,7,8].

To compensate for sag, engineers normally shift the die centerpiece downward (see this illustrated in Figure 2 and Figure 3; [2,3,4,8,9,10,11,12,13,14], also sometimes gently rotate the extrudate [3,5]. For the former, engineers must decenter the mandrel laboriously *by trial* (see Figure 6). These trials are performed based on the thickness distributions on the cut sample. This thesis research can help shorten these trials, by providing equations [Eq. (131) with Eqs. (129)–(130)] for predicting the pipe shape at the cooling chamber entrance. This thesis aims to deepen our understanding of the flow of polymer melts through eccentric plastic pipe extrusion dies. Specifically, this thesis explores how viscoelasticity affects the (1) velocity profile, (2) extrudate shape, (3) residual stresses, (4) axial and lateral forces on the eccentric mandrel, and on (5) knuckle formation (knuckling). Since pipe is only as strong as its thinnest part, a non-

uniform extrudate shape wastes material. Pipe manufacture is thus preoccupied with perfecting extrudate shape.

Curiously, sometimes the pipe is thickest, not at the bottom, but elsewhere in its lower quadrants (see Figure 7; Fig. 1 and Fig. 6 of [8]). By *lower quadrants*, we mean, in cylindrical coordinates, where $\pi/2 \le \tilde{\theta} \le 3\pi/2$ (see Figure 8). These thickened sections in the lower pipe quadrants are called *knuckles*, and their formation, *knuckling* (or *slump* [2,6,7,8]). Knuckling must not be confused with sag (compare Figure 6 with Figure 7; also [15]). Whereas sag can reshape knuckled extrudate, sag can also itself knuckle extrudate that enters the cooling chamber without knuckles [2,6,7,8]. To be clear, *extrudate knuckling* refers to the molten extrudate, and not to the completely solidified extrudate, which we called pipe. Although numerical simulation of sag of eccentric extrudates does predict some knuckling, observed knuckling is far more pronounced (see Fig. 6 of [8]). By *pronounced knuckling*, we mean, where the thickness of the knuckle greatly exceed the bottom thickness. Pronounced knuckling is thus one of the great mysteries of plastic pipe manufacture.

Pipe knuckling has been attributed to sag of eccentric extrudates [2,6,7,8]. By *pipe knuckling*, we mean when completely solidified product has thickened sections in its lower quadrants. Although numerical simulation of sag of eccentric extrudates does qualitatively predict some knuckling, observed knuckling is normally far more pronounced (see Fig. 6 of [8]). Specifically, profiles predicted by sag alone over-predict the bottom thickness.

By pipe or extrudate *thickness*, we mean the radial distance measured from the outer shell to the inner shell along the radial cylindrical coordinate, centered on the outer cylinder (see Table 4 and Figure 9). Eq. (300) [Eq. (301)] relates the angular positions in cylindrical coordinates, $\tilde{\theta}$, to the angular position in eccentric cylindrical coordinates, θ [*vice versa*]. These relations can be used to transform a thickness distribution from one coordinate system to another.

This thesis focuses on the consequences of this decentering. Specifically, when the molten polymer is viscoelastic, as is normally the case, a downward lateral force, F_x, is exerted on the mandrel. The die eccentricity also affects the positive axial force on the mandrel, F_z (see Figure 2 through Figure 5, Table 1 and Table 2 for symbol definitions, both dimensional and dimensionless; see also Table 3). These forces govern the required rigidity for the mandrel attachment (on a *spider die*, normally a set of eight bolts).

Table 4: Solid pipe thickness profile (see APPENDIX E of [7]).

Angular position in eccentric cylindrical coordinates, θ [degrees]	Angular position in cylindrical coordinates, $\tilde{\theta}$ [degrees]	Thickness, Δ_p, (see Figure 7) [millimeters]
0.00	0.00	73.7
19.8	23.0	72.8
39.3	45.0	74.0
81.5	90.0	84.6
118	125	94.5
129	135	92.9
180	180	80.1
231	225	91.9
279	270	80.6
321	315	74.5

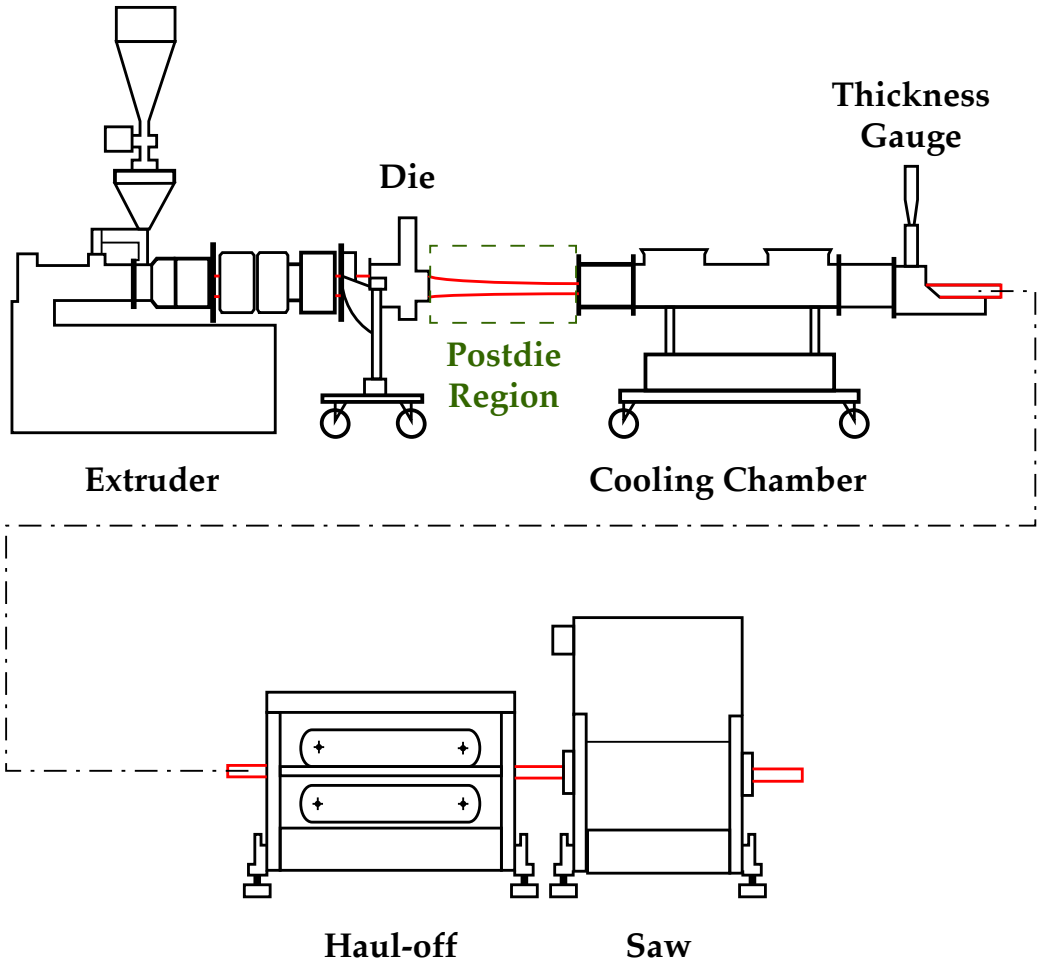

Figure 1: Pipe extrusion line.

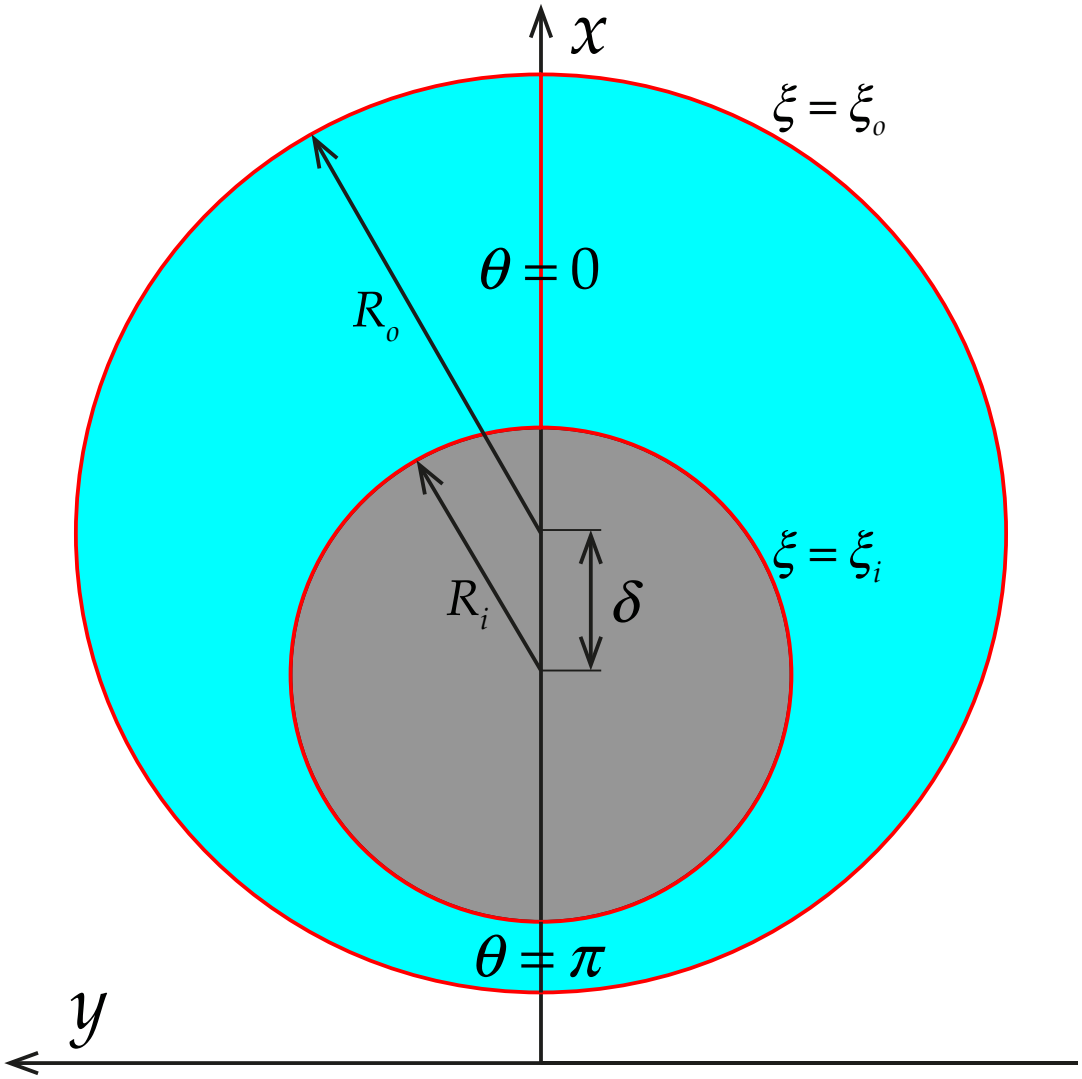

Figure 2: End view of pipe extrusion die defining the die dimensions.

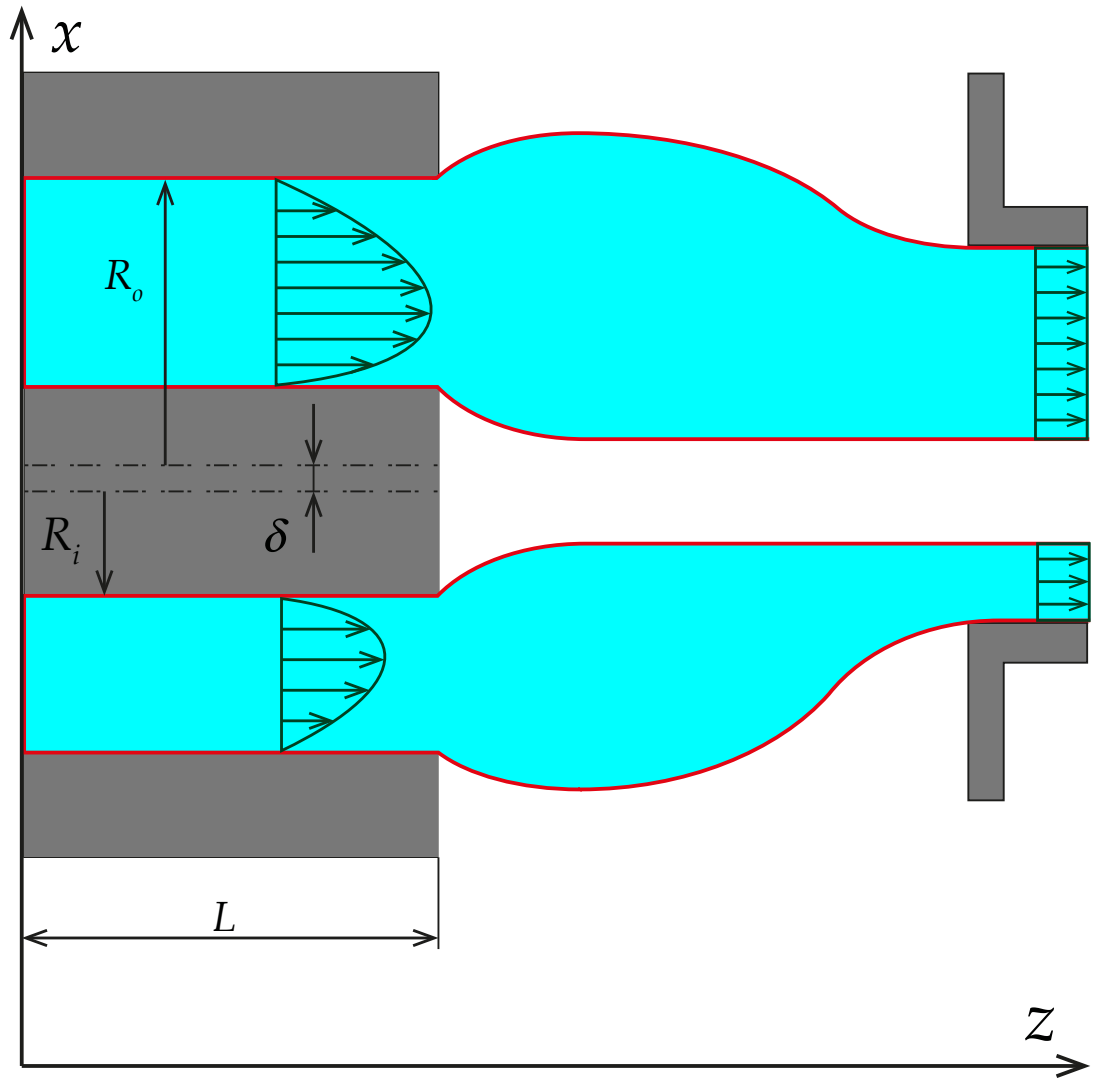

Figure 3: Side view of pipe extrusion die (left), defining the die dimensions, and the postdie region (right). The mandrel and barrel surfaces correspond to $\xi = \xi_i$ and $\xi = \xi_o$. Solid-body motion, $v_z(\xi,\theta) = V$, in the cooling chamber (right).

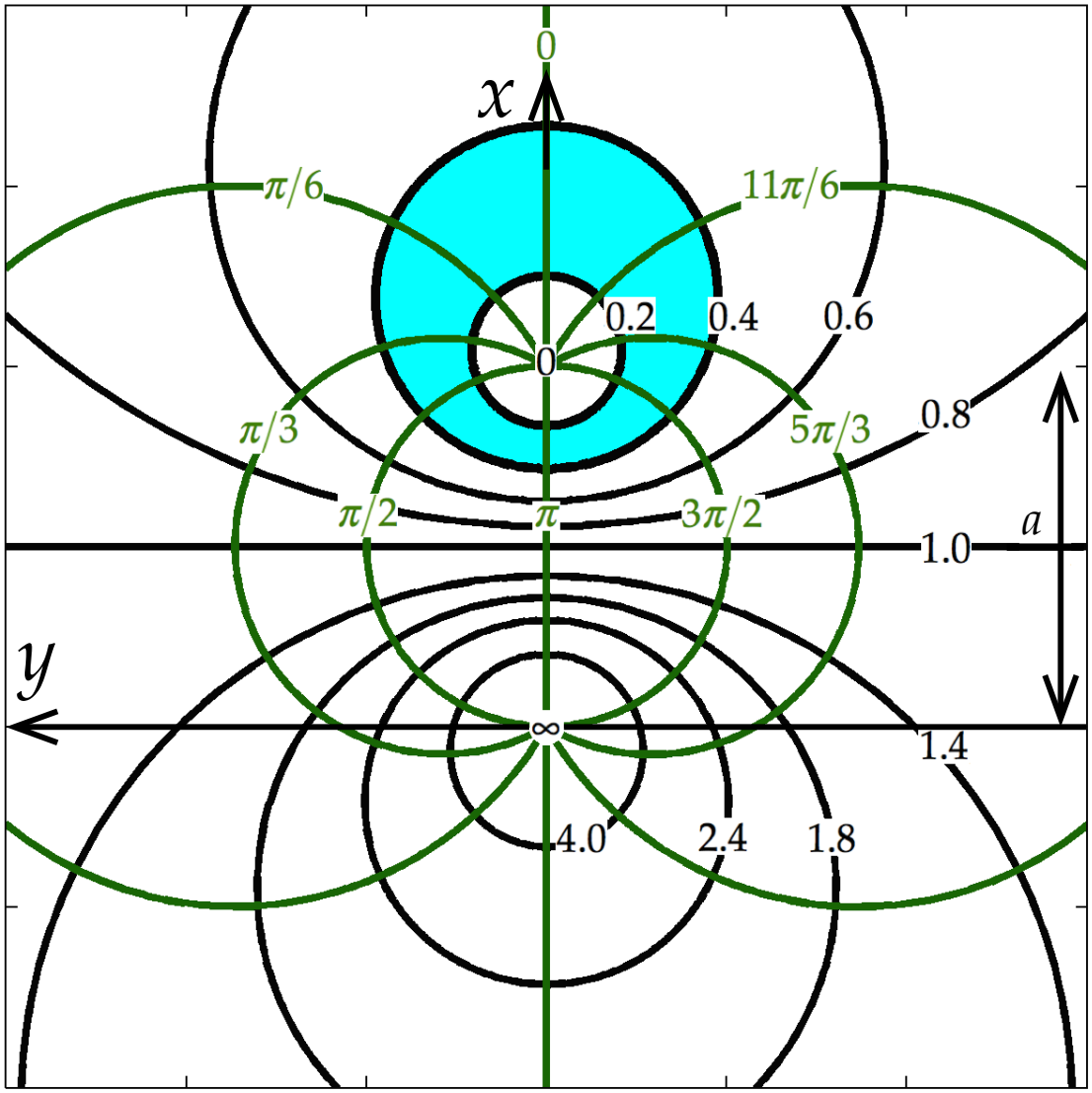

Figure 4: Eccentric cylindrical coordinates showing the circles of constant eccentric radial coordinate (**black**), ξ, and the circles of constant eccentric angular coordinate (**green**), θ. **Cyan** example between $\xi = 0.2$ and $\xi = 0.4$.

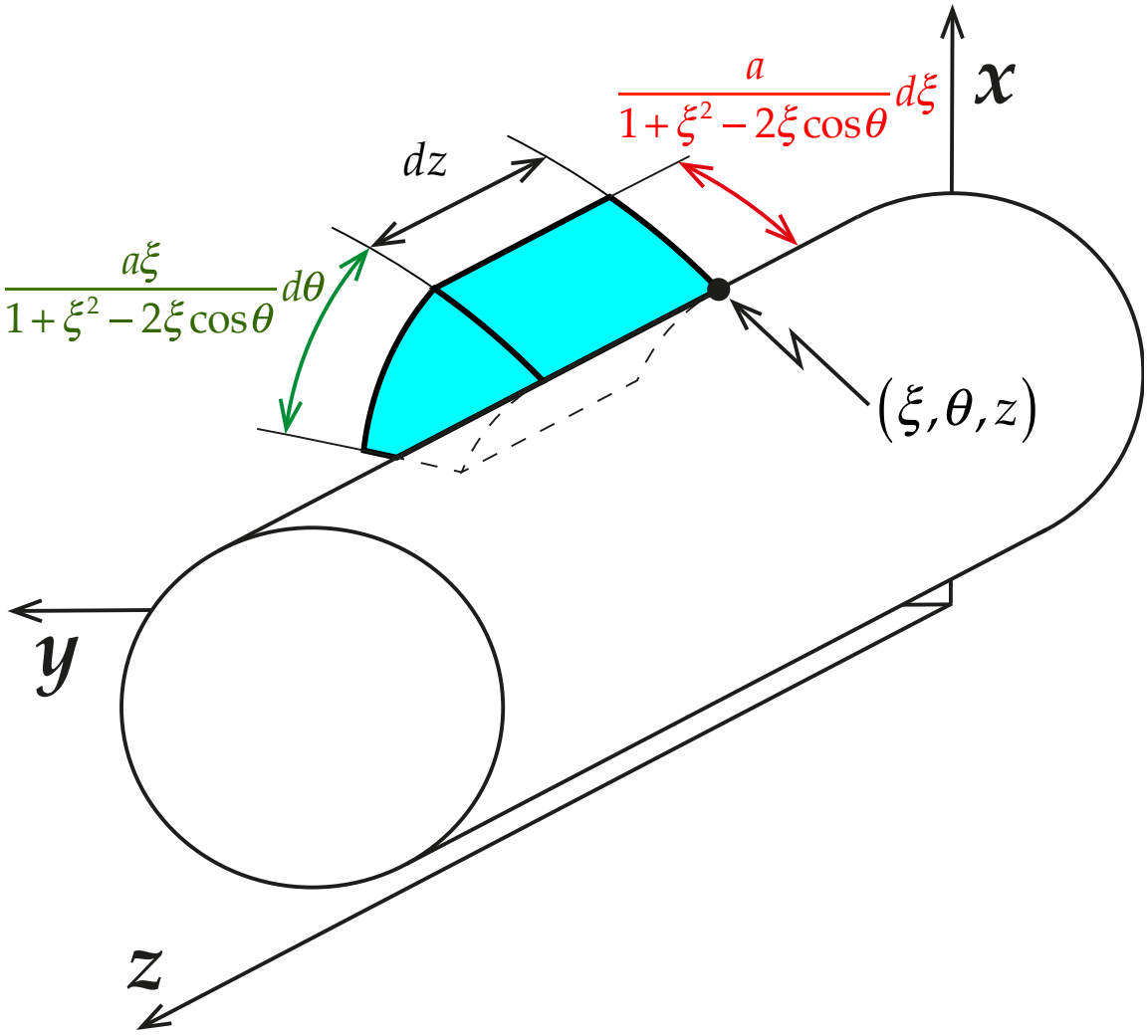

Figure 5: Differential volume element of the molten plastic in eccentric cylindrical coordinates (cyan). Edges of differential surface element through which melt flows labeled $\left[a/\left(1+\xi^2-2\xi\cos\theta\right)\right]d\xi$ and $\left[a\xi/\left(1+\xi^2-2\xi\cos\theta\right)\right]d\theta$. Cylindrical shell of constant eccentric cylindrical radial coordinate ξ parallels $z-$axis, and intersects $x-$axis at $x=a/\left(1-\xi^2\right)$. This cylindrical shell contains surface element whose edges are dashed and labeled $\left[a\xi/\left(1+\xi^2-2\xi\cos\theta\right)\right]d\theta$ and dz.

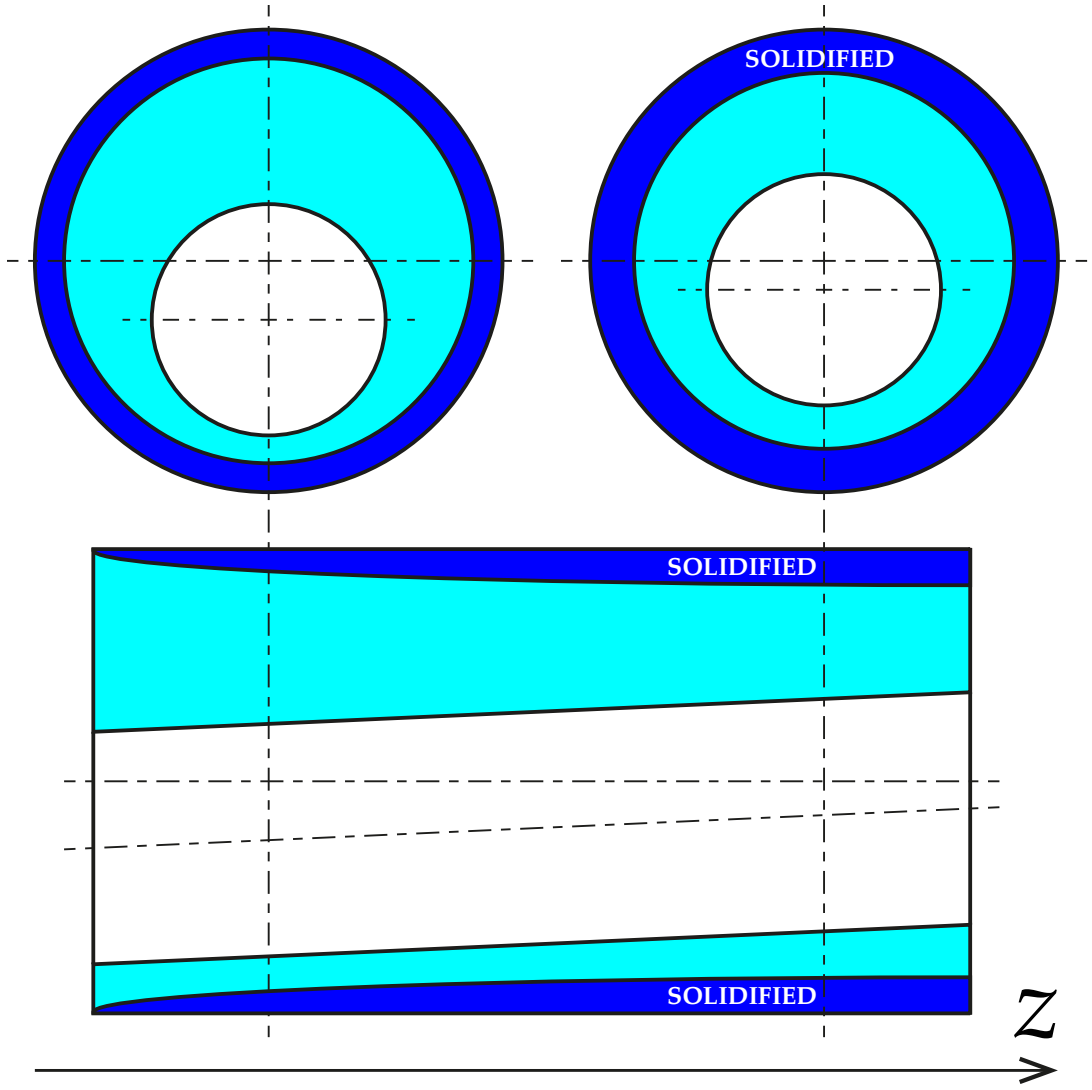

Figure 6: Sag without knuckling.

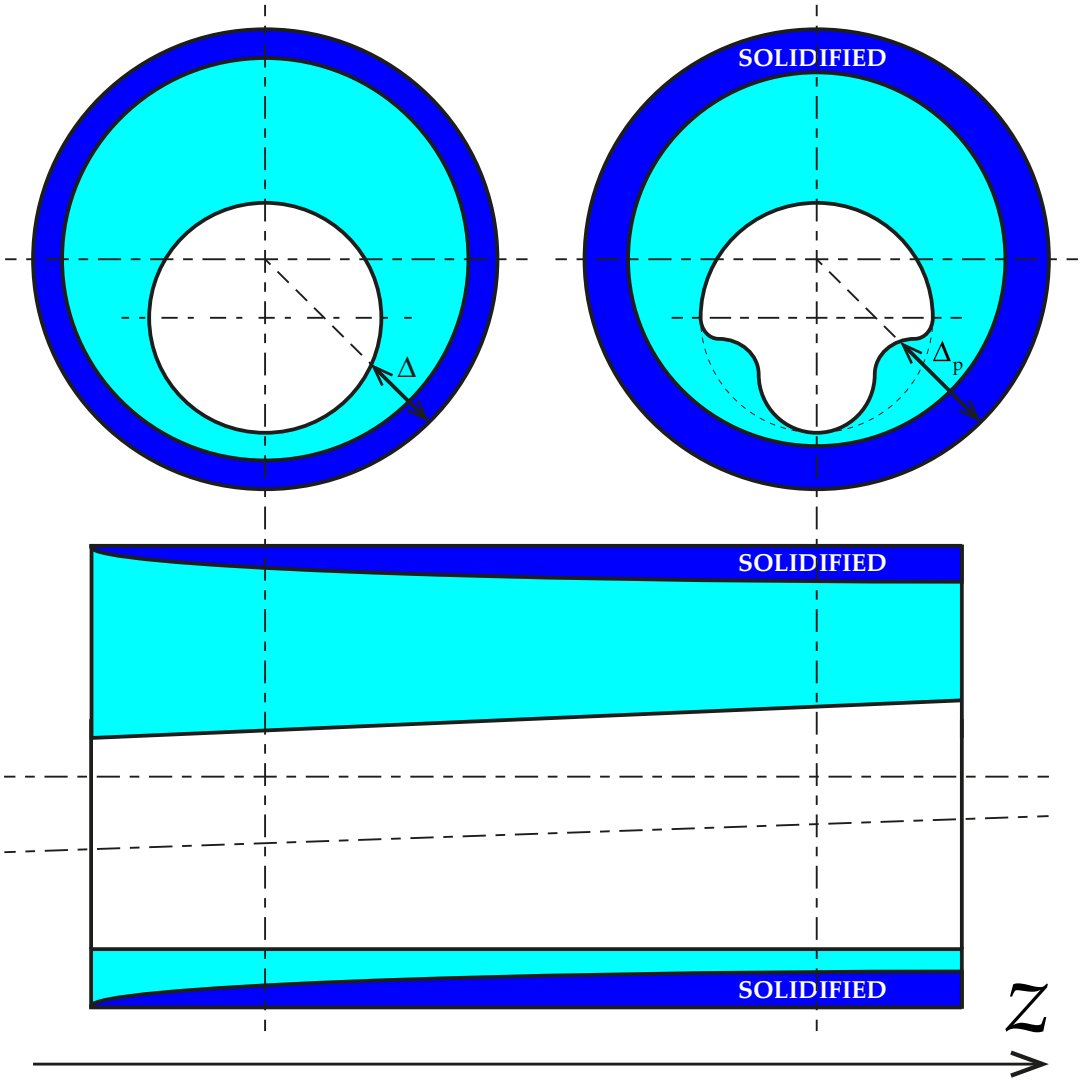

Figure 7: Knuckling from sag (slump). Δ and Δ_p are the thickness of the extrudate that leaving the die, and entering the cooling chamber.

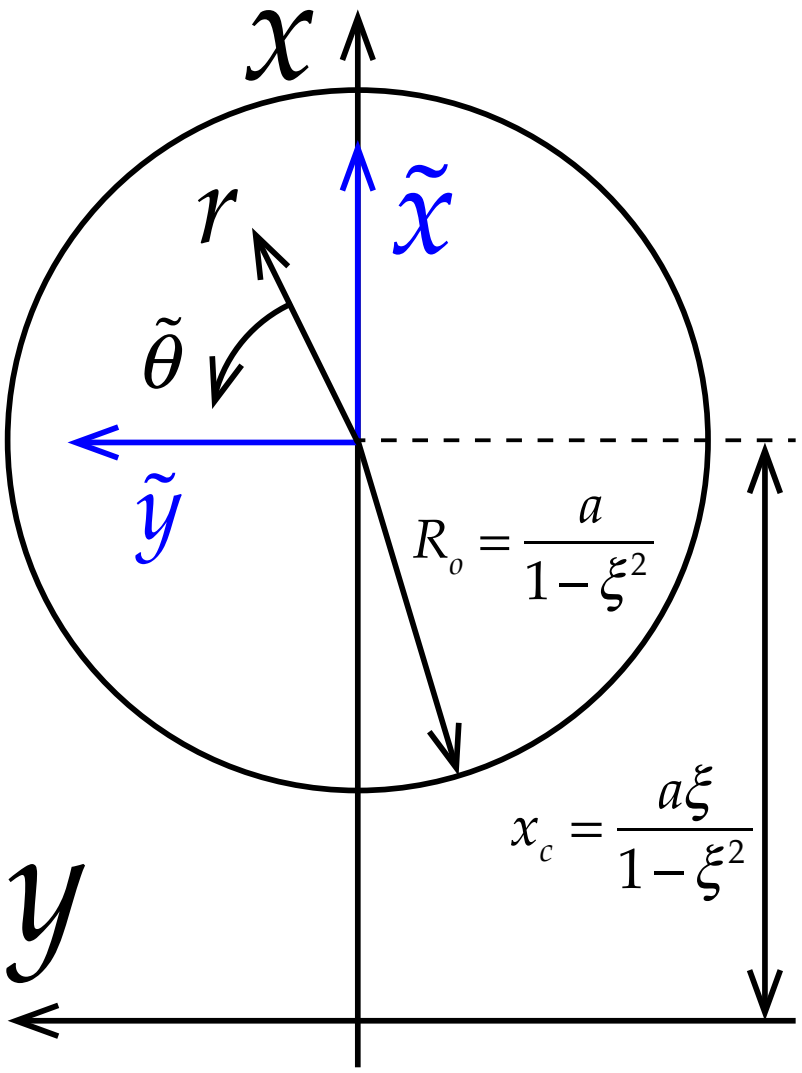

Figure 8: The shifted Cartesian coordinates, $(\tilde{x},\tilde{y})$, *versus* the Cartesian coordinates in Figure 4, (x,y). The origin of the cylindrical coordinates, $(r,\tilde{\theta})$, is located at $(x,y) = \left(a\xi/\left[1-\xi^2\right],0\right)$.

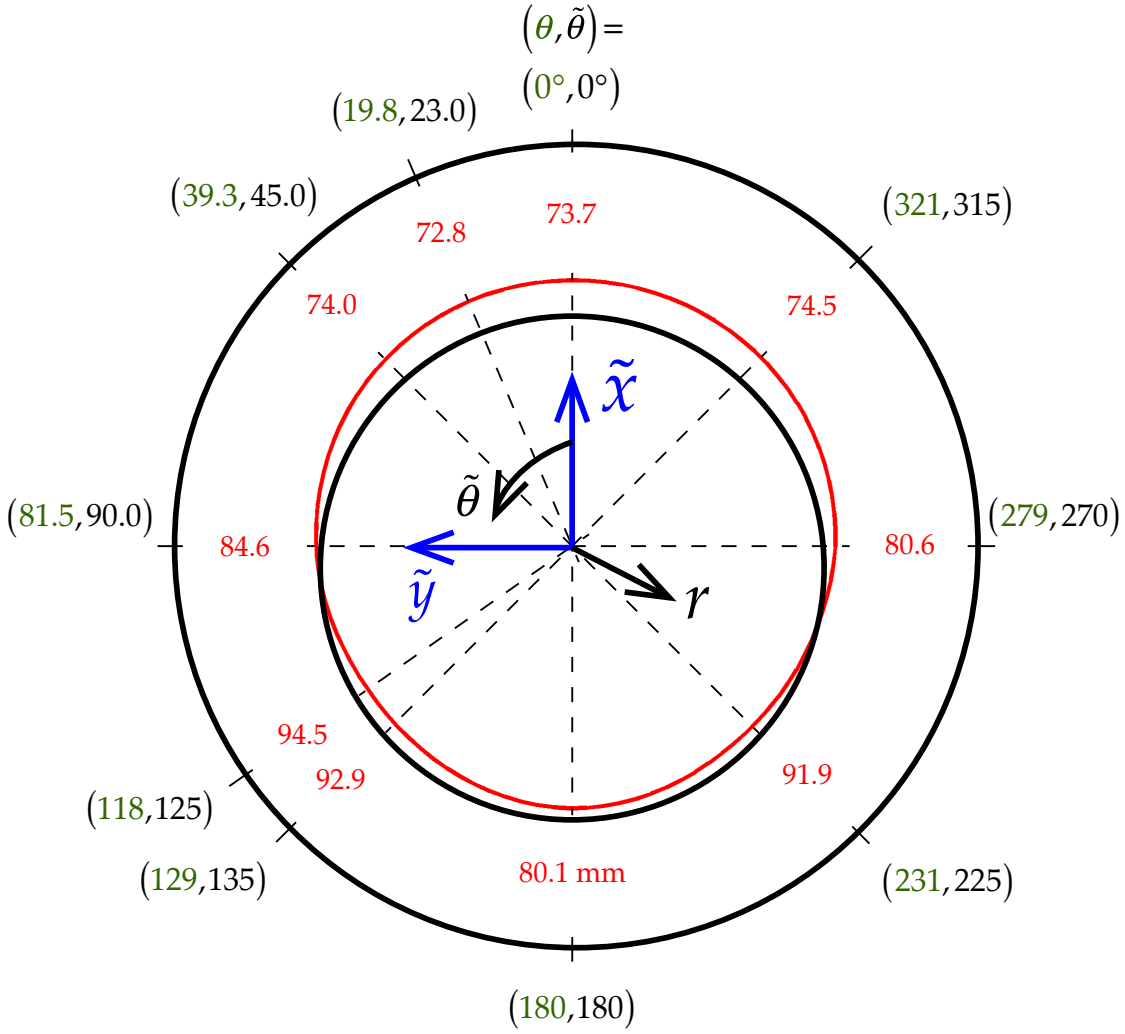

Figure 9: Measured wall thickness distribution of pipe with knuckles (**red**) with ten specific angular positions, for both eccentric cylindrical, θ, [Table 4] and cylindrical, $\tilde{\theta}$, coordinates. **Black** circles are drawn using $(\xi_i,\xi_o)=(0.0592,0.0740)$.

Chapter 2 Literature Review and Background

John Raymond Jones of Wales [16] pioneered a method for solving polymer-processing problems, specifically for the Oldroyd 8-constant fluid, by splitting the velocity field into its Newtonian and non-Newtonian parts. The method yields answers for the relevant polymer process features, including velocity, extrudate shape, stresses and forces. Each of these answers, split naturally into their Newtonian and non-Newtonian parts. These parts, in turn, arise with coefficients that just depend of the processing problem geometry. We call this method *polymer process partitioning* (see this discussed in 3.2 below). Curiously, we know of no polymer processing textbook treatment of the polymer process partitioning [16]. This method has been applied to the viscoelastic coating of an eccentric wire (with (Cases III and IV in [16]) or without (Cases I in [16]) pressure gradient), the extrusion of elliptical pipe [17,18], and also to extrusion from an eccentric annular pipe die (Cases II in [16]; [18]; Section 2. of [19]), and even to a corrugated wire coated through a corrugated die (see Section 3. of [19]; Section 2. of [20]). In the latter, we discovered an important opportunity to improve upon the method of Jones [16], an improvement that we call the rapid convergence approximation [see Eq. (88)]. For extrusion through curved eccentric annuli (be they circular [21] or elliptical [22,23]) or for flows along cylindrical boundaries [24], Jones and his coworkers abandoned polymer process partitioning.

In this thesis, we apply the polymer process partitioning approach, to arrive at our analytical solutions. The usefulness of this method appears to have been overlooked by the polymer processing community. We write this thesis not only

to benefit the professional mathematical physicists, but with sufficient detail to help graduate students arrive at their own analytical solutions for any polymer processing problem, at least some other flows between eccentric annuli, wire coating for example. Specifically, we would expect educators to use our work in both their research and teaching, and for their graduate students to train themselves from our analysis.

Table 5 summarizes and classifies previous analytical work on pressure-driven flow through eccentric annuli, and compares the present research to these contributions. With reference to column 2 of Table 5, only the Bingham and power-law entries are not special cases of the Oldroyd 8-constant model. Further to Table 5, for Newtonian fluids, secondary flows in the coating of elliptical wires (Section 2. [25]) and in the extrusion of the elliptical pipe (Section 3. [25]) and pressure-driven flow through curved eccentric annuli have also been investigated.

Pipe knuckling has been observed on extrusion lines producing large diameter thick-walled pipes when the extrusion die is eccentric [2,7,8]. Figure 9 illustrates the detailed example of pipe knuckling in large thick high-density polyethylene pipe. Note the thickened sections in the lower quadrants. When pipe knuckles arise, they can be a serious non-uniformity of thickness. Moreover, when large diameter pipe is made, from a new resin, it can take up to four attempts at start-up to get an acceptable thickness profile [26]; each attempt can waste up to 10 h and ten thousand pounds of pipe resin [27,28,29]. Pipe knuckling generally

worsens start-up, often to the point of no solution, and thus, to de-selection of otherwise desirable new pipe resins.

2.1 Eccentric Cylindrical Coordinates System

Eccentric cylindrical coordinates (illustrated in Figure 4) consist of two orthogonal sets of cylindrical shells. The first set is defined by the *eccentric radial coordinate*, ξ, and another, by the *eccentric angular coordinate*, θ. The transformations from Cartesian to eccentric cylindrical coordinates are given by (see Eqs. (73)–(75) of [30]):

$$x = a\frac{1-\xi\cos\theta}{1-2\xi\cos\theta+\xi^2} \tag{1}$$

$$y = a\frac{\xi\sin\theta}{1-2\xi\cos\theta+\xi^2} \tag{2}$$

$$z_C = z \tag{3}$$

or:

$$\xi = \frac{x^2+y^2-2ax+a^2}{x^2+y^2} \tag{4}$$

$$\theta = \arctan\left(\frac{ay}{x^2+y^2-ax}\right) \tag{5}$$

$$z = z_C \tag{6}$$

where the z coordinate is the flow direction (see Figure 3), and we call:

$$a \equiv \delta^{-1}\left(R_o^4+R_i^4+\delta^4-2R_i^2R_o^2-2R_i^2\delta^2-2R_o^2\delta^2\right)^{1/2} \tag{7}$$

the *dimensional confocal length*, and thus we define the *dimensionless confocal length* as:

$$f \equiv \frac{a}{R_0} \equiv \epsilon^{-1}\left(1+\kappa^4+\epsilon^4-2\kappa^2-2\kappa^2\epsilon^2-2\epsilon^2\right)^{1/2} \tag{8}$$

where R_i, R_o and δ are the mandrel radius, the extrusion die radius and the dimension eccentricity (see Figure 2 and Table 2 for variable definitions). The circles of constant ξ are given by:

$$\left(x-\frac{a}{1-\xi^2}\right)^2+y^2=\left(\frac{a\xi}{1-\xi^2}\right)^2 \tag{9}$$

and circles of constant θ, by:

$$x^2+\left(y-\tfrac{1}{2}a\cot\theta\right)^2=\left(\frac{a}{2\sin\theta}\right)^2 \tag{10}$$

To illustrate our eccentric cylindrical coordinates, we use Eqs. (9) and (10) to draw the circular cross-sections of cylindrical shells of constant ξ (black circles) and of constant θ (**green** circles) in Figure 4. Inside the eccentric annulus, the shells of constant ξ start through the origin of the eccentric cylindrical coordinate system (not to be confused with the origin of our corresponding Cartesian system). This origin is on the line $\xi=0$, that is, the line through positive focus, $x=a$. The shell of infinite radius, when $\xi=1$, is the plane. Inside the eccentric annulus, the cylindrical shells of constant θ start with the vertical half-plane ($\theta=0$) immediately above the line $\xi=0$, and the shell end with the vertical planar strip ($\theta=\pi$). Eccentric cylindrical coordinates are not to be

confused with bipolar cylindrical coordinates, which are also used for analyzing flow in eccentric annuli (see FIGURE A.7-1. In [31] or in [32], or *Fig. 3.* In [33], or Fig. P3.16 in [34] where ξ and θ have other meanings [35,36,37,38,39]).

We next illustrate our eccentric cylindrical differential volume element in Figure 5. Employing Eqs. (A.7-13) of [40] gives us the *scale factors* for coordinates ξ and θ:

$$h_{\xi} \equiv \frac{a}{1+\xi^2-2\xi\cos\theta} \tag{11}$$

$$h_{\theta} \equiv \frac{a\xi}{1+\xi^2-2\xi\cos\theta} \tag{12}$$

The differential area relevant to the axial flow rate is given by:

$$dA_{\xi\theta} = \frac{a^2\xi}{\left(1+\xi^2-2\xi\cos\theta\right)^2} d\xi d\theta \tag{13}$$

and the differential area relevant to the axial force on the mandrel, by:

$$dA_{\theta z} = \frac{a\xi}{1+\xi^2-2\xi\cos\theta} d\theta dz \tag{14}$$

We will use Eq. (13) in Subsection. 4.2 to get the axial flow rate, and Eq. (14) in Subsection. 4.4 to get the axial force on mandrel.

2.2 Oldroyd Constitutive Equation

In this thesis, we choose the Oldroyd 8-constant constitutive model for the extruded plastics. We choose this model for its rich diversity of special cases (see Chapter 1; also Table 6). Like Jones [16] before us and for simplicity, we follow

the notation and symbols of Oldroyd [41], with just a few modernizations. Table 3 lists correspondences between symbols used in the present work and those used by Jones [16].

2.2.1 Oldroyd Model

We write the Oldroyd 8-constant model as:

$$\begin{aligned}&\tau_{ik}+\lambda_1\frac{\mathscr{D}\tau_{ik}}{\mathscr{D}t}+\mu_0\tau_{jj}\dot{\gamma}_{ik}-\mu_1\left(\tau_{ij}\dot{\gamma}_{jk}+\tau_{jk}\dot{\gamma}_{ij}\right)+\nu_1\tau_{jl}\dot{\gamma}_{jl}\delta_{ik}\\&=2\eta_0\left(\dot{\gamma}_{ik}+\lambda_2\frac{\mathscr{D}\dot{\gamma}_{ik}}{\mathscr{D}t}-2\mu_2\dot{\gamma}_{ij}\dot{\gamma}_{jk}+\nu_2\dot{\gamma}_{jl}\dot{\gamma}_{jl}\delta_{ik}\right)\end{aligned} \tag{15}$$

where:

$$\pi_{ik}\equiv\tau_{ik}+p\delta_{ik} \tag{16}$$

and the rate-of-strain tensor is given by:

$$\dot{\gamma}_{ik}\equiv\frac{1}{2}\left(\frac{\partial v_k}{\partial x_i}+\frac{\partial v_i}{\partial x_k}\right) \tag{17}$$

and the corotational derivative is given by:

$$\frac{\mathscr{D}b_{ik}}{\mathscr{D}t}\equiv\frac{\partial b_{ik}}{\partial t}+v_j\frac{\partial b_{ik}}{\partial x_j}+\omega_{ij}b_{jk}+b_{ij}\omega_{jk} \tag{18}$$

where the vorticity tensor is given by:

$$\omega_{ik}\equiv\frac{1}{2}\left(\frac{\partial v_k}{\partial x_i}-\frac{\partial v_i}{\partial x_k}\right) \tag{19}$$

In Eq. (16), δ_{ik} is the *kronecker delta*. For convenience, we define every dimensional symbol in Table 1, and dimensionless ones in Table 2.

2.2.2 Oldroyd Model Constants

To deepen our understandings of the Oldroyd model constants, we first examine the model for any simple shear flow:

$$\left(1+\lambda_1\frac{\partial}{\partial t}\right)\tau_{yx}+\frac{1}{2}\left(\lambda_1+\mu_0-\mu_1\right)\tau_{xx}\dot{\gamma}-\frac{1}{2}\left(\lambda_1-\mu_0+\mu_1\right)\tau_{yy}\dot{\gamma}+\frac{1}{2}\mu_0\tau_{zz}\dot{\gamma} = \eta_0\left(1+\lambda_2\frac{\partial}{\partial t}\right)\dot{\gamma} \tag{20}$$

$$\left(1+\lambda_1\frac{\partial}{\partial t}\right)\tau_{xx}-\left(\lambda_1+\mu_1-\nu_1\right)\tau_{yx}\dot{\gamma}=-\eta_0\left(\lambda_2+\mu_2-\nu_2\right)\dot{\gamma}^2 \tag{21}$$

$$\left(1+\lambda_1\frac{\partial}{\partial t}\right)\tau_{yy}+\left(\lambda_1-\mu_1+\nu_1\right)\tau_{yx}\dot{\gamma}=\eta_0\left(\lambda_2-\mu_2+\nu_2\right)\dot{\gamma}^2 \tag{22}$$

$$\left(1+\lambda_1\frac{\partial}{\partial t}\right)\tau_{zz}+\nu_1\tau_{yx}\dot{\gamma}=\eta_0\nu_2\dot{\gamma}^2 \tag{23}$$

which, for steady shear flow, give the steady shear viscosity function as:

$$\frac{\eta(\dot{\gamma})}{\eta_0}=\frac{1+\sigma_2\dot{\gamma}^2}{1+\sigma_1\dot{\gamma}^2} \tag{24}$$

which matches Eq. (8) of [4] and Eq. (8.1-7) of [31] and where:

$$\sigma_1\equiv\lambda_1^2+\mu_0\left(\mu_1-\tfrac{3}{2}\nu_1\right)-\mu_1\left(\mu_1-\nu_1\right) \tag{25}$$

$$\sigma_2\equiv\lambda_1\lambda_2+\mu_0\left(\mu_2-\tfrac{3}{2}\nu_2\right)-\mu_1\left(\mu_2-\nu_2\right) \tag{26}$$

and where the magnitude of the rate of deformation tensor:

$$\dot{\gamma}\equiv\frac{\left(1-2\xi\cos\theta+\xi^2\right)}{a\xi}\sqrt{\left(\xi\frac{\partial v_z}{\partial\xi}\right)^2+\left(\frac{\partial v_z}{\partial\theta}\right)^2} \tag{27}$$

is obtained by substituting Eqs. (33a) of [16] and (33b) of [16] into Eq. (43) of [16]. Introducing the Weissenberg number:

$$\mathrm{Wi} \equiv \sqrt{\sigma_1}\dot{\gamma} \tag{28}$$

into Eq. (24) gives:

$$\frac{\eta}{\eta_0} = \frac{1+\sigma\,\mathrm{Wi}^2}{1+\mathrm{Wi}^2} \tag{29}$$

where:

$$\sigma \equiv \sigma_2/\sigma_1 \tag{30}$$

Taking the limit as strain rate, $\dot{\gamma}$, goes to infinity yields:

$$\eta_\infty/\eta_0 = \sigma \tag{31}$$

From Eq. (29), specifically for a generalized Newtonian fluid where the shear stress is given by:

$$\tau_{yx} = \eta(\dot{\gamma})\dot{\gamma} \tag{32}$$

which can be non-dimensionalzied to:

$$\mathbb{S} = \frac{\eta(\mathrm{Wi})}{\eta_0}\mathrm{Wi} \tag{33}$$

we need:

$$\sigma \geq 1/9 \tag{34}$$

for the shear stress to increase monotonically with shear rate (see Figure 10).

and that η inflects with $\dot{\gamma}$ at:

$$(\mathrm{Wi},\eta) = \left(\frac{1}{\sqrt{3}}, \frac{3+\sigma}{4}\right) \tag{35}$$

where:

$$\mathrm{Wi}_\mathrm{i} \equiv \sqrt{\sigma_1}\dot{\gamma}_\mathrm{i} \tag{36}$$

and thus, more importantly, the *viscosity curves* will inflect at (see Eq. (90) of [42]; Eq. (87) of [43]):

$$\left(\mathrm{Wi}_{\mathrm{i}},\eta_{\mathrm{i}}\right)=\left(1/\sigma^{1/4},\sqrt{\sigma}\right) \tag{37}$$

By viscosity curves we mean curves of $\ln\eta$ *versus* $\ln\mathrm{Wi}$. Further:

$$\left.\frac{d\ln\eta}{d\ln\mathrm{Wi}}\right|_{\mathrm{Wi}_{\mathrm{i}}}\equiv\left(n-1\right)=\frac{1}{\sigma^{1/4}} \tag{38}$$

where n is called the *power-law index*. By power-law index, we mean one plus the slope of the viscosity curve at its inflection point. Using Eq. (29) to plot Figure 11 from which we see that when $\sigma>1$, the fluid is shear thickening, and when $\sigma=1$, Newtonian, and otherwise, shear thinning.

For the normal stress difference coefficients, in steady shear flow, Eqs. (20)–(23) gives (Eqs. (12) of [41]):

$$\Psi_1\left(\dot{\gamma}\right)=2\lambda_1\eta\left(\dot{\gamma}\right)-2\lambda_2\eta_0 \tag{39}$$

and:

$$\Psi_2\left(\dot{\gamma}\right)=-\left(\lambda_1-\mu_1\right)\eta\left(\dot{\gamma}\right)+\left(\lambda_2-\mu_2\right)\eta_0 \tag{40}$$

which match Eqs. (8.1-8) and (8.1-9a) of [31] and where $\eta\left(\dot{\gamma}\right)$ is given by Eq. (24). Hence:

$$\frac{-\Psi_2\left(\dot{\gamma}\right)}{\Psi_1\left(\dot{\gamma}\right)}\equiv\frac{1}{2}\left[\frac{\left(\lambda_1-\mu_1\right)\eta\left(\dot{\gamma}\right)-\left(\lambda_2-\mu_2\right)\eta_0}{\lambda_1\eta\left(\dot{\gamma}\right)-\lambda_2\eta_0}\right] \tag{41}$$

Eqs. (24), (39) and (40) are then simply related by:

$$\frac{\eta\left(\dot{\gamma}\right)}{\eta_0}=-\frac{\Psi_1\left(\dot{\gamma}\right)}{\Psi_{10}}\left(\frac{\lambda_2}{\lambda_1}-1\right)+\frac{\lambda_2}{\lambda_1}=\frac{\Psi_2\left(\dot{\gamma}\right)}{\Psi_{20}}\left(\frac{\lambda_1-\lambda_2-\mu_1+\mu_2}{\lambda_1-\mu_1}\right)+\frac{\lambda_2-\mu_2}{\lambda_1-\mu_1}=\frac{1+\sigma_2\dot{\gamma}^2}{1+\sigma_1\dot{\gamma}^2} \tag{42}$$

or:

$$\frac{\eta}{\eta_0} = -\frac{\Psi_1}{\Psi_{10}}\left(\frac{\lambda_2}{\lambda_1} - 1\right) + \frac{\lambda_2}{\lambda_1} = \frac{\Psi_2}{\Psi_{20}}\left(\frac{\lambda_1 - \lambda_2 - \mu_1 + \mu_2}{\lambda_1 - \mu_1}\right) + \frac{\lambda_2 - \mu_2}{\lambda_1 - \mu_1} = \frac{1 + \sigma\,\mathrm{Wi}^2}{1 + \mathrm{Wi}^2} \tag{43}$$

where:

$$\Psi_{10} \equiv 2\eta_0\left(\lambda_1 - \lambda_2\right) \tag{44}$$

and:

$$\Psi_{20} \equiv -\eta_0\left(\lambda_1 - \lambda_2 - \mu_1 + \mu_2\right) \tag{45}$$

are the zero shear rate first and second normal stress differences.

Here, we demonstrate the versatility of Eq. (15) by identifying the special cases of (a) the Generalized Newtonian fluid:

$$\lambda_1 = \mu_0 = \mu_1 = \nu_1 = \lambda_2 = \mu_2 = \nu_2 = 0 \tag{46}$$

$$\tau_{ik} = 2\eta_0\dot{\gamma}_{ik} \tag{47}$$

(b) the corotational Maxwell fluid (see Section **2.** of [44]; [45,46,47,48]):

$$\lambda_2 = \mu_0 = \mu_1 = \mu_2 = \nu_1 = \nu_2 = 0 \tag{48}$$

$$\tau_{ik} + \lambda_1 \frac{\mathscr{D}\tau_{ik}}{\mathscr{D}t} = 2\eta_0\dot{\gamma}_{ik} \tag{49}$$

and finally, (c) the corotational Jeffreys fluid (see Section **8.** of [44]):

$$\mu_0 = \mu_1 = \mu_2 = \nu_1 = \nu_2 = 0 \tag{50}$$

$$\tau_{ik} + \lambda_1 \frac{\mathscr{D}\tau_{ik}}{\mathscr{D}t} = 2\eta_0\dot{\gamma}_{ik} + 2\eta_0\lambda_2 \frac{\mathscr{D}\dot{\gamma}_{ik}}{\mathscr{D}t} \tag{51}$$

Eq. (15) has been treated in some detail in (see Chapters 2 and 3 in [49], §8.1 of [31], §7.3 in [32], Section 4.2. in [50], Section **6.3-2** in [51], Section **6.1-7** in [52] and

Section **3.4.5** in [53]). Eq. (15) can be written in integral form (see EXAMPLE 8.1-2 of [31]) Tables 8.1-1 in [31] or 7.3-2 in [32] identify thirteen special cases of Eq. (15) (see also Tables 8.1-8.3 in [54]).

Additionally, the Oldroyd 8-constant framework has been closely connected, albeit approximately, with macromolecular theory ([55,56,57]; see Table 1 of [58]; see Eqs. (32) of [59],[60]; see Tables 6.2-1 and 6.2-2 of [32]; Problems 11B.9 and 11B.10 of [61]; §IV and §V. of [62]; §9.5 of [31]). For instance, when:

$$\begin{aligned} &\eta_p = \bar{n}kT\lambda, \quad \lambda_1 = \lambda, \qquad \lambda_2 = 2\lambda/5, \quad \mu_0 = -2\lambda/7, \\ &\mu_1 = -\lambda/7, \quad \mu_2 = -26\lambda/35, \quad \nu_1 = \nu_2 = 0 \end{aligned} \tag{52}$$

the Oldroyd 8-constant model provides a good approximation to the behaviour of a suspension of rigid dumbbells [58]. Also, when:

$$\begin{aligned} &\eta_p = \frac{b\bar{n}kT\lambda_H}{b+5}, \qquad \lambda_1 = \frac{b(2b+11)\lambda_H}{(2b+7)(b+9)}, \quad \lambda_2 = \frac{-14b\lambda_H}{(2b+7)(b+7)(b+9)}, \\ &\mu_0 = \frac{-6b\lambda_H}{(2b+7)(b+5)(b+9)}, \quad \mu_1 = \frac{b(2b+3)\lambda_H}{(2b+7)(b+9)}, \quad \mu_2 = \frac{-2b(4b+21)\lambda_H}{(2b+7)(b+7)(b+9)}, \\ &\nu_1 = \nu_2 = 0 \end{aligned} \tag{53}$$

the Oldroyd 8-constant model model provides a good approximation to the behaviour of a suspension of FENE dumbbells [58].

Table 5: Literature on Analytical Solutions for Flow between Straight Eccentric Cylinders.

Authors (year)	Constitutive Model	Coordinates System	Velocity Profile	Extrudate Shape	Shear Stress	Forces	[Ref.] (Correction to)
Caldwell (1930)	N	bi	$\mathbb{C}$	Σ			[63]
Piercy *et al*. (1933)	N	bi	Σ	Σ			[64]
Oldroyd (1947)	B	ec	Σ				[65]
Heyda (1959)	N	bi	Σ				[66]
Berker (1963)	N	bi					Sect. 23.9 [67]
Jones (1964); Jones and Jones (1966)	O_8	ec	Σ			χ	[16,19]
Snyder *et al*. (1965)	N	bi	Σ		Σ		[68]
Camilleri and Jones (1966)	O_8	ec	Σ				[18]
Guckes (1975)	P	bi		$\aleph$			[69]
Ballal and Rivlin (1975)	RE	bi	Σ				[70]
Zidan and Hassan (1985)	$O^{(2)}$	bi	Σ				[71]
Kolitawong and Giacomin (2001)	P	bi	$\mathbb{C}$	$\mathbb{C}\aleph$	Σ	$\mathbb{F}$	[37]
This thesis	O_8	ec	Σ	$\mathbb{C}\aleph$	$\mathbb{C}\aleph$	$\mathbb{F}, \chi$	[72,73,74](16)

Legend: B ≡ Bingham; O_8 ≡ 8-constant Oldroyd; P ≡ power-law; N ≡ Newtonian; $O^{(2)}$ ≡ Second-order; RE ≡ Rivlin-Ericksen; ec ≡ eccentric cylindrical coordinates; bi ≡ bipolar cylindrical coordinates; $\mathbb{F}$ ≡ axial force; χ ≡ lateral force; Σ ≡ series; $\mathbb{C}$ ≡ closed form; $\aleph$ ≡ numerical; $\mathbb{C}\aleph$ ≡ closed form with integral defined function;

Table 6: Models included in the Oldroyd 8-constant model (see TABLE 8.1-1 of [31] and TABLE 7.3-2 of [32]).

Model [Ref.]	No. of Constant	Reduce from Oldroyd 8-Constant Model [Eq.(15)] by Assigning	Steady State Shear Flow Viscometric Functions
Oldroyd 6-constant [41]	6	$\nu_1 = \nu_2 = 0$	$\eta(\dot\gamma)\,;\Psi_1(\dot\gamma)\,;\Psi_2(\dot\gamma)$
Oldroyd 4-constant [41]	4	$\mu_1 = \lambda_1\,;\ \mu_2 = \lambda_2\,;\ \nu_1 = \nu_2 = 0$	$\eta(\dot\gamma)\,;\Psi_1(\dot\gamma)\,;\Psi_2 = 0$
Gordon-Schowalter*,† [75]	4	$\lambda_2 = (\eta_s/\eta_0)\lambda_1\,;$ $\mu_1 = (1-\xi)\lambda_1\,;$ $\mu_2 = (1-\xi)(\eta_s/\eta_0)\lambda_1\,;$ $\mu_0 = \nu_1 = \nu_2 = 0$	$\eta(\dot\gamma)\,;\Psi_1(\dot\gamma)\,;\Psi_2(\dot\gamma) < 0$
Johnson-Segalman**,‡ [76,77]	4	$\lambda_2 = (\eta_s/\eta_0)\lambda_1\,;$ $\mu_1 = (1-\xi)\lambda_1\,;$ $\mu_2 = (1-\xi)(\eta_s/\eta_0)\lambda_1\,;$ $\mu_0 = \nu_1 = \nu_2 = 0$	$\eta(\dot\gamma)\,;\Psi_1(\dot\gamma)\,;\Psi_2(\dot\gamma) < 0$
Oldroyd Fluid A (Lower Convected Jeffreys) (see Eq. (A) 9.1-9 of [31])	3	$\mu_1 = -\lambda_1\,;\mu_2 = -\lambda_2\,;$ $\mu_0 = \nu_1 = \nu_2 = 0$	$\eta = \eta_0\,;\Psi_1 = 2\eta_0(\lambda_1 - \lambda_2)\,;$ $\Psi_2 = -\Psi_1$
Oldroyd Fluid B (Upper Convected Jeffreys) (see Eq. (B) 9.1-9 of [31])	3	$\mu_1 = \lambda_1\,;\mu_2 = \lambda_2\,;$ $\mu_0 = \nu_1 = \nu_2 = 0$	$\eta = \eta_0\,;\Psi_1 = 2\eta_0(\lambda_1 - \lambda_2)\,;$ $\Psi_2 = 0$
Second-Order Fluid (see Eq. 8.4-3 of [31])	3	$\lambda_1 = \mu_0 = \mu_1 = \nu_1 = \nu_2 = 0$	$\eta = \eta_0\,;\Psi_1 = -2\lambda_2\eta_0\,;$ $\Psi_2 = \eta_0(\lambda_2 - \mu_2)$
Corotational Jeffreys Model [78,79]	3	$\mu_0 = \mu_1 = \mu_2 = \nu_1 = \nu_2 = 0$	$\eta(\dot\gamma)\,;\Psi_1(\dot\gamma)\,;\Psi_2 = -\frac{1}{2}\Psi_1$
Williams 3-constant Oldroyd Model [80,81]	3	$\mu_1 = \lambda_1\,;\mu_2 = \lambda_2\,;\nu_1 = \frac{2}{3}\lambda_1\,;$ $\nu_2 = \frac{2}{3}\lambda_2\,;\mu_0 = 0$	$\eta(\dot\gamma)\,;\Psi_1(\dot\gamma)\,;\Psi_2 = 0$
Denn Modified Convected Maxwell Model [82]	3	$\mu_1 = \lambda_1\,;\lambda_2 = \mu_0 = \nu_1 = \nu_2 = 0$	$\eta = \eta_0(1 - \lambda_1\mu_2\dot\gamma^2)\,;$ $\Psi_1 = 2\lambda_1\eta\,;\Psi_2 = 0$
Lower Convected Maxwell Model (Eq. (3.23) of [83])	2	$\lambda_2 = \mu_0 = \mu_1 = \mu_2 = \nu_1 = \nu_2 = 0$	$\eta = \eta_0\,;\Psi_1 = 2\lambda_1\eta_0\,;$ $\Psi_2 = -\Psi_1$
Upper Convected Maxwell Model [84]	2	$\lambda_2 = \mu_0 = \mu_1 = \mu_2 = \nu_1 = \nu_2 = 0$	$\eta = \eta_0\,;\Psi_1 = 2\lambda_1\eta_0\,;\Psi_2 = 0$
Corotational Maxwell Model [44]	2	$\lambda_2 = \mu_0 = \mu_1 = \mu_2 = \nu_1 = \nu_2 = 0$	$\eta(\dot\gamma)\,;\Psi_1(\dot\gamma)\,;\Psi_2 = -\frac{1}{2}\Psi_1$

Remark: *corrects eighth row in TABLE 7.3-2 of [32]; † $\eta_0 \equiv (1-\xi)\eta_p + \eta_s$

**corrects last row in TABLE 7.3-2 of [32]; ‡ $\eta_0 \equiv \eta_p + \eta_s$

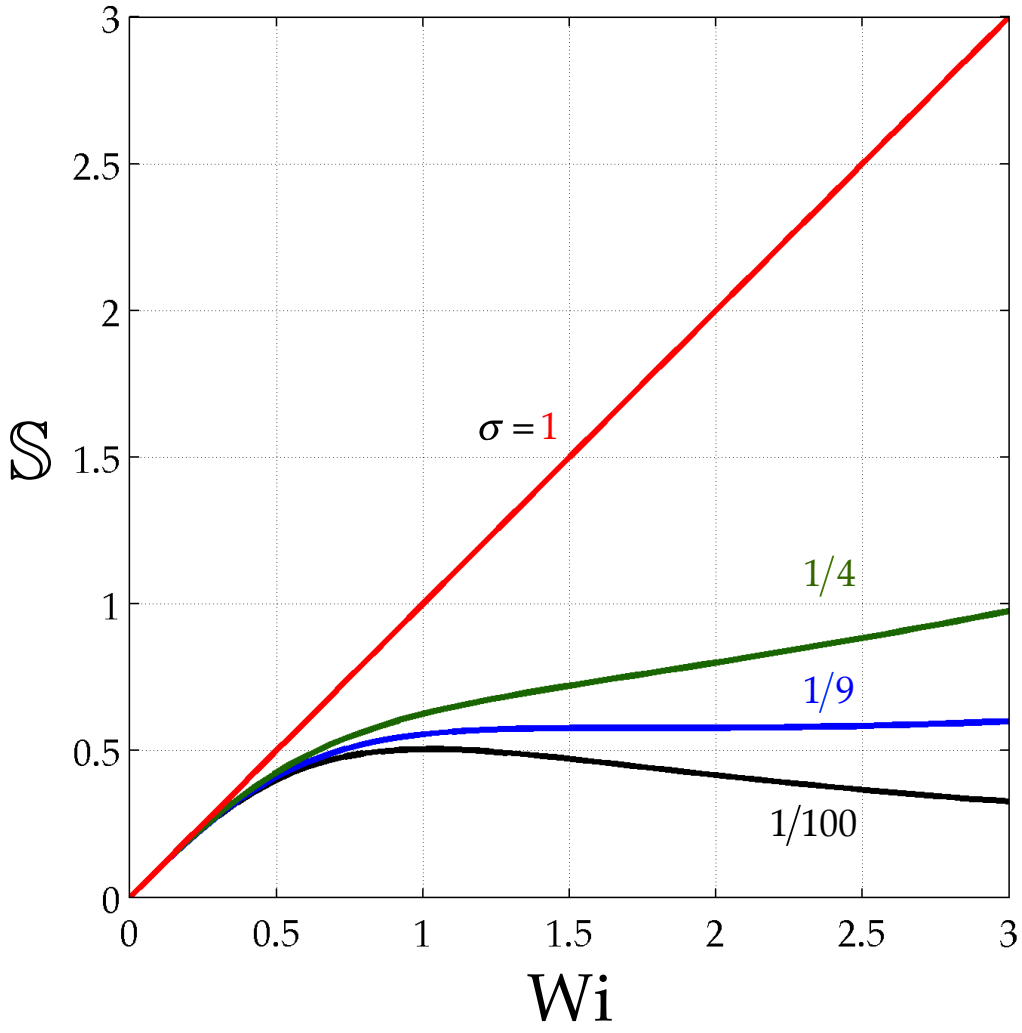

Figure 10: Dimensionless shear stress *versus* Weissenberg number with curves of constant $\sigma = \frac{1}{100}, \frac{1}{9}, \frac{1}{4}, 1$ from bottom to top [Eq. (33)]. **Blue** curve (second from the bottom) shows the critical value of σ for shear-stress monotonicity [Eq. (34)].

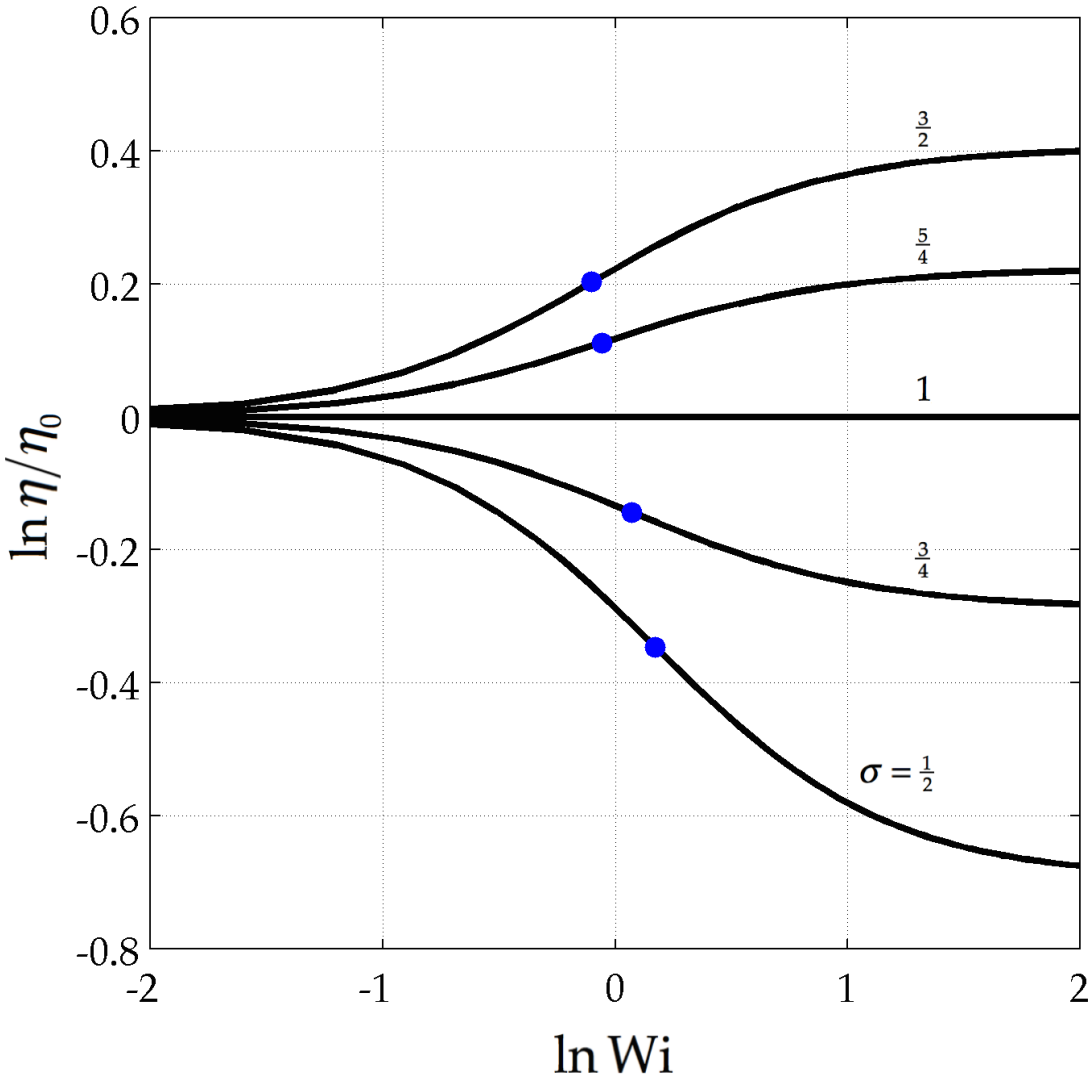

Figure 11: Dimensionless viscosity curves for shear thinning ($\sigma = \frac{1}{2}, \frac{3}{4}$), Newtonian ($\sigma = 1$) and shear thickening ($\sigma = \frac{5}{4}, \frac{3}{2}$) behaviors. **Blue** dots indicate inflections given by Eq. (37).

Chapter 3 Polymer Process Partitioning

Polymer process partitioning yields answers for the relevant polymer process features, including velocity, extrudate shape, stresses and forces. Each of these answers, split naturally into their Newtonian and non-Newtonian parts. For an extrusion from an eccentric annular pipe die, we discovered an important opportunity to improve upon the method of Jones [16], an improvement that we call the rapid convergence approximation [see Eq. (88)].

We use polymer process partitioning to create a graphical procedure to estimate velocity, extrudate shape, stresses and forces in an eccentric pipe die. We accomplish this by adimensionalizing the problem, and then applying the method of Jones [16] which uses eccentric cylindrical coordinates (illustrated and defined in Figure 4) and which first yields an expression for the velocity profile. From this profile, we obtain (i) an expression for the volumetric flow rate (called *throughput*). We then obtain (ii) an expression for the shape of the extruded pipe, which scales with $\langle \breve{v}_z \rangle_\theta$, by integrating the velocity profile, $v_z(\xi,\theta)$, with respect to ξ, through the thickness of the eccentric annulus. Next, we get (iii) expressions for the stresses in the extruded polymer melt. These expressions for the stresses can be used to estimate the upper-bound, for the stress that is frozen into the outermost layer of the plastic pipe (since this layer is quenched first and normally shortly after extrusion). Of course, for semicrystalline polymers, shrinkage will superpose additional stresses upon the frozen pipe

[85,86,87,88,89,90]. We further get (iv) the forces on the mandrel, F_x and F_z. Finally, we use our results to deepen our understanding of (v) knuckling.

As did Jones [16], we choose the 8-constant model due to Oldroyd (see Section 4.9 of [91]) for our analysis because (1) it yields analytical solutions for Items (i) through (v) above, and (2) because of its versatility. By *versatility* we mean that this model contains many simpler models as special cases: (a) generalized Newtonian (including shear-thinning or thickening), (b) corotational Maxwell and (c) corotational Jeffreys. In other words, our analytical solutions for Items (i) through (v) above can be used to explore the role of the Newtonian viscosity for nearly Newtonian material such as commercial grades of condensation polymers. By contrast, our work is equally useful for exploring the roles of shear thinning or shear thickening, with (corotational Maxwell), or without (generalized Newtonian) melt elasticity. We can even compare the roles of retardation without relaxation (second-order fluid), to relaxation without retardation (corotational Maxwell), to relaxation with retardation (corotational Jeffreys). In plastic pipe extrusion, we find example of shear thinning (polyolefins) [92], shear thickening (short glass fiber filled polyolefins) [93], and constant viscosity fluids (tubing from condensation polymers such as nylon). Using this model thus allows us to deepen our understanding of this wide variety of pipe extrusion problems.

3.1 Analytical Solution Method

Here, we begin our analysis of pressure-driven flow through the eccentric annulus illustrated in eccentric cylindrical coordinates in Figure 4 (**Cyan** region). We begin by assuming the flow to be rectilinear:

$$\breve{\mathbf{v}} = \left[0, 0, \breve{v}_z\left(\xi, \theta\right)\right] \tag{54}$$

This approximation neglects a helical secondary flow, where (Eqs. (12a) and (12b) of [19]):

$$\breve{\mathbf{v}} = \left[0, \breve{v}_\theta\left(\xi, \theta\right), \breve{v}_z\left(\xi, \theta\right)\right] \tag{55}$$

For non-Newtonian fluids, this secondary flow has been proven to be small compared to the main flow in axial direction (see Figure 2. of [21] and Figures 4. and 5. of [22])

For a Newtonian fluid:

$$\breve{v}_z \propto 1/\eta_0 \tag{56}$$

For a non-Newtonian fluid, we thus expand the inverse of Eq. (29):

$$\frac{\eta_0}{\eta} = \frac{1+\mathrm{Wi}^2}{1+\sigma\,\mathrm{Wi}^2} = 1+\left(1-\sigma\right)\mathrm{Wi}^2-\left(1-\sigma\right)\sigma\,\mathrm{Wi}^4+\left(1-\sigma\right)\sigma^2\,\mathrm{Wi}^6-\mathrm{O}\left(\mathrm{Wi}^8\right) \tag{57}$$

which suggests our improvement upon Eq. (45) of [16]:

$$\breve{v}_z = v_0+\left(1-\sigma\right)Sv_1-\left(1-\sigma\right)\sigma S^2 v_2+\left(1-\sigma\right)\sigma^2 S^3 v_3-\mathrm{O}\left(S^4\right) \tag{58}$$

where $\mathrm{O}\left(S^4\right)$ represents terms of fourth order and higher, and where:

$$\breve{v}_z \equiv \frac{v_z}{W} \equiv \frac{4\eta_0}{a^2 P} v_z \tag{59}$$

and, the dimensionless pressure gradient squared:

$$S \equiv \frac{\sigma_1 a^2 P^2}{16 \eta_0^{\,2}} \tag{60}$$

and where:

$$P \equiv -dp/dz \tag{61}$$

We truncate Eq. (58) to:

$$\breve{v}_z = v_0 + (1-\sigma) S v_1 \tag{62}$$

Of course, expansions other than Eq. (58), with this same truncation, for $\breve{v}_z$ are possible. One could, for instance, match the *common form* of the results for (i) the volumetric flow rate [Eq. (122)], then (ii) the numerator and the denominator of the shape of the extruded pipe [Eq. (131)], then (iii) the stresses in the melt [Eq. (141)], and finally, (iv) the forces on the mandrel, F_x and F_z [Eqs. (147) and (160)]. We see no more logical equation than Eq. (58), and further, that Eq. (58) is more conservative than the common form when $1/2 < \sigma < 3/2$ (see Eq. (74) below). By *conservative*, we mean closer to the exact expression, Eq. (56).

When treating the helical secondary flow [Eq. (55) above], the Newtonian and non-Newtonian contributions to $\breve{v}_z$ have been partitioned differently (see Eqs. (12a) and (12b) of [19]). For a Newtonian fluid where $\sigma = 1$, Eq. (62) thus reduces to $\breve{v}_z = v_0$.

We begin with the z- component of the equation of motion, in Cartesian coordinates (Eq. (B.5-3) of [40]), evaluated for steady shear flow and in the absence of fluid inertia:

$$\frac{\partial}{\partial x}\left[\eta(\dot{\gamma})\frac{\partial v_z}{\partial x}\right]+\frac{\partial}{\partial y}\left[\eta(\dot{\gamma})\frac{\partial v_z}{\partial y}\right]=-P \tag{63}$$

which, after changing variables (see Eq. (19) of [22] or Eq. (19) of [18]), Jones [16] rewrites, for an Oldroyd 8-constant fluid, as (Eq. (41) of [16]):

$$\left[1+(1+\sigma)S\dot{\gamma}^2\right]\frac{\partial^2 v_z}{\partial\zeta\,\partial\zeta^*}-\frac{(1-\sigma)S}{2}\left[\frac{\partial v_z}{\partial\zeta}\frac{\partial(\dot{\gamma}^2)}{\partial\zeta^*}+\frac{\partial v_z}{\partial\zeta^*}\frac{\partial(\dot{\gamma}^2)}{\partial\zeta}\right]=\frac{-\left(1+S\dot{\gamma}^2\right)^2}{(1-\zeta)^2\left(1-\zeta^*\right)^2} \tag{64}$$

In plastic pipe extrusion, the inertial term in the equation of motion is negligible relative to the viscous term, which therefore dominates. Otherwise put, die flow in plastic pipe extrusion invariably involves Reynolds numbers falling orders of magnitude below unity. To validate any solution to the equation of motion, and thus specifically to validate our solutions for v_z in Eq. (64), it suffices to substitute the solution into Eq. (64).

Substituting Eq. (62) into Eq. (64) and then neglecting the terms of degree of S greater than two, gives:

$$\begin{aligned}&\frac{\partial^2 v_0}{\partial\zeta\,\partial\zeta^*}+(1+\sigma)S\dot{\gamma}^2\frac{\partial^2 v_0}{\partial\zeta\,\partial\zeta^*}+(1-\sigma)S\frac{\partial^2 v_1}{\partial\zeta\,\partial\zeta^*}-\frac{1}{2}(1-\sigma)S\left(\frac{\partial v_0}{\partial\zeta}\right)\frac{\partial\dot{\gamma}^2}{\partial\zeta^*}-\frac{1}{2}(1-\sigma)S\left(\frac{\partial v_0}{\partial\zeta^*}\right)\frac{\partial\dot{\gamma}^2}{\partial\zeta}\\&\quad=-(1-\zeta)^{-2}\left(1-\zeta^*\right)^{-2}-2(1-\zeta)^{-2}\left(1-\zeta^*\right)^{-2}S\dot{\gamma}^2\end{aligned} \tag{65}$$

where for simplicity, we define:

$$\zeta\equiv\xi e^{i\theta} \tag{66}$$

and:

$$\zeta^*\equiv\xi e^{-i\theta} \tag{67}$$

Equating coefficients in Eq. (65) for S^0, and then simplifying gives:

$$\frac{\partial^2 v_0}{\partial\zeta\,\partial\zeta^*} = -\left(1-\zeta\right)^{-2}\left(1-\zeta^*\right)^{-2} \tag{68}$$

the governing partial differential equation for v_0, and then for S^1:

$$\begin{aligned}&\left(1+\sigma\right)\dot{\gamma}^2\frac{\partial^2 v_0}{\partial\zeta\,\partial\zeta^*}+\left(1-\sigma\right)\frac{\partial^2 v_1}{\partial\zeta\,\partial\zeta^*}-\frac{1}{2}\left(1-\sigma\right)\left(\frac{\partial v_0}{\partial\zeta}\right)\frac{\partial\dot{\gamma}^2}{\partial\zeta^*}-\frac{1}{2}\left(1-\sigma\right)\left(\frac{\partial v_0}{\partial\zeta^*}\right)\frac{\partial\dot{\gamma}^2}{\partial\zeta}\\&\quad=-2\left(1-\zeta\right)^{-2}\left(1-\zeta^*\right)^{-2}\dot{\gamma}^2\end{aligned} \tag{69}$$

the governing partial differential equation for v_1. Substituting Eq. (43) of [16] into Eq. (69) gives:

$$\frac{\partial^2 v_1}{\partial\zeta\,\partial\zeta^*} = 2\frac{\partial}{\partial\zeta}\left[\left(1-\zeta\right)^2\left(1-\zeta^*\right)^2\frac{\partial v_0}{\partial\zeta}\left(\frac{\partial v_0}{\partial\zeta^*}\right)^2\right]+2\frac{\partial}{\partial\zeta^*}\left[\left(1-\zeta\right)^2\left(1-\zeta^*\right)^2\left(\frac{\partial v_0}{\partial\zeta}\right)^2\frac{\partial v_0}{\partial\zeta^*}\right] \tag{70}$$

Eqs. (68) and (70) are the Poisson equation in the ζ and ζ^* coordinates. We will employ the method of Poisson (see Section 7.6 in [94]) to solve Eqs. (68) and (70) for the zeroth and first axial velocity coefficients in Subsection 4.1 below.

3.2 Form of the Solutions

In this subsection, we first tackle the velocity profile. From this profile, we then obtain (i) the volumetric flow rate, then (ii) the shape of the extruded pipe, then (iii) the stresses in the melt, and finally, (iv) the forces on the mandrel, F_x and F_z. We cast all of our results in dimensionless terms, and specifically in the form:

$$\mathscr{P} = \mathscr{P}_0+\left(1-\sigma\right)S\mathscr{P}_1 \tag{71}$$

which is a truncation of an expansion in $(1-\sigma)\sigma^{o-1}S^{o}$, where o is the order of the expansion [see Eq.(62)]:

$$\mathscr{P} = \mathscr{P}_0 + (1-\sigma)S\mathscr{P}_1 + \mathrm{O}(S^2) \tag{72}$$

where $\mathrm{O}(S^2)$ is the truncation, and where $\mathscr{P}_0$ and $\mathscr{P}_1$ are function of geometry only, and specifically $\mathscr{P}_0(\xi_i,\xi_o)$ and $\mathscr{P}_1(\xi_i,\xi_o)$. For items (i) through (iv) defined above, $\mathscr{P}$ is the result:

(i) $\breve{Q}$, (ii) $\left(\langle\breve{v}_z\rangle_{\theta=0},\langle\breve{v}_z\rangle_{\theta=\pi}\right)$, (iii) $\mathbb{S}_{\mathrm{m}}$ and (iv) $\mathbb{F},\chi$,

$\mathscr{P}_0$ is the Newtonian contribution:

(i) $\breve{Q}_0$, (ii) $\left(\breve{Q}_{\theta,0}(0),\breve{Q}_{\theta,0}(\pi)\right)$, (iii) $\mathbb{S}_0$ and (iv) $\mathbb{F}_0,\chi_0$

and $\mathscr{P}_1$ is the *non-Newtonian variable*:

(i) $\breve{Q}_1$, (ii) $\left(\breve{Q}_{\theta,1}(0),\breve{Q}_{\theta,1}(\pi)\right)$, (iii) $\mathbb{S}_1$ and (iv) $\mathbb{F}_1,\chi_1$.

By non-Newtonian variable, we mean the non-Newtonian contribution divided by $(1-\sigma)S$. Below, we give dimensionless graphs for the Newtonian contributions $\breve{Q}_0$, $\left(\breve{Q}_{\theta,0}(0),\breve{Q}_{\theta,0}(\pi)\right)$, $\mathbb{S}_0$, $\mathbb{F}_0$ and χ_0, and for the non-Newtonian variables $\breve{Q}_1$, $\left(\breve{Q}_{\theta,1}(0),\breve{Q}_{\theta,1}(\pi)\right)$, $\mathbb{S}_1$, $\mathbb{F}_1$ and χ_1. Practitioners can use these plots to design extrusion dies graphically.

From Eq. (62), we glean that all of our results are subject to the constraint:

$$S^2 < 1 \tag{73}$$

where S is given by Eq. (121) from which we learn that S scales roughly with $1/a^6$, where the confocal length a decreases with eccentricity [see Eq. (7)]. From Eq. (72) we can expect our truncated expansion to be accurate when:

$$\left|\frac{(1-\sigma)\sigma S^2 \mathscr{P}_2}{\mathscr{P}_0}\right| \ll 1 \tag{74}$$

Since obtaining $\mathscr{P}_1$ has been laborious, we would expect that obtaining $\mathscr{P}_2$ would be more so.

Chapter 4 Extrusion Die Analysis

In this Chapter, we focus on the consequences of the mandrel decentering. We employ the polymer process partitioning (see Chapter 3) to arrive at analytical solutions of five physical quantities that allow us to deepen our understanding of the extrusion die.

4.1 Velocity Profile

Solving Eq. (68), see Eq. (4.3.47) of [95] for Euler Formula, for the Newtonian part, we get (See Appendix I):

$$v_0 = \sum_{n=0}^{\infty} \phi_n \cos n\theta + \frac{-1}{1 - 2\xi\cos\theta + \xi^2} \tag{75}$$

since the particular part of Eq. (50) of [16] converges to a closed form. We call Eq. (75) *partly closed*. By partly closed, we mean that the particular part of Eq. (75) is in closed form. In Eq. (75):

$$\phi_n = \begin{cases} \alpha_0 + \beta_0 \ln \xi^2 & ; n = 0 \\ 2\alpha_n \xi^n + 2\beta_n \xi^{-n} & ; n \geq 1 \end{cases} \tag{76}$$

with α_n, β_n, ξ_i and ξ_o given by:

$$\alpha_n = \begin{cases} \dfrac{\xi_i^2 \ln \xi_i^2 + \ln \xi_o^2 - \xi_o^2 \ln \xi_o^2 - \ln \xi_i^2}{\left(-\ln \xi_o^2 + \xi_o^2 \ln \xi_o^2 + \ln \xi_i^2 - \xi_o^2 \ln \xi_i^2\right)\left(-1 + \xi_i^2\right)} & ; n = 0 \\ \dfrac{\xi_i^2 \xi_o^{2n} - \xi_o^{2n} + \xi_i^{2n} - \xi_o^2 \xi_i^{2n}}{\left(\xi_o^{2n} - \xi_o^{2n+2} - \xi_i^{2n} + \xi_o^2 \xi_i^{2n}\right)\left(-1 + \xi_i^2\right)} & ; n \geq 1 \end{cases} \tag{77}$$

$$\beta_n = \begin{cases} \dfrac{\xi_o^2 - \xi_i^2}{\left(-\ln\xi_o^2 + \xi_o^2 \ln\xi_o^2 + \ln\xi_i^2 - \xi_o^2 \ln\xi_i^2\right)\left(-1+\xi_i^2\right)} & ; n = 0 \\ \dfrac{-\xi_i^n \xi_o^n \left(\xi_o^2 - \xi_i^2\right)}{\left(-\xi_o^n \xi_i^{-n} + \xi_o^{n+2}\xi_i^{-n} + \xi_o^{-n}\xi_i^n - \xi_o^{-n+2}\xi_i^n\right)\left(-1+\xi_i^2\right)} & ; n \geq 1 \end{cases} \tag{78}$$

where:

$$\xi_i \equiv \frac{\left(R_o^2 - R_i^2 - \delta^2\right) - \left(R_o^4 + R_i^4 + \delta^4 - 2R_i^2R_o^2 - 2R_i^2\delta^2 - 2R_o^2\delta^2\right)^{1/2}}{2\delta R_i}; \delta < \left(R_o - R_i\right) \tag{79}$$

or in dimensionless terms:

$$\xi_i \equiv \frac{\left(1 - \kappa^2 - \epsilon^2\right) - \left(1 + \kappa^4 + \epsilon^4 - 2\kappa^2 - 2\kappa^2\epsilon^2 - 2\epsilon^2\right)^{1/2}}{2\epsilon\kappa}; \epsilon < \left(1 - \kappa\right) \tag{80}$$

and:

$$\xi_o \equiv \frac{\left(R_o^2 - R_i^2 + \delta^2\right) - \left(R_o^4 + R_i^4 + \delta^4 - 2R_i^2R_o^2 - 2R_i^2\delta^2 - 2R_o^2\delta^2\right)^{1/2}}{2\delta R_o}; \delta < \left(R_o - R_i\right) \tag{81}$$

or in dimensionless terms:

$$\xi_o \equiv \frac{\left(1 - \kappa^2 + \epsilon^2\right) - \left(1 + \kappa^4 + \epsilon^4 - 2\kappa^2 - 2\kappa^2\epsilon^2 - 2\epsilon^2\right)^{1/2}}{2\epsilon}; \epsilon < \left(1 - \kappa\right) \tag{82}$$

where the dimensionless eccentricity, ϵ, and the aspect ratio, κ, are defined in Table 2. We use Eqs. (80) and (82) to plot Figure 12. Our Eqs. (75) and (76) differ from Eqs. (49) and (50) of [16] in that Eq. (75) is partly closed.

To solve for v_1, Jones truncated Eq. (49) of [16] to the second harmonic, $n = 2$:

$$v_0 = \sum_{n=0}^{2} \phi_{\mathrm{J}n} \cos n\theta \tag{83}$$

where the subscript J is for Jones [16], and where:

$$\phi_{Jn} = \begin{cases} \alpha_{J0} + \beta_{J0} \ln \xi^2 - \left(1-\xi^2\right)^{-1} & ;n=0 \\ 2\left[\alpha_{Jn}\xi^n + \beta_{Jn}\xi^{-n} - \xi^n\left(1-\xi^2\right)^{-1}\right] & ;n\geq 1 \end{cases} \tag{84}$$

where:

$$\alpha_{Jn} = \begin{cases} \dfrac{\xi_i^2 \ln \xi_i^2 + \ln \xi_o^2 - \xi_o^2 \ln \xi_o^2 - \ln \xi_i^2}{\left(-\ln \xi_o^2 + \xi_o^2 \ln \xi_o^2 + \ln \xi_i^2 - \xi_o^2 \ln \xi_i^2\right)\left(-1+\xi_i^2\right)} & ;n=0 \\ \dfrac{\xi_o^n \xi_i^{-n+2} + \xi_o^{-n}\xi_i^n - \xi_o^{-n+2}\xi_i^n - \xi_o^n \xi_i^{-n}}{\left(\xi_o^{-n+2}\xi_i^n + \xi_o^n \xi_i^{-n} - \xi_o^{-n}\xi_i^n - \xi_o^{n+2}\xi_i^{-n}\right)\left(-1+\xi_i^2\right)} & ;n\geq 1 \end{cases} \tag{85}$$

$$\beta_{Jn} = \begin{cases} \dfrac{\xi_o^2 - \xi_i^2}{\left(-\ln \xi_o^2 + \xi_o^2 \ln \xi_o^2 + \ln \xi_i^2 - \xi_i^2 \ln \xi_i^2\right)\left(-1+\xi_i^2\right)} & ;n=0 \\ \dfrac{\xi_i^n \xi_o^n \left(\xi_o^2 - \xi_i^2\right)}{\left(-\xi_o^{-n}\xi_i^n + \xi_o^{-n+2}\xi_i^n + \xi_o^n \xi_i^{-n} - \xi_o^{n+2}\xi_i^{-n}\right)\left(-1+\xi_i^2\right)} & ;n\geq 1 \end{cases} \tag{86}$$

but we find that, for large eccentricity, this truncation gives inaccurate velocity (see Figure 19). To correct this, we begin by noting that in Eqs. (77) and (78), α_n and β_n converge rapidly to α_∞ and 0. We now thus depart from Jones [16], with our own approximation to Eq. (75), by assuming that:

$$\alpha_3 = \alpha_4 = \alpha_5 = \ldots = \alpha_\infty \tag{87}$$

then Eq. (75) becomes:

$$v_0 = \sum_{n=0}^{2} \phi_n \cos n\theta + 2\alpha_\infty \frac{4\xi^3 \cos^3\theta - 3\xi^3 \cos\theta + \xi^4 - 2\xi^4 \cos^2\theta}{1 - 2\xi\cos\theta + \xi^2} - \frac{1}{1 - 2\xi\cos\theta + \xi^2} \tag{88}$$

where:

$$\alpha_\infty \equiv \lim_{n\to\infty} \alpha_n = \lim_{n\to\infty} \frac{\xi_i^{\,2}\xi_o^{\,2n} - \xi_o^{\,2n} + \xi_i^{\,2n} - \xi_o^{\,2}\xi_i^{\,2n}}{\left(\xi_o^{\,2n} - \xi_o^{\,2n+2} - \xi_i^{\,2n} + \xi_o^{\,2}\xi_i^{\,2n}\right)\left(-1+\xi_i^{\,2}\right)} = \frac{1}{1-\xi_o^{\,2}} \tag{89}$$

Eq. (88) differs from Eq. (75) by the closed form for the portion of the homogeneous part of ϕ_n where $n \geq 3$. We thus call our Eq. (88) the *rapid convergence approximation*. This approximation is accurate when:

$$\frac{\alpha_3}{\alpha_\infty} - 1 \ll 1 \tag{90}$$

which, for normal sag compensation, is always the case. Evaluating Eq. (77) for $n = 3$ and substituting this with Eq. (89) into Eq. (90) gives:

$$\frac{\xi_i^{\,6}}{\left(1-\xi_i^{\,2}\right)\left(\xi_o^{\,4}+\xi_i^{\,2}\xi_o^{\,2}+\xi_i^{\,4}\right)} \ll 1 \tag{91}$$

Figure 13 compares our rapid convergence approximation for v_0 [Eq. (88)] with the exact expression [Eq. (75)]. We find good agreement. Figure 13 also compares the Jones [16] truncation for v_0 [Eq. (83)] with the exact expression [Eq. (75)]. The Jones [16] truncation is inaccurate, and unphysical as θ approaches π.

Since substituting the exact expression [Eq. (75)] into Eq. (70) gives an intractable partial differential equation for v_1, we instead substitute Eq. (88) into Eq. (70). We then follow Appendix I to solve for the non-Newtonian part:

$$v_1 = \sum_{n=0}^{\infty} \psi_n \cos n\theta \tag{92}$$

where:

$$\psi_n = \beta_0^3 \psi_n^{(1)} + \beta_0^2 \psi_n^{(2)} + \beta_0 \psi_n^{(3)} + \psi_n^{(4)} \tag{93}$$

with:

$$\psi_n^{(m)} = \begin{cases} \mathrm{A}_0^{(m)} + \mathrm{B}_0^{(m)} \ln \xi^2 + v_{1p,0}^{(m)} & ;\, n = 0 \quad ;\, m = 1,2,3,4 \\ \mathrm{A}_n^{(m)} \xi^n + \mathrm{B}_n^{(m)} \xi^{-n} + v_{1p,n}^{(m)} & ;\, n \geq 1 \quad ;\, m = 1,2,3,4 \end{cases} \tag{94}$$

where:

$$A_n^{(m)} = \begin{cases} \dfrac{\ln \xi_o^{\,2} v_{1p,0}^{(m)}(\xi_i) - \ln \xi_i^{\,2} v_{1p,0}^{(m)}(\xi_o)}{\ln \xi_i^{\,2} - \ln \xi_o^{\,2}} & ;\, n = 0 \\ \dfrac{\xi_i^{\,-n} v_{1p,n}^{(m)}(\xi_o) - \xi_o^{\,-n} v_{1p,n}^{(m)}(\xi_i)}{\xi_o^{\,-n} \xi_i^{\,n} - \xi_o^{\,n} \xi_i^{\,-n}} & ;\, n \geq 1 \end{cases} \tag{95}$$

and:

$$B_n^{(m)} = \begin{cases} \dfrac{v_{1p,0}^{(m)}(\xi_i) - v_{1p,0}^{(m)}(\xi_o)}{\ln \xi_o^{\,2} - \ln \xi_i^{\,2}} & ;\, n = 0 \\ \dfrac{\xi_o^{\,n} v_{1p,n}^{(m)}(\xi_i) - \xi_i^{\,n} v_{1p,n}^{(m)}(\xi_o)}{\xi_o^{\,-n} \xi_i^{\,n} - \xi_o^{\,n} \xi_i^{\,-n}} & ;\, n \geq 1 \end{cases} \tag{96}$$

Eq. (93) separates ψ_n into four groups: $\psi_n^{(1)}$, $\psi_n^{(2)}$, $\psi_n^{(3)}$ and $\psi_n^{(4)}$. In Eq. (94), we neglect all non-zero harmonics higher than the fourth ($n > 4$).

The particular parts of the first group $\psi_n^{(1)}$ defined in Eq. (94) are given by:

$$v_{1p,0}^{(1)} = \xi^2 - \xi^{-2} \tag{97}$$

$$v_{1p,1}^{(1)} = 2\xi - 4\xi \ln \xi - 4\xi^{-1} \ln \xi \tag{98}$$

and the particular parts of the second group $\psi_n^{(2)}$ in Eq. (94):

$$v_{1p,0}^{(2)} = \left(6\alpha_2 - 6\alpha_1\right)\xi^2 + \left(6\beta_2 - 6\beta_1\right)\xi^{-2} \tag{99}$$

$$v_{1p,1}^{(2)} = C_{12,1}\xi^3 + C_{12,2}\xi + C_{12,3}\xi \ln \xi + C_{12,4}\xi^{-1} \ln \xi + C_{12,5}\xi^{-3} \tag{100}$$

$$v_{1p,2}^{(2)} = C_{22,1}\xi^4 + C_{22,2}\xi^2 + C_{22,3}\xi^2\ln\xi + C_{22,4} + C_{22,5}\xi^{-2} + C_{22,6}\xi^{-2}\ln\xi + \tfrac{10}{3}\beta_2\xi^{-4} \tag{101}$$

$$v_{1p,3}^{(2)} = C_{32,1}\xi^3 + C_{32,2}\xi^3\ln\xi + 8\beta_2\xi^{-3}\ln\xi + \tfrac{4}{3}\beta_2\xi^{-3} \tag{102}$$

$$v_{1p,4}^{(2)} = \left(-\tfrac{2}{3}\alpha_2 + \tfrac{2}{3}\alpha_\infty\right)\xi^2 - \tfrac{2}{3}\beta_2\xi^{-2} \tag{103}$$

where the coefficients $C_{12,\ell}$, $C_{22,\ell}$ and $C_{32,\ell}$ are defined in Eqs. (259)-(261) in Appendix II, and the particular parts of the third group $\psi_n^{(3)}$ in Eq. (94):

$$v_{1p,0}^{(3)} = C_{03,1}\xi^6 + C_{03,2}\xi^4 + C_{03,3}\xi^2 + 4\ln\xi - \ln\left(\xi^2-1\right)^2 + C_{03,4}\xi^{-2} + C_{03,5}\xi^{-4} - \tfrac{8}{3}\beta_2^2\xi^{-6} \tag{104}$$

$$\begin{aligned} v_{1p,1}^{(3)} = {} & C_{13,1}\xi^5 - \xi^{-1}\ln\left(\xi^2-1\right)^2 - \xi\ln\left(\xi^2-1\right)^2 + C_{13,2}\xi^3 + C_{13,3}\xi \\ & + C_{13,4}\xi\ln\xi - 6\xi^{-1} + C_{13,5}\xi^{-1}\ln\xi + C_{13,6}\xi^{-3} + C_{13,7}\xi^{-5} \end{aligned} \tag{105}$$

$$\begin{aligned} v_{1p,2}^{(3)} = {} & C_{23,1}\xi^4 + C_{23,2}\xi^{-4} + C_{23,3}\xi^2 - \xi^2\ln\left(\xi^2-1\right)^2 + C_{23,4}\xi^2\ln\xi \\ & + C_{23,5} + C_{23,6}\xi^{-2} - \xi^{-2}\ln\left(\xi^2-1\right)^2 + C_{23,7}\xi^{-2}\ln\xi \end{aligned} \tag{106}$$

$$\begin{aligned} v_{1p,3}^{(3)} = {} & C_{33,1}\xi^5 - \xi^3\ln\left(\xi^2-1\right)^2 + C_{33,2}\xi^3 - \xi^{-3}\ln\left(\xi^2-1\right)^2 + C_{33,3}\xi^3\ln\xi \\ & + C_{33,4}\xi + C_{33,5}\xi^{-1} + C_{33,6}\xi^{-5} + C_{33,7}\xi^{-3} + C_{33,8}\xi^{-3}\ln\xi \end{aligned} \tag{107}$$

$$\begin{aligned} v_{1p,4}^{(3)} = {} & -1 + C_{43,1}\xi^6 + \tfrac{1}{2}\alpha_\infty\xi^4 + \left(4-4\alpha_\infty\right)\xi^4\ln\xi - \xi^4\ln\left(\xi^2-1\right)^2 \\ & + C_{43,2}\xi^2 + C_{43,3}\xi^{-2} - \xi^{-4} - \xi^{-4}\ln\left(\xi^2-1\right)^2 - \tfrac{4}{5}\beta_2^2\xi^{-6} \end{aligned} \tag{108}$$

$$\begin{aligned} v_{1p,5}^{(3)} = {} & \alpha_\infty^2\xi^7 + \tfrac{2}{5}\alpha_\infty\xi^5 - \xi^5\ln\left(\xi^2-1\right)^2 + \left(4-4\alpha_\infty\right)\xi^5\ln\xi - \xi^{-5}\ln\left(\xi^2-1\right)^2 - \tfrac{4}{5}\xi^{-5} \\ & + C_{53,1}\xi^3 + C_{53,2}\xi^{-3} + C_{53,3}\xi + C_{53,4}\xi^{-1} \end{aligned} \tag{109}$$

where the coefficients $C_{03,\ell}$, $C_{13,\ell}$, $C_{23,\ell}$, $C_{33,\ell}$, $C_{43,\ell}$ and $C_{53,\ell}$ in Eqs. (262)-(267) in Appendix II, and the particular parts of the fourth group $\psi_n^{(4)}$ in Eq. (94):

$$v_{1p,0}^{(4)} = C_{04,1}\xi^6 + C_{04,2}\xi^4 + C_{04,3}\xi^2 + C_{04,4}\ln\xi + C_{04,5}\ln\left(\xi^2-1\right)^2 + C_{04,6}\xi^{-2} + C_{04,7}\xi^{-4} + C_{04,8}\xi^{-6} + \tfrac{1}{2}\left(1+\xi^2-4\alpha_\infty+4\alpha_\infty\xi^2+4\alpha_\infty^2\xi^4+4\alpha_\infty^2-8\alpha_\infty^2\xi^2\right)\left(\xi^2-1\right)^{-3} \tag{110}$$

$$v_{1p,1}^{(4)} = C_{14,1}\xi^7 + C_{14,2}\xi^5 + C_{14,3}\xi^3 + C_{14,4}\xi + C_{14,5}\xi\ln\xi + C_{14,6}\xi\ln\left(\xi^2-1\right)^2 + C_{14,7}\xi^{-1} + C_{14,8}\xi^{-1}\ln\left(\xi^2-1\right)^2 + C_{14,9}\xi^{-1}\ln\xi + C_{14,10}\xi^{-3} + C_{14,11}\xi^{-5} + C_{14,12}\xi^{-7} + C_{14,13}\xi^{-1}\left(\xi^2-1\right)^{-3} + C_{14,14}\xi\left(\xi^2-1\right)^{-3} + C_{14,15}\xi^3\left(\xi^2-1\right)^{-3} \tag{111}$$

$$v_{1p,2}^{(4)} = C_{24,1}\xi^8 + C_{24,2}\xi^6 + C_{24,3}\xi^4 + C_{24,4}\xi^2 + C_{24,5}\xi^2\ln\xi + C_{24,6}\xi^2\ln\left(\xi^2-1\right)^2 + C_{24,7} + C_{24,8}\xi^{-2} + C_{24,9}\xi^{-2}\ln\xi + C_{24,10}\xi^{-2}\ln\left(\xi^2-1\right)^2 + C_{24,11}\xi^{-4} + C_{24,12}\xi^{-6} + \tfrac{8}{5}\beta_2^3\xi^{-8} + C_{24,13}\xi^6\left(\xi^2-1\right)^{-3} + C_{24,14}\xi^4\left(\xi^2-1\right)^{-3} + C_{24,15}\xi^2\left(\xi^2-1\right)^{-3} + C_{24,16}\left(\xi^2-1\right)^{-3} + C_{24,17}\xi^{-2}\left(\xi^2-1\right)^{-3} \tag{112}$$

$$v_{1p,3}^{(4)} = C_{34,1}\xi^9 + C_{34,2}\xi^7 + C_{34,3}\xi^5 + C_{34,4}\xi^3 + C_{34,5}\xi^3\ln\xi + C_{34,6}\xi^3\ln\left(\xi^2-1\right)^2 + C_{34,7}\xi + C_{34,8}\xi^{-1} + C_{34,9}\xi^{-3} + C_{34,10}\xi^{-3}\ln\xi + C_{34,11}\xi^{-3}\ln\left(\xi^2-1\right)^2 + C_{34,12}\xi^{-5} + C_{34,13}\xi^{-7} + C_{34,14}\xi^7\left(\xi^2-1\right)^{-3} + C_{34,15}\xi^5\left(\xi^2-1\right)^{-3} + C_{34,16}\xi^3\left(\xi^2-1\right)^{-3} + C_{34,17}\xi\left(\xi^2-1\right)^{-3} + C_{34,18}\xi^{-1}\left(\xi^2-1\right)^{-3} + C_{34,19}\xi^{-3}\left(\xi^2-1\right)^{-3} \tag{113}$$

$$v_{1p,4}^{(4)} = C_{44,1}\xi^{10} + C_{44,2}\xi^8 + C_{44,3}\xi^6 + C_{44,4}\xi^4 + C_{44,5}\xi^4\ln\xi + C_{44,6}\xi^4\ln\left(\xi^2-1\right)^2 + C_{44,7}\xi^2 + C_{44,8} + C_{44,9}\xi^{-2} + C_{44,10}\xi^{-4}\ln\left(\xi^2-1\right)^2 + C_{44,11}\xi^{-6} + C_{44,12}\xi^8\left(\xi^2-1\right)^{-3} + C_{44,13}\xi^6\left(\xi^2-1\right)^{-3} + C_{44,14}\xi^4\left(\xi^2-1\right)^{-3} - 3\xi^2\left(\xi^2-1\right)^{-3} + C_{44,15}\left(\xi^2-1\right)^{-3} + C_{44,16}\xi^{-2}\left(\xi^2-1\right)^{-3} + C_{44,17}\xi^{-4}\left(\xi^2-1\right)^{-3} \tag{114}$$

$$v_{1p,5}^{(4)} = C_{54,1}\xi^{11} + C_{54,2}\xi^9 + C_{54,3}\xi^7 + C_{54,4}\xi^5 + C_{54,5}\xi^5\ln\xi + C_{54,6}\xi^5\ln\left(\xi^2-1\right)^2 + C_{54,7}\xi^3 + C_{54,8}\xi + C_{54,9}\xi^{-1} + C_{54,10}\xi^{-3} + C_{54,11}\xi^{-5}\ln\left(\xi^2-1\right)^2 + C_{54,12}\xi^9\left(\xi^2-1\right)^{-3} + C_{54,13}\xi^7\left(\xi^2-1\right)^{-3} + C_{54,14}\xi^5\left(\xi^2-1\right)^{-3} - \tfrac{6}{5}\xi^3\left(\xi^2-1\right)^{-3} - \tfrac{6}{5}\xi\left(\xi^2-1\right)^{-3} + C_{54,15}\xi^{-1}\left(\xi^2-1\right)^{-3} + C_{54,16}\xi^{-3}\left(\xi^2-1\right)^{-3} + C_{54,17}\xi^{-5}\left(\xi^2-1\right)^{-3} \tag{115}$$

where the coefficients $C_{04,\ell}$, $C_{14,\ell}$, $C_{24,\ell}$, $C_{34,\ell}$, $C_{44,\ell}$ and $C_{54,\ell}$, in Eqs. (268)-(273) in Appendix II.

We next use our final expression for the velocity profile, Eq. (62) with Eqs. (75) through (78) and with Eqs. (92) through (273) to draw Figure 14 through Figure 21. Our velocity profile differs only from that of Jones (1964) in its non-Newtonian part, v_1, and specifically we departed from Jones with our rapid convergence approximation in Eq. (88). In Figure 14 through Figure 16, we compare, for small eccentricity, our velocity profiles with the corresponding ones from Jones (Eq. (58) in [16] with Eqs. (49) through (51) and (53) through (57) in [16]). Figure 15 shows close agreement for Newtonian behavior, and by contrast, the discrepancies in Figure 14 and Figure 16 illustrate the improvement from our rapid convergence approximation [Eq. (88)]. Specifically, our introduction of Eq. (88) eliminates the unphysical behaviour as θ approaches π.

However, for large eccentricity, Figure 17 through Figure 19 show that, for non-Newtonian behaviors, this same Eq. (58) in [16] gives a very different results from ours [Eq. (62) with Eqs. (75) through (78) and with Eqs. (92) through (273)]. Figure 17 through Figure 19 also show the improvement affected by our rapid convergence approximation [Eq. (88)]. Figure 20 and Figure 21 (see also Fig. 2 of [16]), show the constant speed contours, from which we learn that the fluid, be it Newtonian or not, flows fastest through the thicker gap. By contrast, whereas both the Newtonian ($\sigma = 1$) and the shear-thickening ($\sigma = \frac{1}{2}$) fluid flow most

slowly through the thinnest gap, the shear-thinning ($\sigma = \frac{3}{2}$) fluid most slowly elsewhere.

As a consistency check, we compare our Newtonian velocity profile, Eq. (75) with Eqs. (76) through (78), with the well-known solution of Kolitawong and Giacomin, Eq. (25) of [37]. Figure 22 shows the close agreement. We attribute the slight discrepancy to the lubrication approximation used in the well-known solution (see APPENDIX B. of [37]).

4.1.1 Validation

To validate any solution to the equation of motion, and thus specifically to validate our solutions for v_z in Eq. (64), it suffices to substitute the solution into Eq. (64). Our solution for v_z is given by Eq. (62) in terms of v_0 and v_1. Since we solve for v_0 exactly, to validate our solutions for v_z in Eq. (64), it suffices to substitute our solution for v_1 into Eq. (70). Substituting Eqs. (75) and (92) into Eq. (70), we find the discrepancies between the left and right sides of Eq. (70):

$$\varepsilon \equiv \frac{\partial^2 v_1}{\partial\zeta\,\partial\zeta^*} - 2\frac{\partial}{\partial\zeta}\left[(1-\zeta)^2\left(1-\zeta^*\right)^2\frac{\partial v_0}{\partial\zeta}\left(\frac{\partial v_0}{\partial\zeta^*}\right)^2\right] + 2\frac{\partial}{\partial\zeta^*}\left[(1-\zeta)^2\left(1-\zeta^*\right)^2\left(\frac{\partial v_0}{\partial\zeta}\right)^2\frac{\partial v_0}{\partial\zeta^*}\right] \quad (116)$$

to be small ($\varepsilon \ll 1$) over the space:

$$\begin{cases} 0 \le \theta \le \pi \\ 0 < \xi < 0.4 \end{cases} \quad (117)$$

By contrast, substituting the solution of Jones [16] [Eqs. (53)–(57)] into Eq. (70) yields discrepancies that are not small at high values of θ or at high values of ξ.

Since S and σ do not appear in Eq. (116), ε depends on neither of these. Thus, validation of our solution for v_z in Eq. (64) also depends on neither of these.

The validation of our solution for v_z in Eq. (64), also validates our truncation of Eq. (58) to Eq. (62) whose coefficient of v_1 is $(1-\sigma)S$. In other words, the physics of pressure driven flow of a non-Newtonian fluid through an eccentric annulus revolves around the product $(1-\sigma)S$.

4.2 Extrudate Shape

The uninitiated may think that the shape of the extrudate that entering cooling chamber will match the shape of the eccentric annulus (see Figure 3). However, the extrudate thickness at any given angular position θ, of course, depends on the integral of the velocity profile at that same position θ. In Subsection 4.1 above, we learnt that the average velocity at that angular position could represent the extruded pipe thickness θ.

The uninitiated may expect die swell to reshape the extrudate between the die and the entrance of the cooling chamber. However, the shape entering the cooling chamber, at any position θ, is propotional to the average velocity in the die at the same position θ. In this work, we neglect any θ or ξ motion that die swell may introduce, and this is not to be confused with neglecting die swell altogether.

To calculate the extruded pipe shape, neglecting any θ or ξ motions that die swell may introduce, we begin with the definition of the volumetric flow rate of the whole cross sectional area of the extrusion die:

$$Q = \int_A v_z(\xi,\theta)\, dA_{\xi\theta} \tag{118}$$

This Eq. (118), and thus the results of this thesis, are generally unaffected by die swell (see [96,97]; Section 7.2.3 of [101]). We are, however, neglecting any θ motion associated with die swell, a quantity that, to our knowledge, has yet to be investigated. Substituting Eq. (13) in Eq. (118), and then adimensionalizing gives:

$$\breve{Q} = \int_0^{2\pi} \int_{\xi_i}^{\xi_o} \frac{\xi \breve{v}_z}{\left(1+\xi^2-2\xi\cos\theta\right)^2}\, d\xi\, d\theta \tag{119}$$

where $\breve{v}_z(\xi,\theta)$ is given by Eq. (62) and:

$$\breve{Q} \equiv \frac{4\eta_0 Q}{a^4 P} \tag{120}$$

which, with Eq. (60), implies that:

$$S \equiv \frac{\sigma_1 a^2 P^2}{16{\eta_0}^2} = \frac{\sigma_1 Q^2}{a^6 \breve{Q}^2} \tag{121}$$

Substituting Eq. (62) into Eq. (119) gives:

$$\breve{Q} = \breve{Q}_0 + (1-\sigma) S \breve{Q}_1 \tag{122}$$

where:

$$\breve{Q}_0 \equiv \int_0^{2\pi} \int_{\xi_i}^{\xi_o} \frac{\xi v_0}{\left(1+\xi^2-2\xi\cos\theta\right)^2}\, d\xi\, d\theta \tag{123}$$

and:

$$\breve{Q}_1 \equiv \int_0^{2\pi} \int_{\xi_i}^{\xi_o} \frac{\xi v_1}{\left(1+\xi^2-2\xi\cos\theta\right)^2} d\xi\, d\theta \tag{124}$$

However, Eqs. (123) and (124) yield no analytical solution, so we integrate numerically, then plot the results in Figure 23. Throughout this thesis, when integrals are evaluated numerically, we use adaptive Simpson quadrature with a tolerance of 10^{-6} (see Section 3 of [98]). We coded Eqs. (123) and (124) into MATLAB (Version R2012b) on a MacBook Air (1.3 GHz Intel Core i5 processor with 4GB 1600 MHz DDR3 memory) employing the OS X (Version 10.10.2) operating system. For each point in Figure 23, we find such an evaluation to consume are 5 and 50 seconds of CPU time for $\breve{Q}_0$ and $\breve{Q}_1$.

For curved hose manufacture, after the hose emerged from the die, the hose is free to bend [99,100]. We thus calculate the radius of curvature of the hose. First, we calculate the average velocity for each wedge $d\theta$:

$$\left\langle \breve{v}_z \right\rangle_\theta = \frac{f^2 \breve{Q}_\theta}{\pi\left(1-\kappa^2\right)} \tag{125}$$

where $f \equiv a/R_o$ is a dimensionless confocal length.

The dimensionless volumetric flow rate at the die exit, for each differential wedge $d\theta$, is defined as:

$$\breve{Q}_\theta \equiv \frac{4\eta_0 Q_\theta}{a^4 P} \tag{126}$$

For angular position θ, Eq. (119) reduces to:

$$\breve{Q}_\theta = \int_{\xi_i}^{\xi_o} \frac{\xi \breve{v}_z}{\left(1+\xi^2-2\xi\cos\theta\right)^2} d\xi \tag{127}$$

Substituting Eq. (62) into Eq. (127) gives:

$$\breve{Q}_\theta = \breve{Q}_{\theta,0} + (1-\sigma) S \breve{Q}_{\theta,1} \tag{128}$$

where:

$$\breve{Q}_{\theta,0} = \int_{\xi_i}^{\xi_o} \frac{\xi}{\left(1+\xi^2-2\xi\cos\theta\right)^2} v_0 \, d\xi \tag{129}$$

$$\breve{Q}_{\theta,1} = \int_{\xi_i}^{\xi_o} \frac{\xi}{\left(1+\xi^2-2\xi\cos\theta\right)^2} v_1 \, d\xi \tag{130}$$

which we will use below.

We can then take the ratio of the average velocity at the top, $\langle \breve{v}_z \rangle_{\theta=0}$, to the bottom, $\langle \breve{v}_z \rangle_{\theta=\pi}$, of the hose, by substituting Eqs. (129) and (130) into Eq. (128), and then this result into Eq. (125):

$$\frac{\langle \breve{v}_z \rangle_{\theta=0}}{\langle \breve{v}_z \rangle_{\theta=\pi}} = \frac{\breve{Q}_{\theta,0}(0) + (1-\sigma) S \breve{Q}_{\theta,1}(0)}{\breve{Q}_{\theta,0}(\pi) + (1-\sigma) S \breve{Q}_{\theta,1}(\pi)} \tag{131}$$

To relate hose curvature to the extrudate shape [given by Eq. (131)], we use Eq. (47) from [37]:

$$\frac{r_0}{(R_i+R_o)/2} = \frac{\langle \breve{v}_z \rangle_{\theta=0} / \langle \breve{v}_z \rangle_{\theta=\pi} + 1}{\langle \breve{v}_z \rangle_{\theta=0} / \langle \breve{v}_z \rangle_{\theta=\pi} - 1} \tag{132}$$

where r_0 is the radius of curvature of the hose (see Figure 2 of [37]), R_i is the radius of the mandrel and R_o is the inner radius of the die.

We next use Eq. (131) with Eqs. (129) and (130) and with Eqs. (75) through (78) , and also with Eqs. (92) through (273) to draw Figure 24 and Figure 25. For each point in Figure 24 and Figure 25, we find such an evaluation to consume are 270, 530, 560 and 200 seconds of CPU time for $\breve{Q}_{\theta,0}(0)$, $\breve{Q}_{\theta,1}(0)$, $\breve{Q}_{\theta,0}(\pi)$ and $\breve{Q}_{\theta,1}(\pi)$.

Together with Eq. (131), Figure 24 and Figure 25 can help plastics engineers predict the shape of the pipe right after emerges from the extrusion die. Together with Eqs. (131) and (132), Figure 24 through Figure 25, can be used by hose engineer to predict extrudate curvature.

4.3 Shear Stress in Die Annulus

When extruded at high throughput, the surface of most polymer extrudates roughen visibly. This wavy skin is called *sharkskin* (see Figure 7.8 in [101]). To prevent sharkskin, some suggest that the highest shear stress cannot exceed roughly 0.1 MPa (see [102]). However, this value depends on the molecular characteristics of the extruded polymer.

The general expression for shear stress in the extrudate is given by:

$$\tau_{\xi z} = \eta(\dot{\gamma})\dot{\gamma} \tag{133}$$

where the viscosity function, $\eta(\dot{\gamma})$ is defined in Eq. (29). Adimensionalizing Eq. (133), and then substituting Eq. (29) into it gives:

$$\mathbb{S} = \frac{1+\sigma\,\mathrm{Wi}^2}{1+\mathrm{Wi}^2}\mathrm{Wi} \tag{134}$$

where:

$$\mathbb{S} \equiv \frac{\sqrt{\sigma_1}\tau_{\xi z}}{\eta_0} \tag{135}$$

or, for a low shear rate, Eq. (134) reduces to:

$$\mathbb{S} = \mathrm{Wi} \tag{136}$$

In pipe extrusion, we freeze the pipe from the outside. We care about the maximum shear stress at the outer surface of the extrudate, which, for a sag compensating die, is at the top [$(\xi,\theta)=(\xi_o,0)$] (see Figure 2) [37].

Adimensionalizing Eq. (27) gives:

$$\mathrm{Wi} = \sqrt{S}\frac{\left(1+\xi^2-2\xi\cos\theta\right)}{\xi}\sqrt{\left(\xi\frac{\partial\breve{v}_z}{\partial\xi}\right)^2+\left(\frac{\partial\breve{v}_z}{\partial\theta}\right)^2} \tag{137}$$

Substituting Eqs. (75) through (78), and (92) through (273) into Eq. (137) then evaluating at $\xi=\xi_i$ and $\theta=0$ gives the maximum Weissenberg number:

$$\mathrm{Wi_m} = \sqrt{S}\left(1+\xi_o{}^2-2\xi_o\right)\left[\mathbb{S}_0+(1-\sigma)S\mathbb{S}_1\right] \tag{138}$$

where:

$$\mathbb{S}_0 \equiv \sum_{n=0}^{\infty}\phi_n'(\xi_o)+\frac{2\xi_o-2}{\left(1-2\xi_o+\xi_o{}^2\right)^2} \tag{139}$$

$$\mathbb{S}_1 \equiv \sum_{n=0}^{\infty}\psi_n'(\xi_o) \tag{140}$$

where ϕ_n' is given by Eq. (274) and ψ_n', by Eq. (275) [with Eqs. (276)-(295)]. Substituting Eq. (138) into Eq. (136) then gives the maximum dimensionless shear stress:

$$\mathbb{S}_{\mathrm{m}} = \sqrt{S}\left(1+\xi_o{}^2-2\xi_o\right)\left[\mathbb{S}_0+\left(1-\sigma\right)S\mathbb{S}_1\right] \tag{141}$$

Our expression for maximum shear stress is also the upper-bound, for the stress that is frozen into the outermost layer of the plastic pipe (since this layer is quenched first and normally shortly after extrusion). Of course, for semicrystalline polymers, shrinkage will superpose additional stresses upon the frozen pipe. Eq. (141) and Figure 26 can thus help plastics engineers estimate the maximum stress that is frozen into the outer surfaces of pipe and hose, and thus, can help them operate without melt fracture.

4.4 Axial Force on Mandrel

The axial force on the mandrel per unit length is given by:

$$F_z \equiv \frac{1}{L}\int_A \tau_{\xi z}\left(\xi_i,\theta\right)dA_{\theta z} \tag{142}$$

where L is the extrusion die length (see Figure 3). Substituting Eq. (14) into Eq. (142), and integrating with respect to z gives:

$$F_z = \int_0^{2\pi} \tau_{\xi z}\left(\xi_i,\theta\right)\frac{a\xi_i}{1+\xi_i{}^2-2\xi_i\cos\theta}d\theta \tag{143}$$

Adimensionalizing Eq. (143) gives:

$$\mathbb{F} = \int_0^{2\pi} \mathbb{S}_i\frac{\xi_i}{1+\xi_i{}^2-2\xi_i\cos\theta}d\theta \tag{144}$$

where:

$$\mathbb{F} \equiv \frac{\sqrt{\sigma_1} F_z}{\eta_0 a} \tag{145}$$

Evaluating Eq. (144) [with Eqs. (134) and (138)] at the inner contour, $\xi = \xi_i$, and then substituting into Eq. (144) gives:

$$\mathbb{F} = \int_0^{2\pi} \xi_i \sqrt{S} \left[\frac{1 + S\left(1 + \xi_i^{\,2} - 2\xi_i \cos\theta\right)^2 \left.\frac{\partial \breve{v}_z}{\partial \xi}\right|_{\xi=\xi_i}^2}{1 + \sigma S\left(1 + \xi_i^{\,2} - 2\xi_i \cos\theta\right)^2 \left.\frac{\partial \breve{v}_z}{\partial \xi}\right|_{\xi=\xi_i}^2} \right] \frac{\left(1 + \xi_i^{\,2} - 2\xi_i \cos\theta\right) \left.\frac{\partial \breve{v}_z}{\partial \xi}\right|_{\xi=\xi_i}}{1 + \xi_i^{\,2} - 2\xi_i \cos\theta} d\theta \tag{146}$$

which yields no analytical solution. However, for small Wi, substituting Eq. (136) [with Eq. (138)] into Eq. (144), and integrating gives:

$$\mathbb{F} = 2\pi \xi_i \sqrt{S} \left[\mathbb{F}_0 + (1 - \sigma) S \mathbb{F}_1 - \frac{2\xi_i}{1 - 2\xi_i^{\,2} + \xi_i^{\,4}} \right] \tag{147}$$

where:

$$\mathbb{F}_0 \equiv K_0 = \phi_0'(\xi_i) \tag{148}$$

and:

$$\mathbb{F}_1 \equiv L_0 = \psi_0'(\xi_i) \tag{149}$$

where ϕ_n' is given by Eq. (274) and ψ_n', by Eq. (275) [with Eqs. (276)-(295)]. We use Eqs. (148) and (149) to plot Figure 27. This figure with Eq. (147) can help plastics engineers design mandrel attachments to withstand the axial force exerted by molten plastic flowing through the die annulus.

4.5 Lateral Force on Mandrel

To calculate the lateral force on the mandrel, we use Eqs. (24) and (59) from [16], subject to our correction to the Jones [16] velocity profile [see Eq. (62) with Eqs. (75) through (78) and with Eqs. (92) through (273) above]:

$$F_x = \Re\left\{ i \oint \tau_{\xi\xi}\left(\dot{\gamma}\right)\Big|_{\xi=\xi_i} dZ \right\} \tag{150}$$

where we quarter the normal component of the extra stress tensor (evaluated on the mandrel) into:

$$\begin{aligned} \tau_{\xi\xi}\left(\dot{\gamma}\right)\Big|_{\xi=\xi_i} \equiv & \left[\frac{\left(\lambda_1 - \mu_1\right)\eta_0\left(1-\sigma\gamma^2\right)}{1-\gamma^2} - \left(\lambda_2 - \mu_2\right)\eta_0 \right]\gamma^2 \\ & -\frac{1}{2}\left(\lambda_1 - \mu_1 - \lambda_2 + \mu_2\right)\left[\sigma\gamma^2 + \ln\left(1+\gamma^2\right) - \sigma\ln\left(1+\gamma^2\right) \right] \end{aligned} \tag{151}$$

and:

$$Z \equiv \frac{a}{1 - \xi_i\cos\theta - i\xi_i\sin\theta} \tag{152}$$

Substituting Eq. (152) into Eq. (150) then gives:

$$F_x = -i\xi_i a \int_{-\pi}^{\pi} \frac{\sin\theta - i\cos\theta}{\left(1 - \xi_i\cos\theta - i\xi_i\sin\theta\right)^2} \tau_{\xi\xi}\left(\dot{\gamma}\right)\Big|_{\xi=\xi_i} d\theta \tag{153}$$

for small Wi, Eq. (151) becomes:

$$\tau_{\xi\xi}\left(\dot{\gamma}\right)\Big|_{\xi=\xi_i} = \left(\lambda_1 - \mu_1 - \lambda_2 + \mu_2\right)\left(1 - \tfrac{1}{2}\sigma\right)\eta_0\dot{\gamma}\left(\xi_i, \theta\right)^2 \tag{154}$$

Evaluating Eq. (27) at $\xi = \xi_i$, then squaring gives:

$$\dot{\gamma}\left(\xi_i,\theta\right)^2=\frac{\left(1-\xi_i\cos\theta-i\xi_i\sin\theta\right)^2\left(1-\xi_i\cos\theta+i\xi_i\sin\theta\right)^2}{a^2}\left(\left.\frac{\partial v_z}{\partial\xi}\right|_{\xi=\xi_i}\right)^2 \tag{155}$$

Substituting Eq. (59) into Eq. (155) gives:

$$\begin{aligned}\dot{\gamma}\left(\xi_i,\theta\right)^2=&\frac{\left(1-\xi_i\cos\theta-i\xi_i\sin\theta\right)^2\left(1-\xi_i\cos\theta+i\xi_i\sin\theta\right)^2W^2}{a^2}\\&\times\left(\sum_{n=0}^{\infty}\left(K_n+\left(1-\sigma\right)SL_n\right)\cos\left(n\theta\right)+\frac{2\xi_i-2\cos\theta}{\left(1-2\xi_i\cos\theta+\xi_i^{\,2}\right)^2}\right)^2\end{aligned} \tag{156}$$

and Eqs. (154) and (156) into Eq. (153) gives:

$$\begin{aligned}F_x=&-i\xi_i\frac{1}{a}\left(\lambda_1-\mu_1-\lambda_2+\mu_2\right)\left(1-\tfrac{1}{2}\sigma\right)\eta_0W^2\\&\times\int_{-\pi}^{\pi}\left\{\begin{array}{l}\left(\sin\theta-i\cos\theta\right)\left(1-\xi_i\cos\theta+i\xi_i\sin\theta\right)^2\\\left(\sum_{n=0}^{\infty}K_n\cos n\theta+\frac{2\xi_i-2\cos\theta}{\left(1-2\xi_i\cos\theta+\xi_i^{\,2}\right)^2}+\sum_{n=0}^{\infty}\left(1-\sigma\right)SL_n\cos n\theta\right)^2\end{array}\right\}d\theta\end{aligned} \tag{157}$$

where $W\equiv a^2P/4\eta_0$ and which expands as:

$$\begin{aligned}F_x=&-i\xi_i\frac{1}{a}\left(\lambda_1-\mu_1-\lambda_2+\mu_2\right)\left(1-\tfrac{1}{2}\sigma\right)\eta_0W^2\\&\times\left[\begin{array}{l}\int_{-\pi}^{\pi}\left(\sin\theta-i\cos\theta\right)\left(1-\xi_i\cos\theta+i\xi_i\sin\theta\right)^2\left(\sum_{n=0}^{\infty}K_n\cos\left(n\theta\right)+\frac{2\xi_i-2\cos\theta}{\left(1-2\xi_i\cos\theta+\xi_i^{\,2}\right)^2}\right)^2d\theta\\+2\int_{-\pi}^{\pi}\left\{\begin{array}{l}\left(\sin\theta-i\cos\theta\right)\left(1-\xi_i\cos\theta+i\xi_i\sin\theta\right)^2\\\times\left(\left[\frac{2\xi_i-2\cos\theta}{\left(1-2\xi_i\cos\theta+\xi_i^{\,2}\right)^2}+\sum_{n=0}^{\infty}K_n\cos\left(n\theta\right)\right]\sum_{n=0}^{\infty}\left(1-\sigma\right)SL_n\cos\left(n\theta\right)\right)\end{array}\right\}d\theta\\+\left(1-\sigma\right)^2S^2\int_{-\pi}^{\pi}\left(\sin\theta-i\cos\theta\right)\left(1-\xi_i\cos\theta+i\xi_i\sin\theta\right)^2\left(\sum_{n=0}^{\infty}L_n\cos\left(n\theta\right)\right)^2d\theta\end{array}\right]\end{aligned} \tag{158}$$

or:

$$\chi=\chi_0+\left(1-\sigma\right)S\chi_1+\left(1-\sigma\right)^2S^2\chi_2 \tag{159}$$

which we truncate to:

$$\chi = \chi_0 + (1-\sigma) S \chi_1 \tag{160}$$

where:

$$\chi \equiv \frac{F_x}{\frac{\xi_i a^3 P^2}{16\eta_0}(\lambda_1 - \mu_1 - \lambda_2 + \mu_2)(1 - \frac{1}{2}\sigma)} \tag{161}$$

$$\chi_0 \equiv \int_{-\pi}^{\pi} \left[\begin{array}{l} -i(\sin\theta - i\cos\theta)(1 - \xi_i \cos\theta + i\xi_i \sin\theta)^2 \\ \times \left[\sum_{n=0}^{\infty} K_n \cos n\theta + \frac{2\xi_i - 2\cos\theta}{(1 - 2\xi_i \cos\theta + \xi_i^{\,2})^2} \right]^2 \end{array} \right] d\theta \tag{162}$$

$$\chi_1 \equiv \int_{-\pi}^{\pi} \left[\begin{array}{l} -2i(\sin\theta - i\cos\theta)(1 - \xi_i \cos\theta + i\xi_i \sin\theta)^2 \\ \times \left\{ \sum_{n=0}^{\infty} K_n \cos n\theta + \frac{2\xi_i - 2\cos\theta}{(1 - 2\xi_i \cos\theta + \xi_i^{\,2})^2} \right\} \sum_{n=0}^{\infty} L_n \cos n\theta \end{array} \right] d\theta \tag{163}$$

$$\chi_2 \equiv \int_{-\pi}^{\pi} (\sin\theta - i\cos\theta)(1 - \xi_i \cos\theta + i\xi_i \sin\theta)^2 \left(\sum_{n=0}^{\infty} L_n \cos(n\theta) \right)^2 d\theta + \ldots \tag{164}$$

and where:

$$K_n \equiv \phi_n'(\xi_i) \tag{165}$$

$$L_n \equiv \psi_n'(\xi_i) \tag{166}$$

where ϕ_n' is given by Eq. (274) and ψ_n', by Eq. (275) in Appendix III [with Eqs. (276)-(295)]. Since Eqs. (162) and (163) do not yield to analytical solution, we evaluate these numerically (see Figure 28). For each point in Figure 28, we find such an evaluation to consume are 10 and 150 seconds of CPU time for χ_0 and χ_1.

From Figure 28, we see that, for Newtonian or shear-thinning fluids ($\sigma \le 1$), χ is always negative. Hence, from Eq. (161), we see that the lateral force, F_x, will be negative when the coefficient $\left(\lambda_1 - \mu_1 - \lambda_2 + \mu_2\right)\left(1 - \frac{1}{2}\sigma\right)$ is positive. Since this coefficient, for Newtonian or shear-thinning fluids, will normally be positive, the lateral force on a sag-compensating die will be downward.

4.6 Worked Example

An engineer gathers the following process details for her high density polyethylene pipe extrusion line, where the pipe dimensions are $R_o = 0.32\,\text{m}$, $R_i = 0.22\,\text{m}$, $\delta = 0.01\,\text{m}$ with the throughput of $\rho Q = 0.01\,\text{kg/s}$, and the material properties at the operating temperature are $\eta_0 = 1.1\times10^7\,\text{Pa·s}$ and $\rho = 900\ \text{kg/m}^3$. From her measured crossover frequency, ω_c, of her $\eta'(\omega)$ and $\eta''(\omega)$ curves at the operating temperature, she estimates a characteristic relaxation time of $\lambda_1 = 1/\omega_c = 1.38\,\text{s}$. She wants to calculate the (i) pressure drop, (ii) extrudate shape, (iii) stresses in the melt, and finally, the (iv) forces on the mandrel, F_x and F_z.

To get the pressure drop per unit length, P, she begins by calculating $\xi_i = 0.0409$, $\xi_o = 0.0594$, $a = 5.3720\ \text{m}$, $\sigma_1 = 1.9\,\text{s}^2$ and $\sigma = 0$ by inserting the given information into, in order, Eqs. (79), (81), (7), (25) and (30). Solving Eq. (120) yields the pressure gradient:

$$P = \frac{4\eta_0 Q}{a^4 \breve{Q}} \tag{167}$$

Substituting Eq. (122) into Eq. (167), and since $\sigma = 0$, gives:

$$P = \frac{4\eta_0 Q}{a^4 \left(\breve{Q}_0 + S \breve{Q}_1 \right)} \tag{168}$$

Substituting Eq. (60) into Eq. (168) then gives:

$$P = \frac{4\eta_0 Q}{a^4 \left(\breve{Q}_0 + \frac{\sigma_1 a^2 P^2}{16 \eta_0^{\,2}} \breve{Q}_1 \right)} \tag{169}$$

Solving the cubic Eq. (169) yields:

$$P = \frac{c}{6} - \frac{2B}{c} \tag{170}$$

where:

$$B \equiv \frac{16 \eta_0^2 \breve{Q}_0}{\sigma_1 a^2 \breve{Q}_1} \tag{171}$$

$$c \equiv \left(108A + 12\sqrt{12B^3 + 81A^2} \right)^{1/3} \tag{172}$$

and:

$$A \equiv \frac{64 \eta_0^3 Q}{\sigma_1 a^6 \breve{Q}_1} \tag{173}$$

To evaluate Eqs. (173), (171) and (172), we need $\breve{Q}_0$ and $\breve{Q}_1$. Interpolating Figure 23 for $\xi_i = 0.0409$ and $\xi_o = 0.0594$ gives $\breve{Q}_0 = 6.94 \times 10^{-7}$ and $\breve{Q}_1 = 2.34 \times 10^{-10}$.

Evaluating Eqs. (173), (171) and (172):

$$A = \frac{64\left(1.1\times10^{7}\,\text{Pa}\cdot\text{s}\right)^{3}\dfrac{0.01\,\text{kg/s}}{900\,\text{kg/m}^{3}}}{1.9\,\text{s}^{2}\left(5.372\,\text{m}\right)^{6}\,2.34\times10^{-10}} = 8.837\times10^{22}\,\frac{\text{Pa}^{3}}{\text{m}^{3}} \tag{174}$$

$$B = \frac{16\left(1.1\times10^{7}\,\text{Pa}\cdot\text{s}\right)^{2}\,6.94\times10^{-7}}{1.9\,\text{s}^{2}\left(5.372\,\text{m}\right)^{2}\,2.34\times10^{-10}} = 1.045\times10^{17}\,\frac{\text{Pa}^{2}}{\text{m}^{2}} \tag{175}$$

$$\begin{aligned} c &= \left(108\left(8.837\times10^{22}\,\frac{\text{Pa}^{3}}{\text{m}^{3}}\right)+12\sqrt{12\left(1.045\times10^{17}\,\frac{\text{Pa}^{2}}{\text{m}^{2}}\right)^{3}+81\left(8.837\times10^{22}\,\frac{\text{Pa}^{3}}{\text{m}^{3}}\right)^{2}}\right)^{1/3} \\ &= 1.122\times10^{9}\,\frac{\text{Pa}}{\text{m}} \end{aligned} \tag{176}$$

and inserting the values in Eqs. (175) and (176) into Eq. (170) yields the required pressure drop per unit die land length:

$$P = \frac{1.122\times10^{9}\,\dfrac{\text{Pa}}{\text{m}}}{6} - \frac{2\left(1.045\times10^{17}\,\dfrac{\text{Pa}^{2}}{\text{m}^{2}}\right)}{1.122\times10^{9}\,\dfrac{\text{Pa}}{\text{m}}} = 8.46\times10^{5}\,\frac{\text{Pa}}{\text{m}} \tag{177}$$

(ii) To get the extrudate shape, $\langle\breve{v}_z\rangle_{\theta=0}/\langle\breve{v}_z\rangle_{\theta=\pi}$, she will need five ingredients, in addition to the given information, for Eq. (131) which, since $\sigma = 0$, simplifies to:

$$\frac{\langle\breve{v}_z\rangle_{\theta=0}}{\langle\breve{v}_z\rangle_{\theta=\pi}} = \frac{\breve{Q}_{\theta,0}(0)+S\breve{Q}_{\theta,1}(0)}{\breve{Q}_{\theta,0}(\pi)+S\breve{Q}_{\theta,1}(\pi)} \tag{178}$$

Using Eq. (60), she first evaluates the dimensionless pressure gradient squared:

$$S \equiv \frac{\sigma_1 a^2 P^2}{16\eta_0{}^2} = \frac{1.9\,\text{s}^{2}\left(5.372\,\text{m}\right)^{2}\left(8.46\times10^{5}\,\dfrac{\text{Pa}}{\text{m}}\right)^{2}}{16\left(1.1\times10^{7}\,\text{Pa}\cdot\text{s}\right)^{2}} = 0.02031 \tag{179}$$

and thus S^2 is well below one, as it should be [see Eq. (73)]. Interpolating Figure 24 and Figure 25 for $\xi_i = 0.0409$ and $\xi_o = 0.0594$ gives $\breve{Q}_{\theta,0}(0) = 1.6\times10^{-7}$, $\breve{Q}_{\theta,0}(\pi) = 7.181\times10^{-8}$, $\breve{Q}_{\theta,1}(0) = 4.8136\times10^{-7}$ and $\breve{Q}_{\theta,1}(\pi) = 3.214\times10^{-7}$.

Evaluating Eq. (178) yields the shape of the extrudate that will enter her cooling chamber:

$$\frac{\langle \breve{v}_z \rangle_{\theta=0}}{\langle \breve{v}_z \rangle_{\theta=\pi}} = \frac{1.6\times10^{-7} + (0.02)4.8136\times10^{-7}}{7.181\times10^{-8} + (0.02)3.214\times10^{-7}} = 2.168 \tag{180}$$

She will use this shape in her simulation of sag.

(iii) To calculate the maximum shear stress in the molten plastic, $\mathbb{S}_{\mathrm{m}}$, she uses Eq. (141) which, since $\sigma = 0$, simplifies to:

$$\mathbb{S}_{\mathrm{m}} = \sqrt{S}\left(1 + \xi_o{}^2 - 2\xi_o\right)\left[\mathbb{S}_0 + S\mathbb{S}_1\right] \tag{181}$$

Interpolating Figure 26 for $\xi_i = 0.0409$ and $\xi_o = 0.0594$ gives $\mathbb{S}_0 = -0.04361$ and $\mathbb{S}_1 = -0.1361$, and substituting these into Eq. (181) gives:

$$\begin{aligned}\mathbb{S}_{\mathrm{m}} &= \sqrt{0.02}\left\{1 + (0.0594)^2 - 2(0.0594)\right\}\left[-0.04361 + 0.02(-0.1361)\right] \\ &= -0.005848\end{aligned} \tag{182}$$

Solving Eq. (135) for the maximum dimensional shear stress gives:

$$\tau_{\xi z} = \frac{\mathbb{S}_{\mathrm{m}}\eta_0}{\sqrt{\sigma_1}} = \frac{-0.005848\left(1.1\times10^7\ \mathrm{Pa\cdot s}\right)}{\sqrt{1.9\,\mathrm{s}^2}} = -46.6\,\mathrm{kPa} \tag{183}$$

which she understands to be the upper-bound for the shear stress that will be frozen in to the outer skin of the pipe product.

(iv) For the axial forces on the mandrel, she uses Eq. (147), which, since $\sigma = 0$, reduces to:

$$\mathbb{F} = 2\pi\xi_i\sqrt{S}\left[K_0 - \frac{2\xi_i}{1-2\xi_i^{\,2}+\xi_i^{\,4}} + SL_0\right] \tag{184}$$

Interpolating Figure 27 for $\xi_i = 0.0409$ and $\xi_o = 0.0594$ gives $K_0 = 0.122$ and $L_0 = 5.71\times10^{-6}$, and substituting these into Eq. (147) gives:

$$\begin{aligned}\mathbb{F} &= 2\pi(0.0409)\sqrt{0.02}\left[0.122 - \frac{2(0.0409)}{1-2(0.0409)^2+(0.0409)^4} + 0.02\left(5.71\times10^{-6}\right)\right] \\ &= 0.001462\end{aligned} \tag{185}$$

Solving Eq. (145) for dimensional axial force gives:

$$F_z = \frac{a\eta_0\mathbb{F}}{\sqrt{\sigma_1}} = \frac{(5.372\,\mathrm{m})\left(1.1\times10^7\,\mathrm{Pa\cdot s}\right)0.001462}{\sqrt{1.9\,\mathrm{s^2}}} = 62.6\,\mathrm{kN} \tag{186}$$

Finally, she evaluates Eq. (160) for the lateral force, which, since $\sigma = 0$, reduces to:

$$\chi = \chi_0 + S\chi_1 \tag{187}$$

Interpolating Figure 28 for $\xi_i = 0.0409$ and $\xi_o = 0.0594$ gives $\chi_0 = -9.934\times10^{-4}$ and $\chi_1 = -1.502\times10^{-5}$, and substituting these into Eq. (187) gives:

$$\chi = -9.934\times10^{-4} + 0.02\left(-1.502\times10^{-5}\right) = -9.934\times10^{-4} \tag{188}$$

Solving Eq. (161), and then, since $\sigma = 0$, this simplifies to:

$$F_x = \frac{\lambda_1 \xi_i a^3 P^2}{16\eta_0}\chi = \frac{-1.38\,\mathrm{s}\left(5.3720\ \mathrm{m}\right)^3 0.0409\left(8.46\times10^5\,\frac{\mathrm{Pa}}{\mathrm{m}}\right)^2}{16\left(1.1\times10^7\ \mathrm{Pa\cdot s}\right)}\left(-9.934\times10^{-4}\right) \tag{189}$$
$$= -35.3\ \mathrm{N/m}$$

If the cooling chamber were now removed, the freely emerging extrudate would now curve with a radius of curvature given by Eq. (132). Substituting the value from Eq. (180) into Eq. (132) gives the dimensionless radius of curvature:

$$\frac{r_0}{\left(R_i + R_o\right)/2} = \frac{2.168+1}{2.168-1} = 2.712 \tag{190}$$

Solving Eq. (190) for the dimensional radius of curvature gives:

$$r_0 = \frac{\left(0.22\,\mathrm{m} + 0.32\,\mathrm{m}\right)}{2}2.712 = 0.732\,\mathrm{m} \tag{191}$$

Of course, curved conduit of other radii of curvature can be produced by adjusting the extrudate shape. For this, we solve Eq. (190):

$$\frac{\left\langle \breve{v}_z \right\rangle_{\theta=0}}{\left\langle \breve{v}_z \right\rangle_{\theta=\pi}} = \frac{\left[\dfrac{r_0}{\left(R_i + R_o\right)/2}\right]+1}{\left[\dfrac{r_0}{\left(R_i + R_o\right)/2}\right]-1} \tag{192}$$

which gives the required shape for a given extrudate curvature. This specific worked example happens to be the one we chose to illustrate in Figure 3.

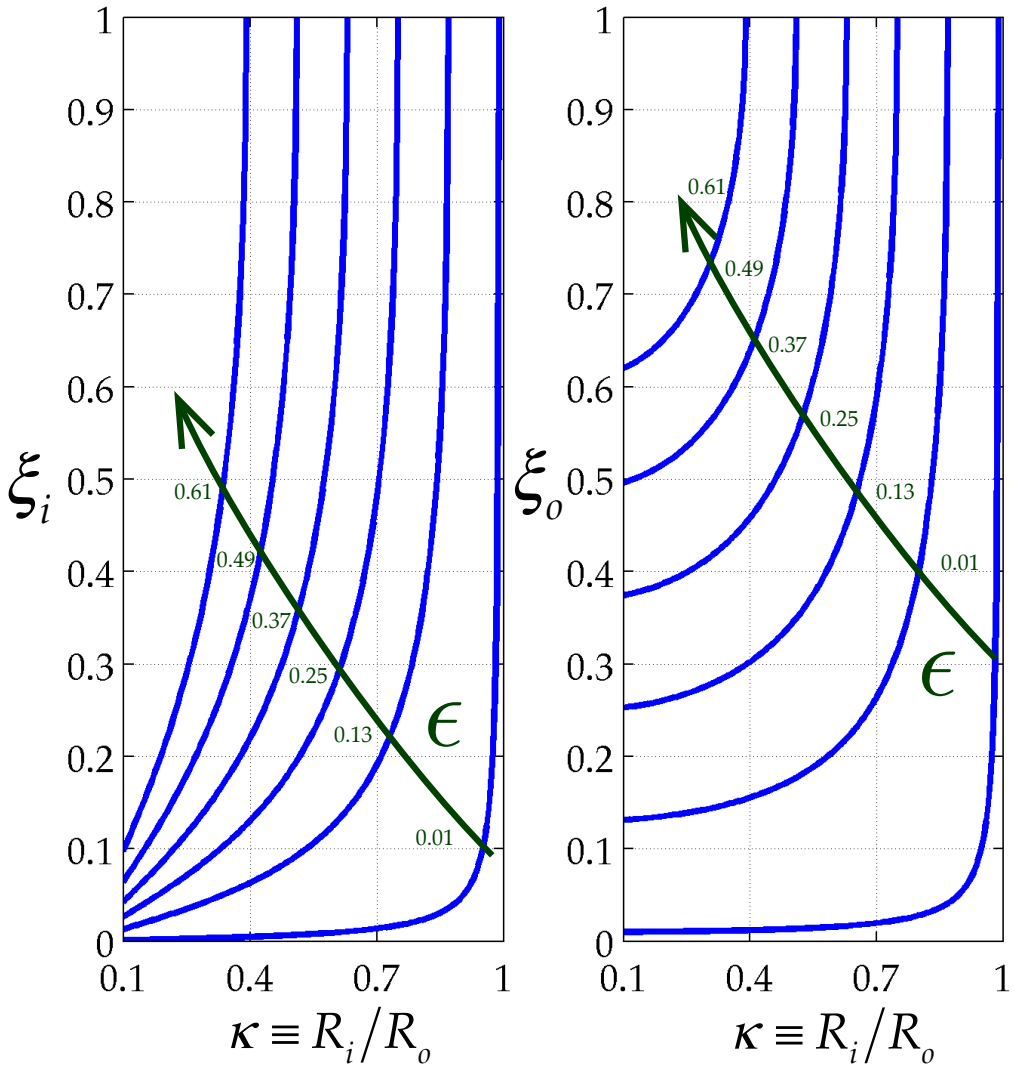

Figure 12: ξ_i and ξ_o *versus* aspect ratio, $\kappa \equiv R_i/R_o$ with curves of constant ϵ.

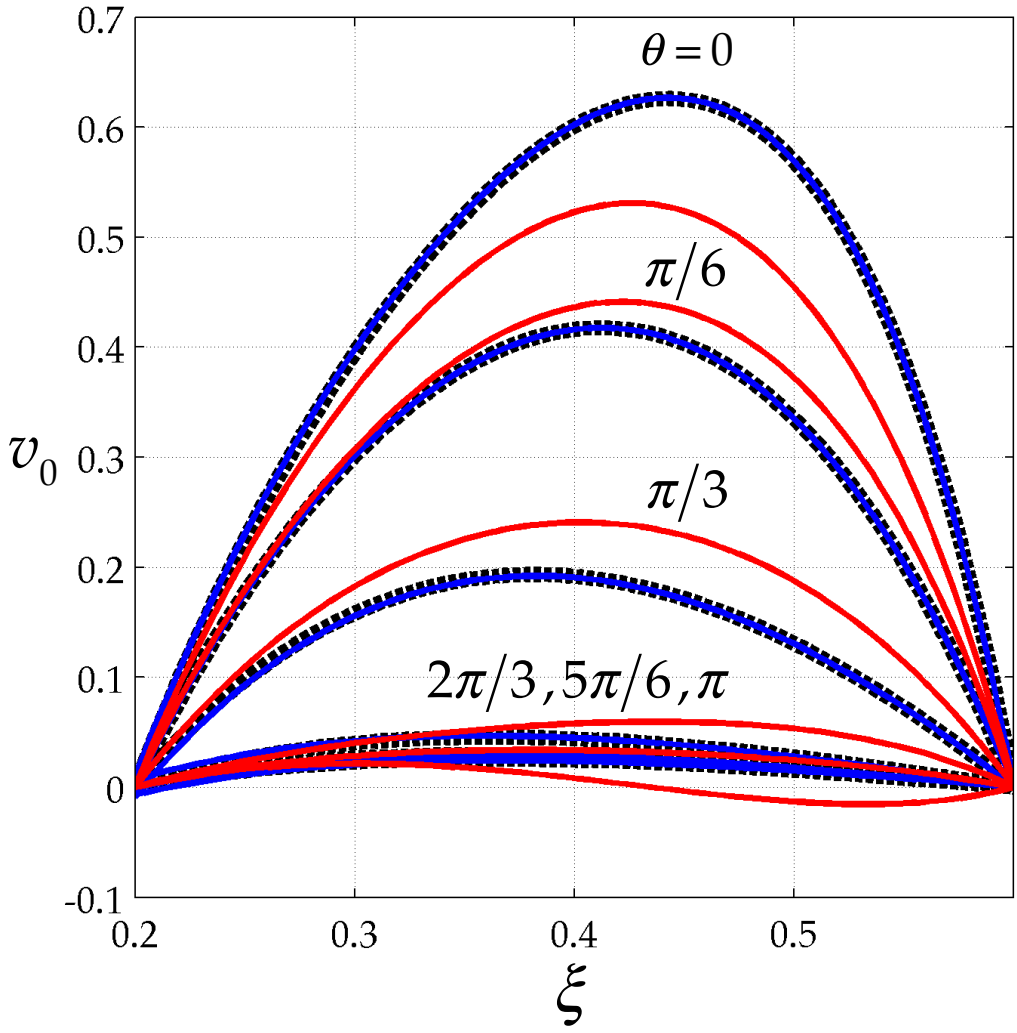

Figure 13: The effectiveness of our rapid convergence approximation [Eq. (88)] (**blue**) that improved upon the Jones [16] truncation [Eq. (83)] (**red**) to the Newtonian contribution to the velocity profile. The dashed **black** curves are the exact expression [Eq. (75)].

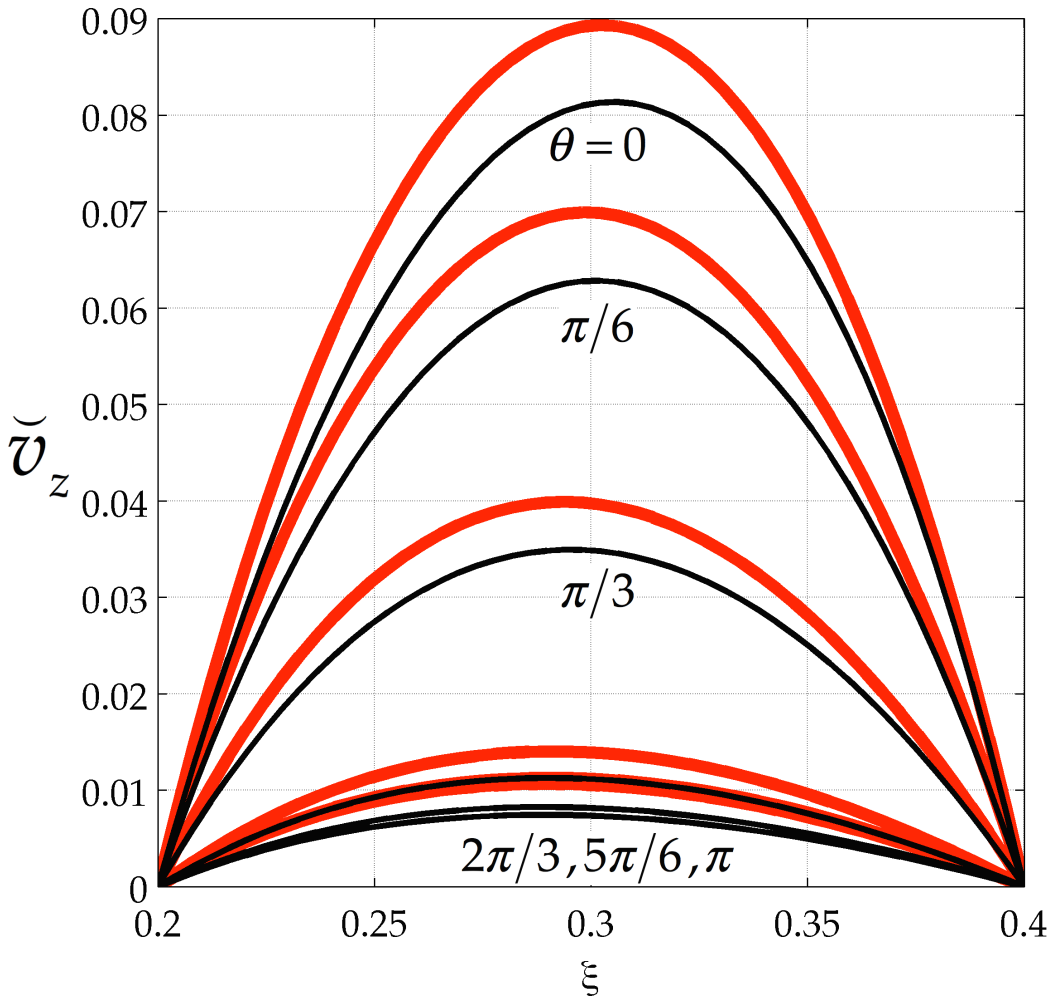

Figure 14: For shear-thinning fluid ($\sigma = \frac{1}{2}$, $S = \frac{1}{5}$), dimensionless axial velocity profiles, $\breve{v}_z$ *versus* ξ, around the eccentric annulus (curves of constant eccentric angular coordinate $\theta = 0, \frac{1}{6}\pi, \frac{1}{3}\pi, \frac{2}{3}\pi, \frac{5}{6}\pi, \pi$ from top to bottom) for the particular die shape $\xi_i = \frac{1}{5}$ and $\xi_o = \frac{2}{5}$. **Black** indicates ours [Eq. (62) with Eqs. (75) and (92)] and **red**, Jones's (Eq. (58) in [16] with Eqs. (49)-(51) and (53)-(57) in [16]). Discrepancies illustrate improvement from rapid convergence approximation [Eq. (88)].

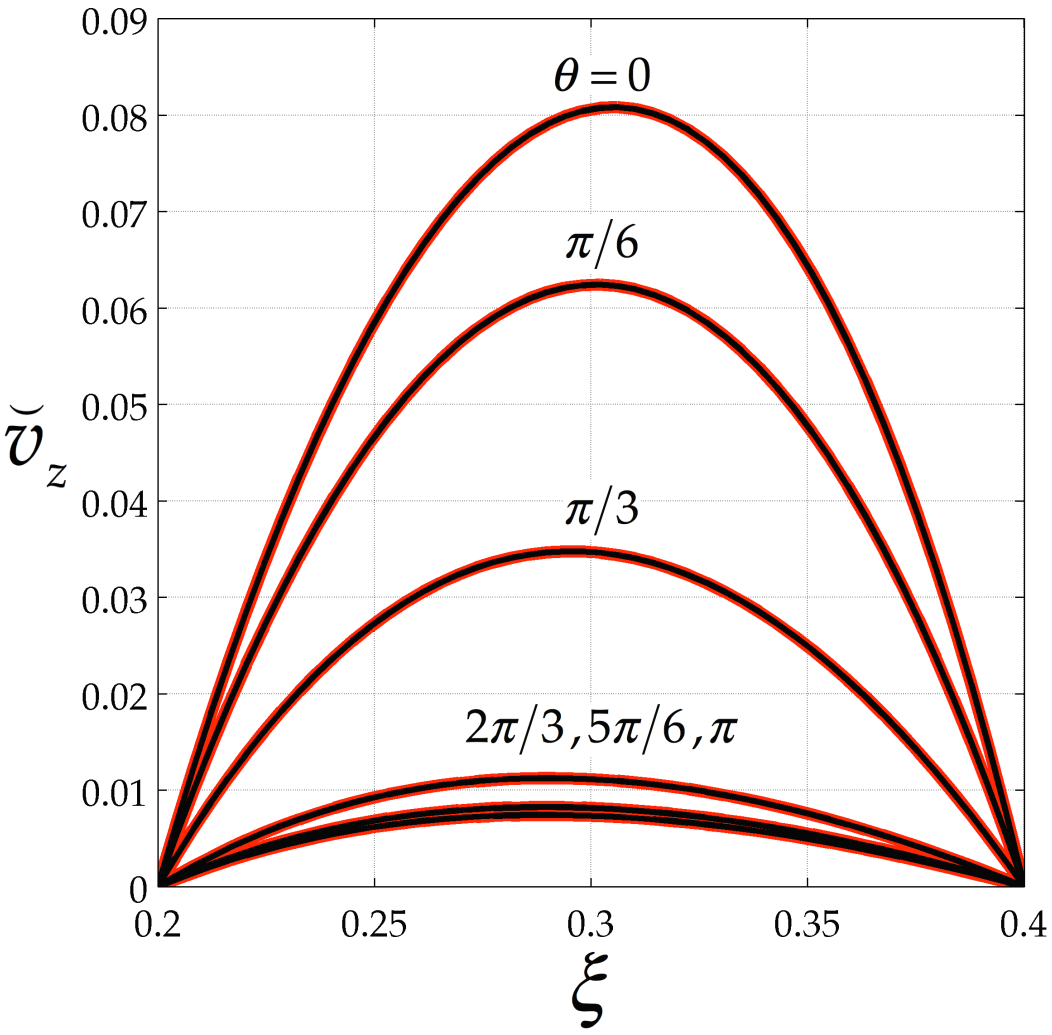

Figure 15: For Newtonian fluid ($\sigma = 1$, $S = \frac{1}{5}$), dimensionless axial velocity profiles, $\breve{v}_z$ *versus* ξ, around the eccentric annulus (curves of constant eccentric angular coordinate $\theta = 0, \frac{1}{6}\pi, \frac{1}{3}\pi, \frac{2}{3}\pi, \frac{5}{6}\pi, \pi$ from top to bottom) for the particular die shape $\xi_i = \frac{1}{5}$ and $\xi_o = \frac{2}{5}$. **Black**, ours [Eq. (62) with Eqs. (75) and (92)] closely matched **red**, Jones's (Eq. (58) in [16] with Eqs. (49)-(51) and (53)-(57) in [16]).

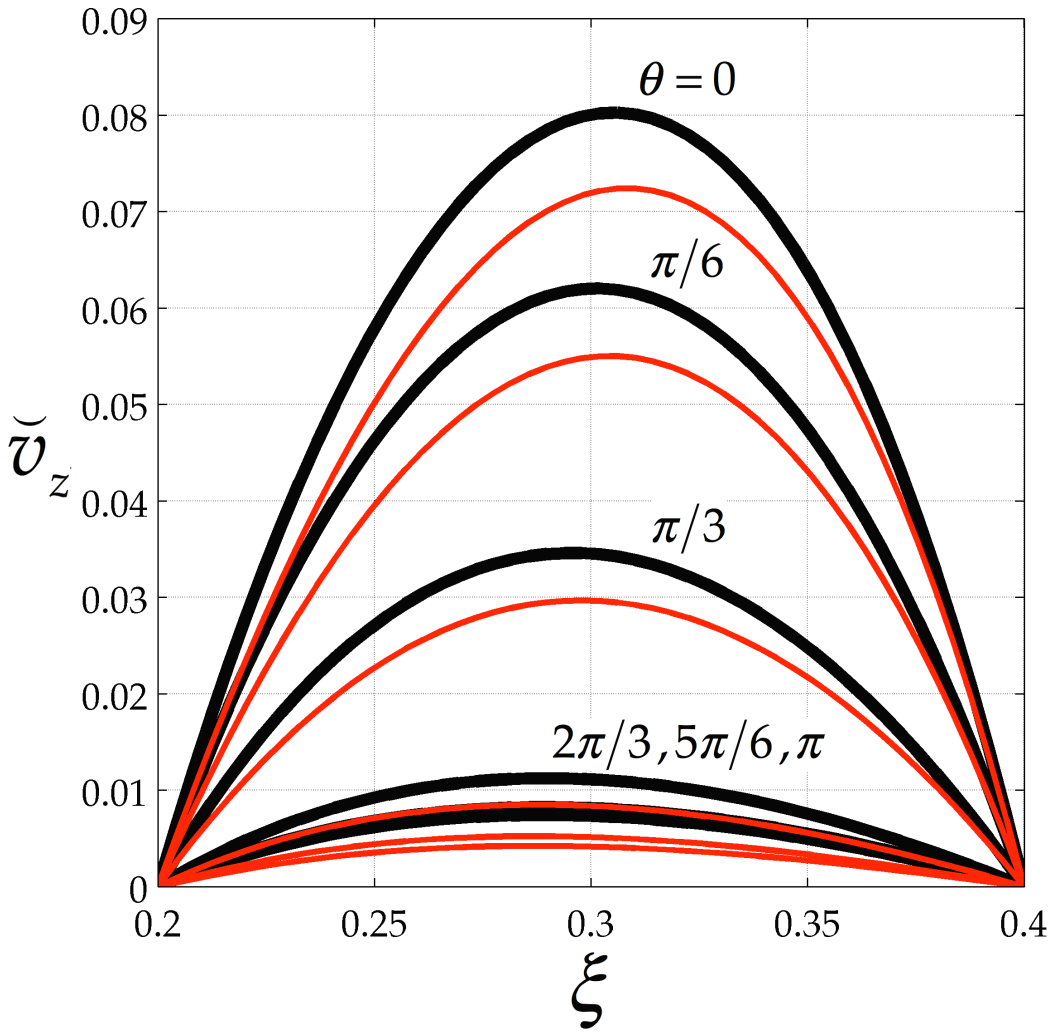

Figure 16: For shear-thickening fluid ($\sigma = \frac{3}{2}$, $S = \frac{1}{5}$), dimensionless axial velocity profiles, $\breve{v}_z$ *versus* ξ, around the eccentric annulus (curves of constant eccentric angular coordinate $\theta = 0, \frac{1}{6}\pi, \frac{1}{3}\pi, \frac{2}{3}\pi, \frac{5}{6}\pi, \pi$ from top to bottom) for the particular die shape $\xi_i = \frac{1}{5}$ and $\xi_o = \frac{2}{5}$. **Black** indicates ours [Eq. (62) with Eqs. (75) and (92)] and **red**, Jones's (Eq. (58) in [16] with Eqs. (49)-(51) and (53)-(57) in [16]). Discrepancies illustrate improvement from rapid convergence approximation [Eq. (88)].

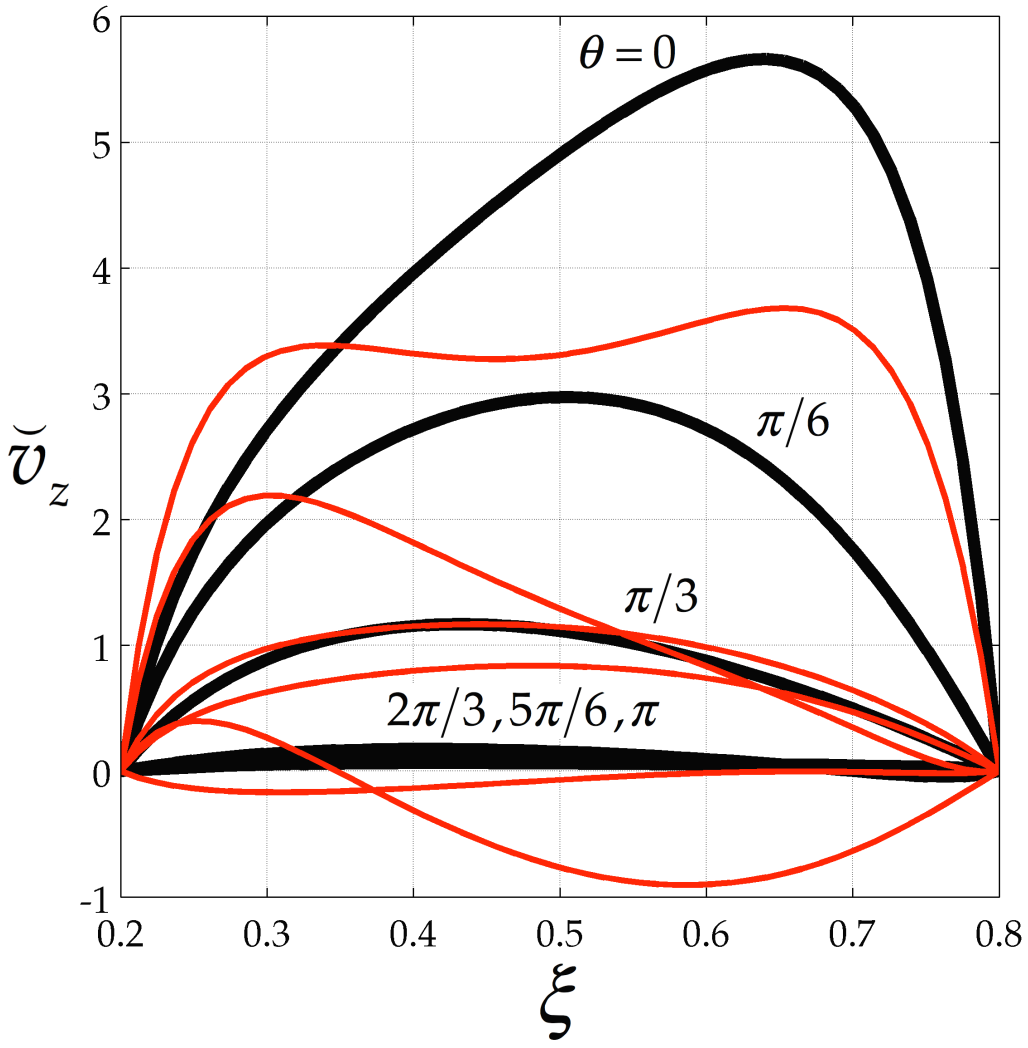

Figure 17: For shear-thinning fluid ($\sigma = \frac{1}{2}$, $S = \frac{1}{5}$), dimensionless axial velocity profiles, $\breve{v}_z$ *versus* ξ, around the eccentric annulus (curves of constant eccentric angular coordinate $\theta = 0, \frac{1}{6}\pi, \frac{1}{3}\pi, \frac{2}{3}\pi, \frac{5}{6}\pi, \pi$, top to bottom) for the particular die shape $\xi_i = \frac{1}{5}$ and $\xi_o = \frac{3}{5}$. **Black** indicates ours [Eq. (62) with Eqs. (75) and (92)] and **red**, Jones's (Eq. (58) in [16] with Eqs. (49) through (51) and (53)-(57) in [16]). Discrepancies illustrate improvement from rapid convergence approximation [Eq. (88)].

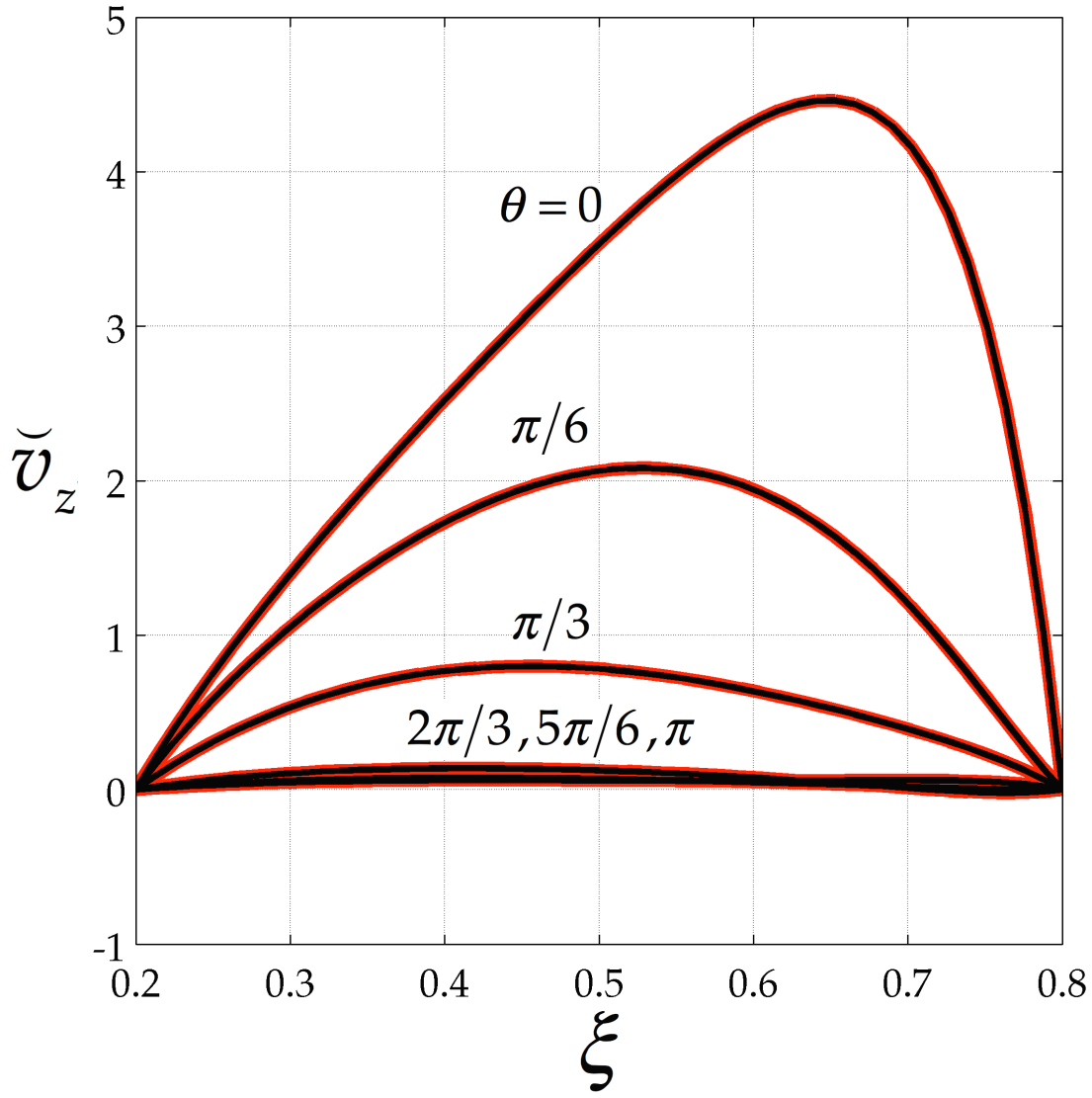

Figure 18: For Newtonian fluid ($\sigma = 1$, $S = \frac{1}{5}$), dimensionless axial velocity profiles, $\breve{v}_z$ *versus* ξ, around the eccentric annulus (curves of constant eccentric angular coordinate $\theta = 0, \frac{1}{6}\pi, \frac{1}{3}\pi, \frac{2}{3}\pi, \frac{5}{6}\pi, \pi$ from top to bottom) for the particular die shape $\xi_i = \frac{1}{5}$ and $\xi_o = \frac{3}{5}$. **Black**, ours [Eq. (62) with Eqs. (75) and (92)] closely matched **red**, Jones's (Eq. (58) in [16] with Eqs. (49) through (51) and (53) through (57) in [16]).

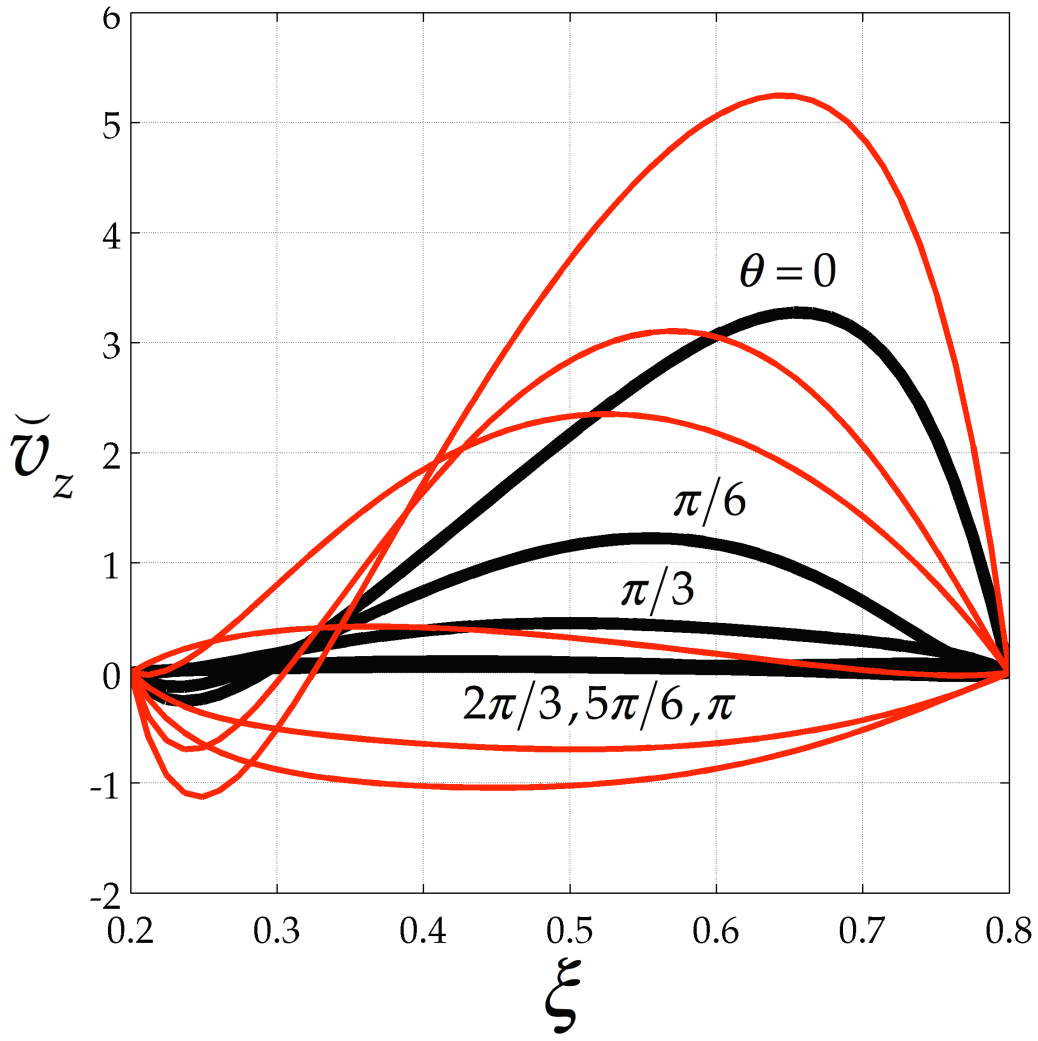

Figure 19: For shear-thickening fluid ($\sigma = \frac{3}{2}$, $S = \frac{1}{5}$), dimensionless axial velocity profiles, $\breve{v}_z$ *versus* ξ, around the eccentric annulus (curves of constant eccentric angular coordinate $\theta = 0, \frac{1}{6}\pi, \frac{1}{3}\pi, \frac{2}{3}\pi, \frac{5}{6}\pi, \pi$ from top to bottom) for the particular die shape $\xi_i = \frac{1}{5}$ and $\xi_o = \frac{3}{5}$. **Black** indicates ours [Eq. (62) with Eqs. (75) and (92)] and **red**, Jones's [Eq. (58) in [16] with Eqs. (49) through (51) and (53) through (57) in [16]]. Discrepancies illustrate improvement from rapid convergence approximation [Eq. (88)].

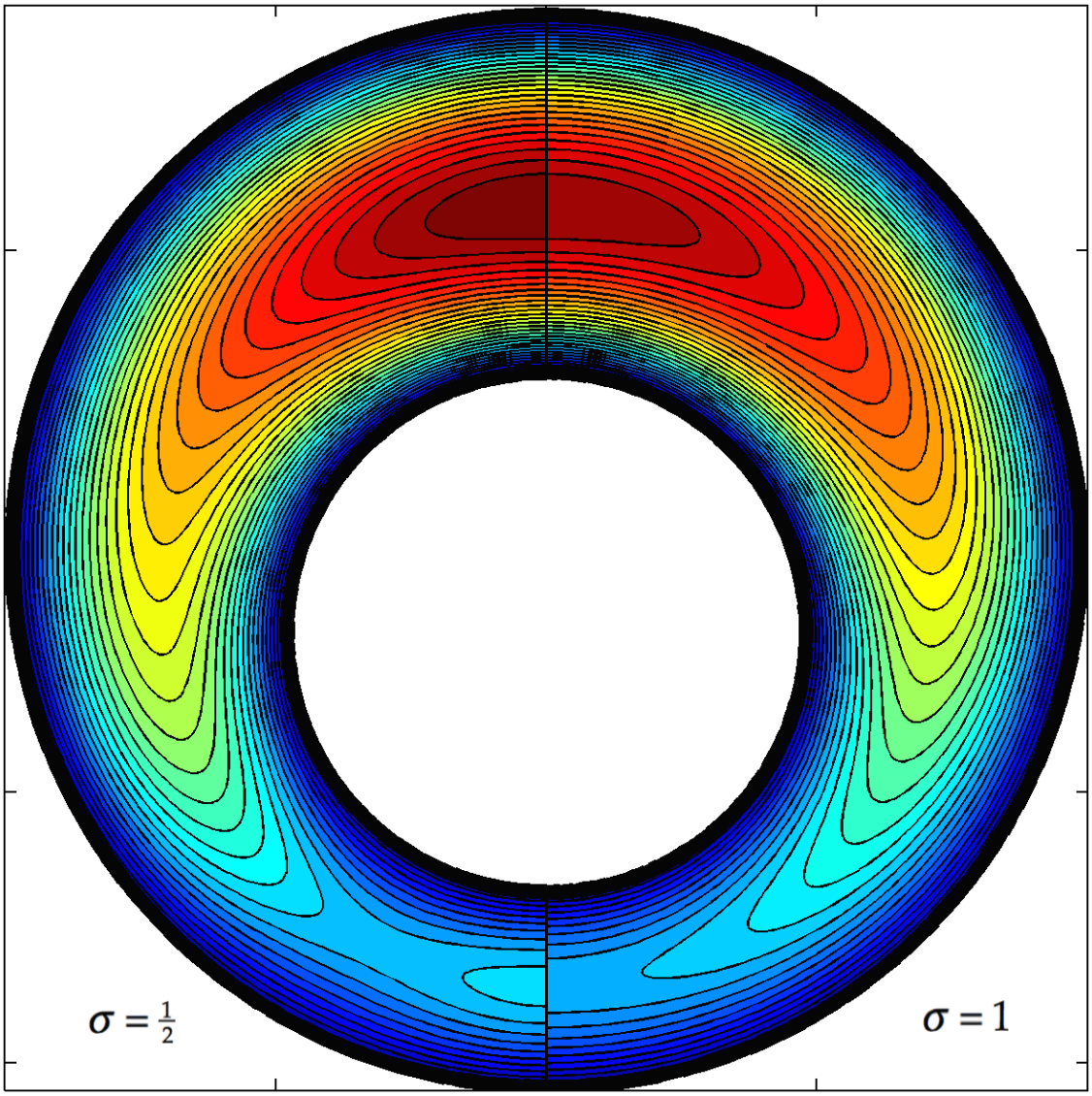

Figure 20: Dimensionless speed, $\breve{v}_z$, over the pipe cross section (30 contours of constant $\breve{v}_z$). Oldroyd 8-constant fluids: shear-thinning, $\sigma = \frac{1}{2}$ (left) *versus* Newtonian, $\sigma = 1$ (right). $S = \frac{1}{20}$, $\xi_i = \frac{1}{10}$ and $\xi_o = \frac{1}{5}$. The **black** near-wall regions are nearly motionless, and the **red**, highest speed ($\breve{v}_{z,\max} = 9.77 \times 10^{-3}$ for $\sigma = \frac{1}{2}$, $\breve{v}_{z,\max} = 9.45 \times 10^{-3}$ for $\sigma = 1$).

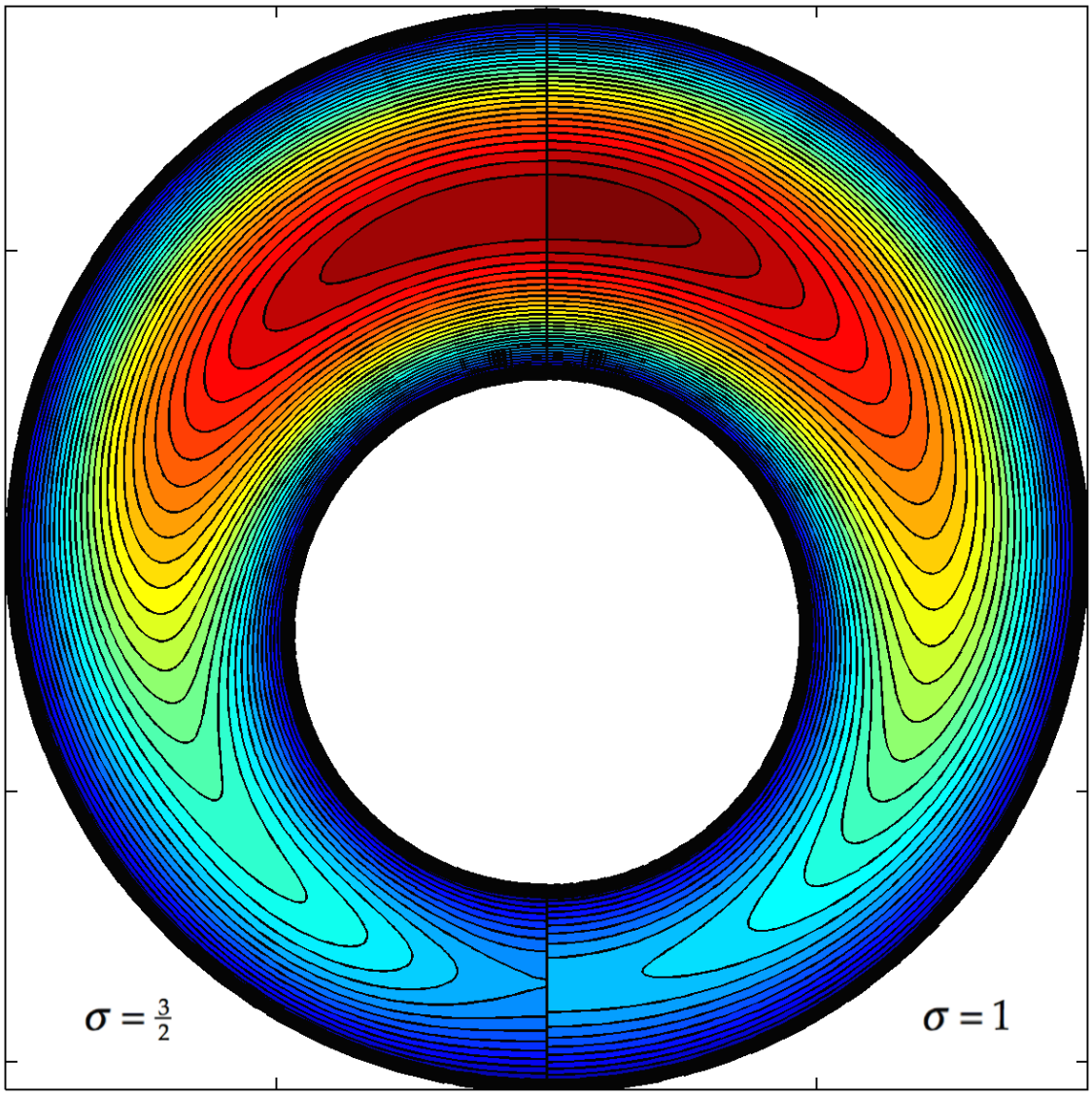

Figure 21: Dimensionless speed, $\breve{v}_z$, over the pipe cross section (30 contours of constant $\breve{v}_z$). Oldroyd 8-constant fluids: shear thickening, $\sigma = \frac{3}{2}$ (left) *versus* Newtonian, $\sigma = 1$ (right). $S = \frac{1}{20}$, $\xi_i = \frac{1}{10}$ and $\xi_o = \frac{1}{5}$. The **black** near-wall regions are nearly motionless, and the **red**, highest speed ($\breve{v}_z = 9.14 \times 10^{-3}$ for $\sigma = \frac{3}{2}$, $\breve{v}_z = 9.45 \times 10^{-3}$ for $\sigma = 1$).

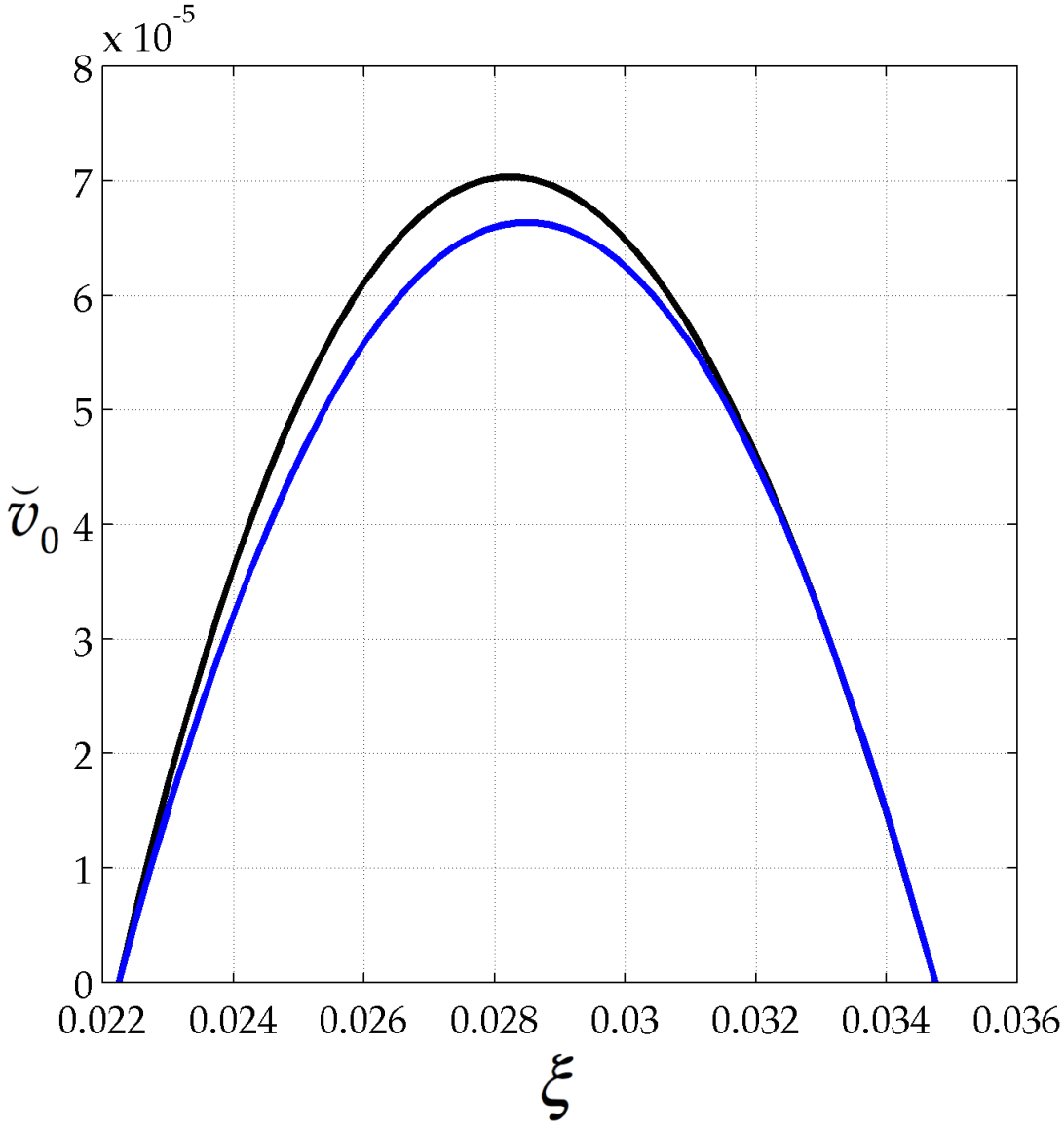

Figure 22: Comparison between our dimensionless axial velocity profiles and well-known solution at evaluates at $\theta = 0$ (corresponding to $\beta = \pi$ in Eq. (25) of [37]) for die shape $R_i = 80\,\text{cm}$, $R_o = 100\,\text{cm}$ and $\delta = 3.5\,\text{cm}$ for Newtonian fluid $\sigma = 1$. **Black**, ours and **Blue**, well-known solution. Slight discrepancy due to our improvement upon the lubrication approximation.

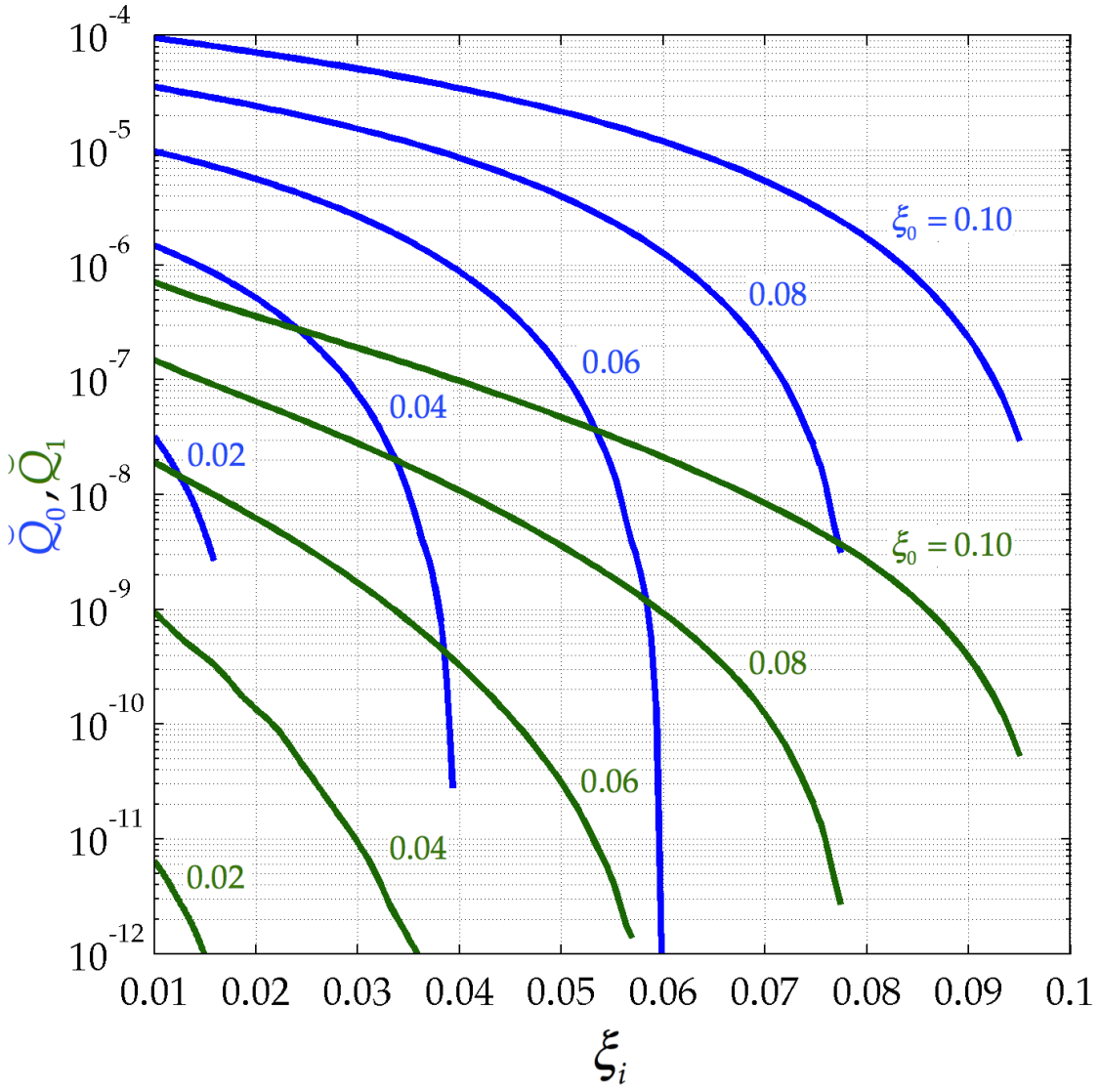

Figure 23: Newtonian, $\breve{Q}_0$ (**blue**), and non-Newtonian variable, $\breve{Q}_1$ (**green**), contributions to volumetric flow rate *versus* ξ_i with $\xi_o = 0.02, 0.04, 0.06, 0.08, 0.10$ isopleths [Eqs. (123) and (124)].

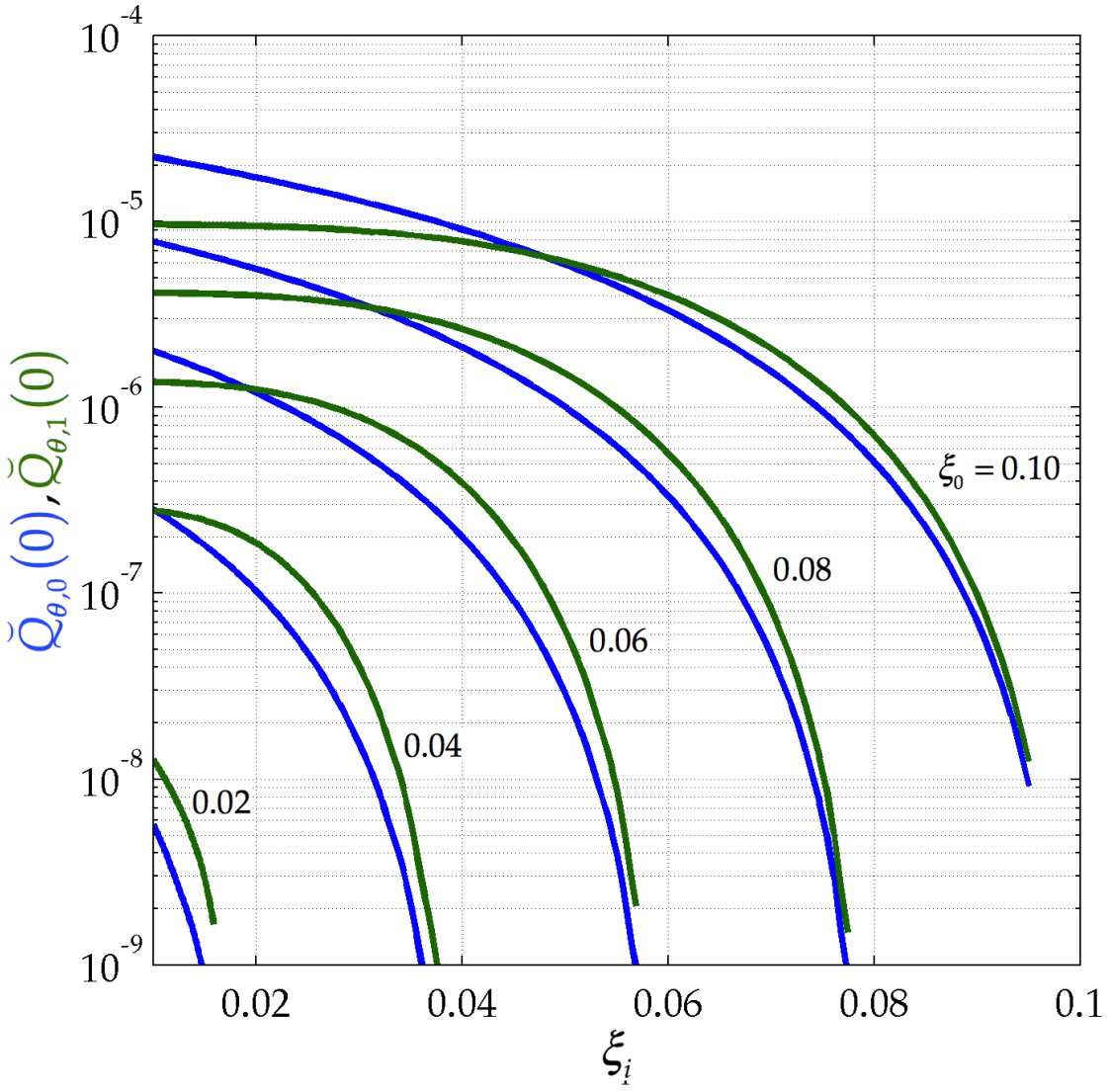

Figure 24: Newtonian, $\breve{Q}_{\theta,0}(0)$ (**blue**), and non-Newtonian variable, $\breve{Q}_{\theta,1}(0)$ (**green**), contributions to volumetric flow rate evaluating at $\theta = 0$, *versus* ξ_i, with $\xi_o = 0.02, 0.04, 0.06, 0.08, 0.10$ isopleths [Eqs. (129) and (130)].

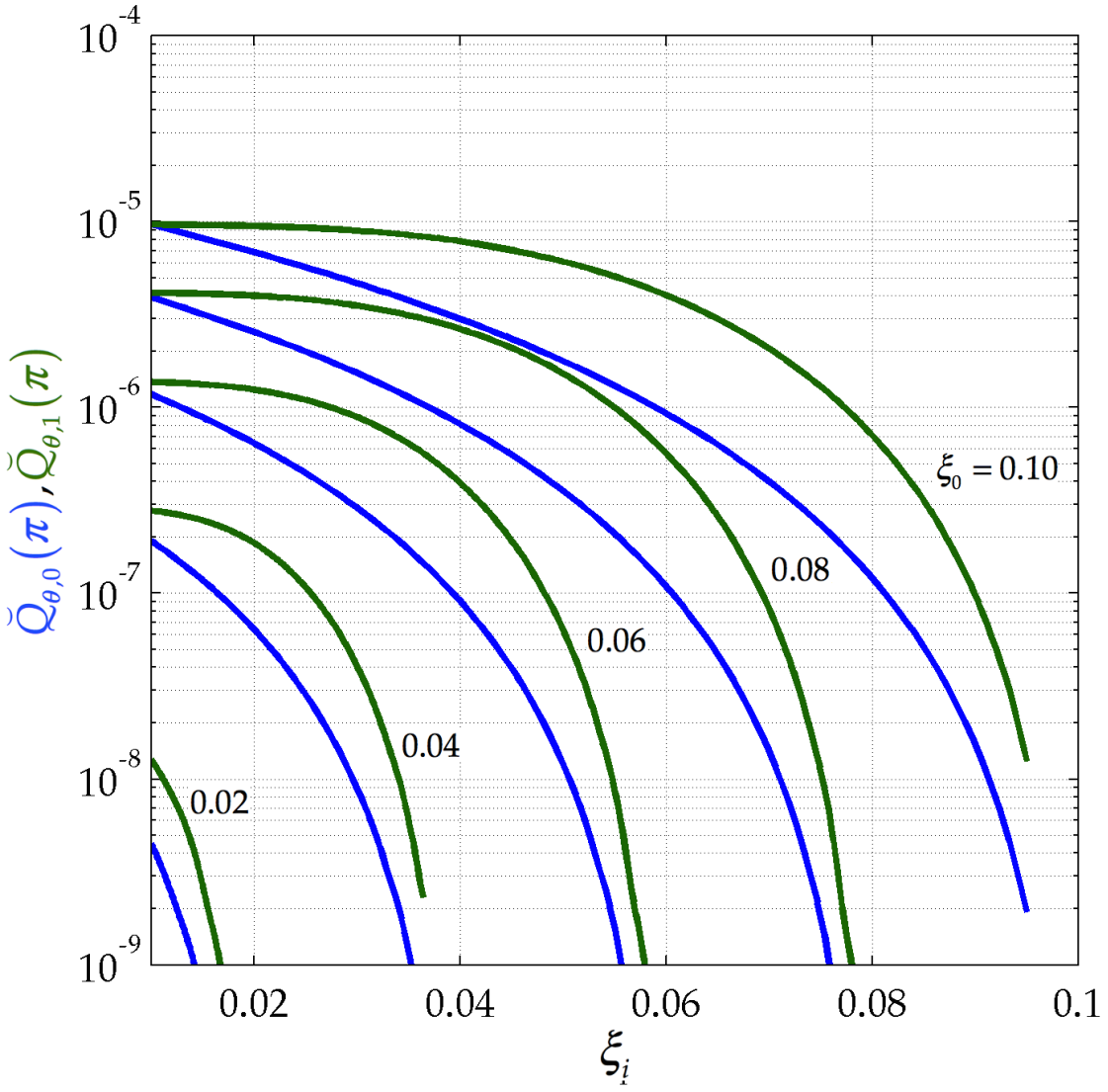

Figure 25: Newtonian, $\breve{Q}_{\theta,0}(\pi)$ (**blue**), and non-Newtonian variable, $\breve{Q}_{\theta,1}(\pi)$ (**green**), contributions to volumetric flow rate evaluating at $\theta = \pi$, *versus* ξ_i, with $\xi_o = 0.02, 0.04, 0.06, 0.08, 0.10$ isopleths [Eqs. (129) and (130)].

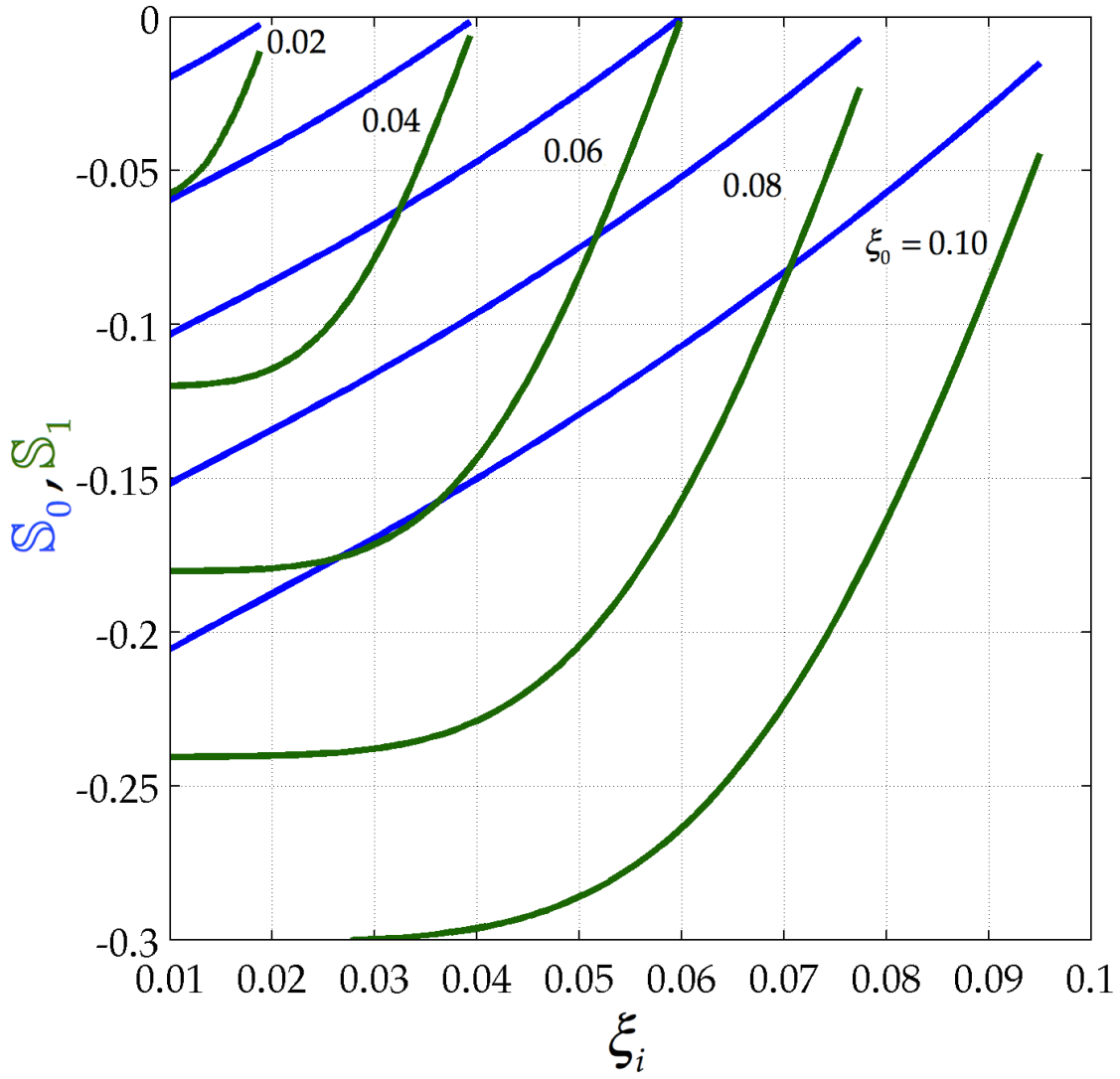

Figure 26: Newtonian, $\mathbb{S}_0$ (**blue**), and non-Newtonian variable, $\mathbb{S}_1$ (**green**), contribution to maximum shear stress *versus* ξ_i, with $\xi_o = 0.02, 0.04, 0.06, 0.08, 0.10$ isopleths [Eqs. (139) and (140)]

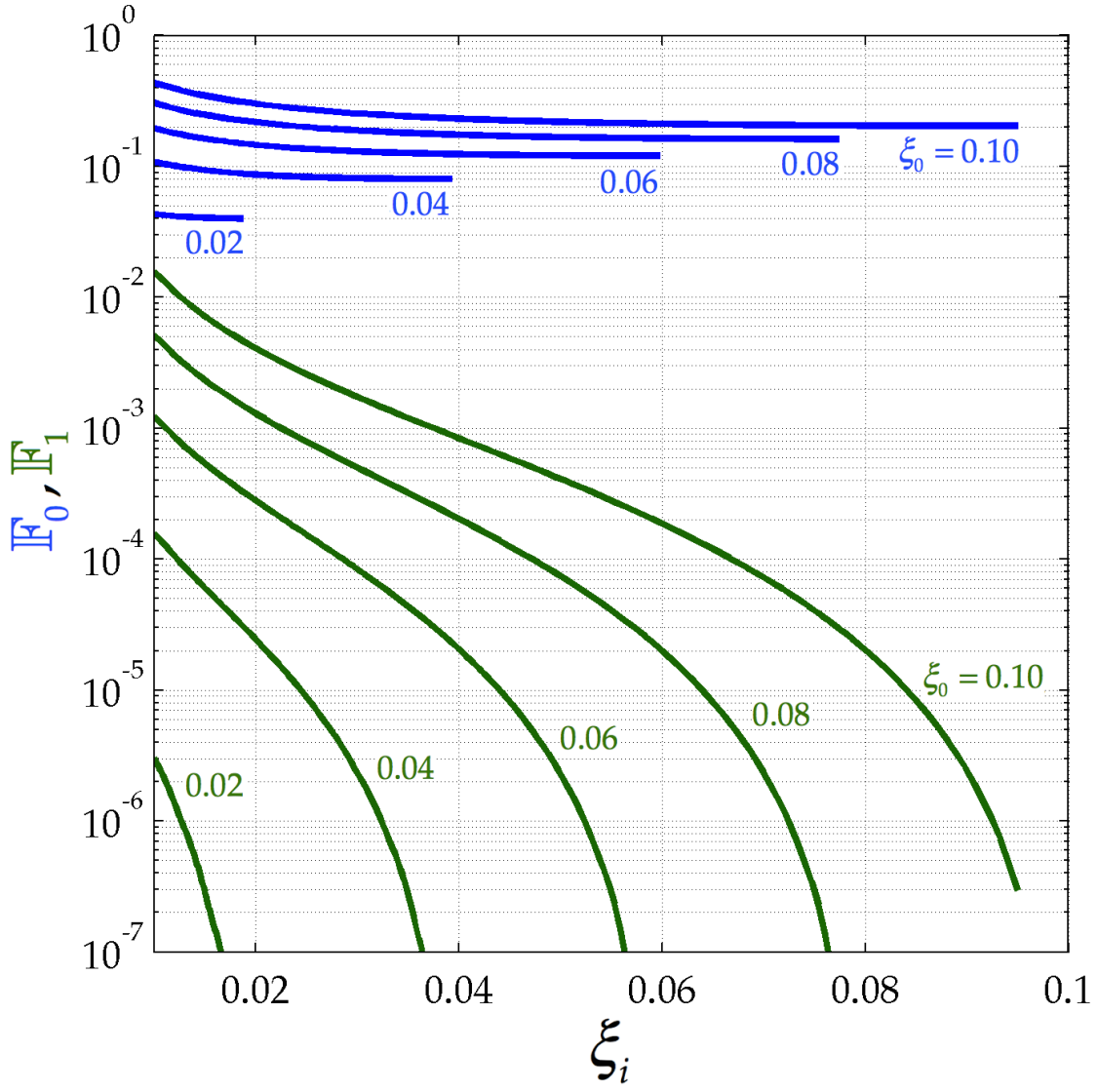

Figure 27: Newtonian, $\mathbb{F}_0$ (**blue**), and non-Newtonian variable, $\mathbb{F}_1$ (**green**), contribution to axial force *versus* ξ_i, with $\xi_o = 0.02, 0.04, 0.06, 0.08, 0.10$ isopleths [Eqs. (148) and (149)].

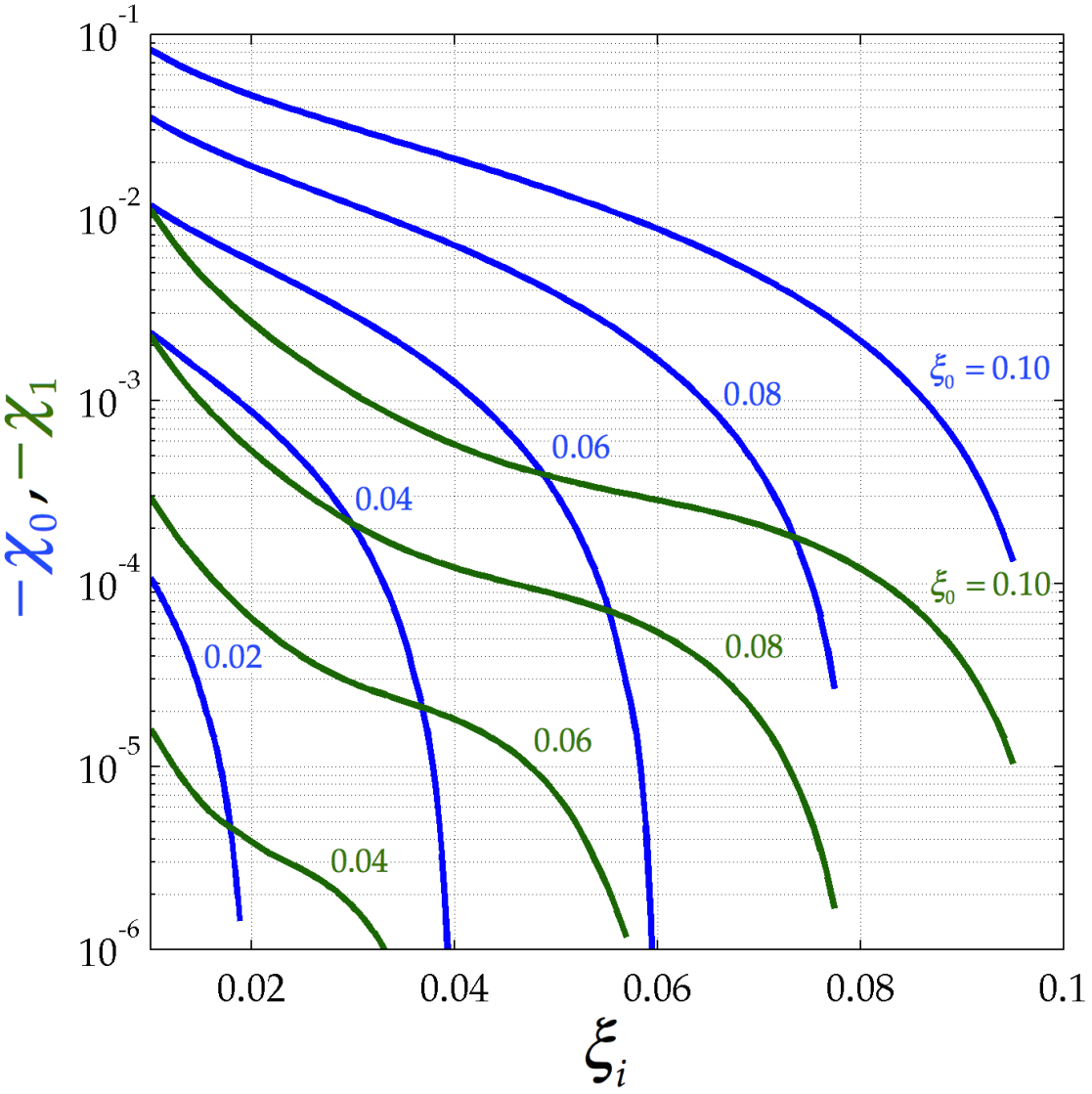

Figure 28: Newtonian, χ_0 (**blue**), and non-Newtonian variable, χ_1 (**green**), contribution to lateral force coefficient *versus* ξ_i, with $\xi_o = 0.02, 0.04, 0.06, 0.08, 0.10$ isopleths [Eq. (162) and (163)].

Chapter 5 Extrudate Knuckling from Viscoelasticity

In this Chapter, we undertake a detailed examination of our previous result for the extrudate shape (see Section 4.2) and discover extrudate knuckling. We investigate and eventually explain extrudate knuckling, and thus a new explanation for pipe knuckling. We develop a map to help plastics engineers predict the extrudate shape, including extrudate knuckles, and then from the mass balance over the postdie region, to predict the extrudate shape entering the cooling chamber. We include a detailed dimensional worked example to help process engineers suppress extrudate knuckling.

Rewriting Eqs. (122)-(124) [using Eq. (125)] from our previous results in Subsection 4.2, we get:

$$\left\langle \breve{v}_z \right\rangle_\theta = \left\langle \breve{v}_z \right\rangle_{\theta,0} + \left(1-\sigma\right) S \left\langle \breve{v}_z \right\rangle_{\theta,1} \tag{193}$$

where:

$$\left\langle \breve{v}_z \right\rangle_{\theta,0} \equiv \frac{f^2}{\pi\left(1-\kappa^2\right)} \int_{\xi_i}^{\xi_o} \frac{\xi}{\left(1+\xi^2-2\xi\cos\theta\right)^2} v_0 \, d\xi \tag{194}$$

$$\left\langle \breve{v}_z \right\rangle_{\theta,1} \equiv \frac{f^2}{\pi\left(1-\kappa^2\right)} \int_{\xi_i}^{\xi_o} \frac{\xi}{\left(1+\xi^2-2\xi\cos\theta\right)^2} v_1 \, d\xi \tag{195}$$

We will use Eq. (193) in Section 5.1 to investigate, and to eventually explain, extrudate knuckling.

5.1 Extrudate Knuckling

In this section, we develop a map to help plastics engineers predict extrudate shape, including extrudate knuckles, and then, from the mass balance, to predict the pipe shape (in Section 5.2).

To test for the presence of extrudate knuckles, we begin by differentiating Eq. (193) once:

$$\frac{\partial\langle\breve{v}_z\rangle_\theta}{\partial\theta}=\frac{\partial\langle\breve{v}_z\rangle_{\theta,0}}{\partial\theta}+(1-\sigma)S\frac{\partial\langle\breve{v}_z\rangle_{\theta,1}}{\partial\theta} \tag{196}$$

and twice to give:

$$\frac{\partial^2\langle\breve{v}_z\rangle_\theta}{\partial\theta^2}=\frac{\partial^2\langle\breve{v}_z\rangle_{\theta,0}}{\partial\theta^2}+(1-\sigma)S\frac{\partial^2\langle\breve{v}_z\rangle_{\theta,1}}{\partial\theta^2} \tag{197}$$

Setting the left side of Eq. (196) to zero gives:

$$\frac{\partial\langle\breve{v}_z\rangle_{\theta,0}}{\partial\theta}+(1-\sigma)S\frac{\partial\langle\breve{v}_z\rangle_{\theta,1}}{\partial\theta}=0 \tag{198}$$

We will use this equation to solve for the angular position of the extrudate knuckles, θ_K. We will further identify under which process condition extrudate knuckles arise.

We next calculate both of the derivatives in Eq. (198). Substituting Eqs. (75) and (92) into Eqs. (194) and (195) gives:

$$\langle\breve{v}_z\rangle_{\theta,0}=\frac{f^2}{\pi(1-\kappa^2)}\int_{\xi_i}^{\xi_o}\frac{\xi\left[\sum_{n=0}^{\infty}\phi_n\cos n\theta+\frac{-1}{1-2\xi\cos\theta+\xi^2}\right]}{\left(1+\xi^2-2\xi\cos\theta\right)^2}d\xi \tag{199}$$

$$\left\langle \breve{v}_z \right\rangle_{\theta,1} = \frac{f^2}{\pi\left(1-\kappa^2\right)} \int_{\xi_i}^{\xi_o} \frac{\xi \sum_{n=0}^{5} \psi_n \cos n\theta}{\left(1+\xi^2-2\xi\cos\theta\right)^2} d\xi \tag{200}$$

Differentiating Eqs. (199) and (200), once gives:

$$\frac{\partial \left\langle \breve{v}_z \right\rangle_{\theta,0}}{\partial\theta} = \frac{f^2}{\pi\left(1-\kappa^2\right)} \int_{\xi_i}^{\xi_o} \left[\begin{array}{c} \dfrac{-\xi \sum_{n=1}^{\infty} n\phi_n \sin n\theta}{\left(1-2\xi\cos\theta+\xi^2\right)^2} + \dfrac{-4\xi^2 \sin\theta \sum_{n=0}^{\infty} \phi_n \cos n\theta}{\left(1-2\xi\cos\theta+\xi^2\right)^3} \\ + \dfrac{6\xi^2 \sin\theta}{\left(1-2\xi\cos\theta+\xi^2\right)^4} \end{array} \right] d\xi \tag{201}$$

$$\frac{\partial \left\langle \breve{v}_z \right\rangle_{\theta,1}}{\partial\theta} = \frac{f^2}{\pi\left(1-\kappa^2\right)} \int_{\xi_i}^{\xi_o} \left[\frac{-\xi \sum_{n=1}^{5} n\psi_n \sin n\theta}{\left(1-2\xi\cos\theta+\xi^2\right)^2} + \frac{-4\xi^2 \sin\theta \sum_{n=0}^{5} \psi_n \cos n\theta}{\left(1-2\xi\cos\theta+\xi^2\right)^3} \right] d\xi \tag{202}$$

and twice:

$$\frac{\partial^2 \left\langle \breve{v}_z \right\rangle_{\theta,0}}{\partial\theta^2} = \frac{f^2}{\pi\left(1-\kappa^2\right)} \int_{\xi_i}^{\xi_o} \left[\begin{array}{c} -\dfrac{\xi \sum_{n=1}^{\infty} n^2 \phi_n \cos n\theta}{\left(1-2\xi\cos\theta+\xi^2\right)^2} + \xi^2 \dfrac{8\sin\theta \sum_{n=1}^{\infty} n\phi_n \sin n\theta - 4\cos\theta \sum_{n=0}^{\infty} \phi_n \cos n\theta}{\left(1-2\xi\cos\theta+\xi^2\right)^3} \\ + \dfrac{6\xi^2\cos\theta + 24\xi^3 \sin^2\theta \sum_{n=0}^{\infty} \phi_n \cos n\theta}{\left(1-2\xi\cos\theta+\xi^2\right)^4} - \dfrac{48\xi^3 \sin^2\theta}{\left(1-2\xi\cos\theta+\xi^2\right)^5} \end{array} \right] d\xi \tag{203}$$

$$\frac{\partial^2 \left\langle \breve{v}_z \right\rangle_{\theta,1}}{\partial\theta^2} = \frac{f^2}{\pi\left(1-\kappa^2\right)} \int_{\xi_i}^{\xi_o} \left[\begin{array}{c} -\dfrac{\xi \sum_{n=1}^{5} n^2 \psi_n \cos n\theta}{\left(1-2\xi\cos\theta+\xi^2\right)^2} + \dfrac{24\xi^3 \sin^2\theta \sum_{n=1}^{5} \psi_n \cos n\theta}{\left(1-2\xi\cos\theta+\xi^2\right)^4} \\ + \xi^2 \dfrac{8\sin\theta \sum_{n=1}^{5} n\psi_n \sin n\theta - 4\cos\theta \sum_{n=1}^{5} \psi_n \cos n\theta}{\left(1-2\xi\cos\theta+\xi^2\right)^3} \end{array} \right] d\xi \tag{204}$$

Substituting both Eqs. (201) and (202) into Eq. (198) gives:

$$\int_{\xi_i}^{\xi_o}\left[\frac{-\xi\sum_{n=1}^{\infty} n\phi_n \sin n\theta_K}{\left(1-2\xi\cos\theta_K+\xi^2\right)^2}+\frac{-4\xi^2\sin\theta_K\sum_{n=0}^{\infty}\phi_n\cos n\theta_K}{\left(1-2\xi\cos\theta_K+\xi^2\right)^3}+\frac{6\xi^2\sin\theta_K}{\left(1-2\xi\cos\theta_K+\xi^2\right)^4}\right]d\xi$$
$$+(1-\sigma)S\int_{\xi_i}^{\xi_o}\left[\frac{-\xi\sum_{n=0}^{5} n\psi_n \sin n\theta_K}{\left(1-2\xi\cos\theta_K+\xi^2\right)^2}+\frac{-4\xi^2\sin\theta_K\sum_{n=0}^{5}\psi_n\cos n\theta_K}{\left(1-2\xi\cos\theta_K+\xi^2\right)^3}\right]d\xi=0 \tag{205}$$

When the solution to Eq. (205) also satisfies both:

$$\frac{\partial^2\langle\breve{v}_z\rangle_{\theta,0}}{\partial\theta^2}+(1-\sigma)S\frac{\partial^2\langle\breve{v}_z\rangle_{\theta,1}}{\partial\theta^2}<0 \tag{206}$$

where $\partial^2\langle\breve{v}_z\rangle_{\theta,0}/\partial\theta^2$ and $\partial^2\langle\breve{v}_z\rangle_{\theta,1}/\partial\theta^2$ are given in Eqs. (203) and (204), and, in cylindrical coordinates:

$$\frac{\pi}{2}\le\tilde{\theta}_K<\pi \tag{207}$$

then the thickest parts of the extrudate are in the lower quadrants, and thus extrudate knuckles exist. Eq. (207) can be rewritten in eccentric cylindrical coordinates as:

$$\arccos\left(\frac{2\xi_o}{1+\xi_o^2}\right)\le\theta_K<\arccos\left(\frac{\left(1+\xi_o^2\right)\left(-\frac{R_o}{a}+\frac{1}{1-\xi_o^2}\right)-1}{2\xi_o\left(-\frac{R_o}{a}+\frac{1}{1-\xi_o^2}\right)-\xi_o}\right) \tag{208}$$

Eqs. (205), (206) and (207) [or Eq. (208)] are the criterion for extrudate knuckling. This criterion is the main result of this thesis.

5.2 Postdie Region

In this section, we perform a mass balance on the postdie region. By *postdie* region, we mean the section of the manufacturing line between the die and the cooling chamber, where the annular melt undergoes extensional flow (see Figure 1 and Figure 3; [103,104,105]). Our mass balance on the postdie region gives the shape of the melt entering the cooling chamber as a function of the shape of the viscoelastic melt emerging from the eccentric annular die.

Since the postdie region involves little cooling, and thus no solidification, the melt density is nearly constant in this region. The mass balance at any particular $\tilde{\theta}$ is thus given by (see Appendix IV for the relationship between θ and $\tilde{\theta}$):

$$\left\langle v_z \right\rangle_{\tilde{\theta}} dA_{\mathrm{e}\tilde{\theta}} = V dA_{\mathrm{p}\tilde{\theta}} \tag{209}$$

which we then rearrange and, using Table 2, adimensionalize as:

$$\frac{\left\langle v_z \right\rangle_{\tilde{\theta}}}{V} = \frac{dA_{\mathrm{p}\tilde{\theta}}}{dA_{\mathrm{e}\tilde{\theta}}} = \frac{\left\langle \breve{v}_z \right\rangle_{\tilde{\theta}}}{\breve{V}} \tag{210}$$

The differential area for each slice of the extrudate entering cooling chamber in the postdie region is given by (see Fig. A.8-1. in [40]):

$$dA_{\mathrm{p}\tilde{\theta}} = \int_{R_{\mathrm{ip}}(\tilde{\theta})}^{R_{\mathrm{op}}} r\, dr = \frac{R_{\mathrm{op}}^2 - R_{\mathrm{ip}}^2\left(\tilde{\theta}\right)}{2} \tag{211}$$

and, for the one leaving the extrusion die, by:

$$dA_{\mathrm{e}\tilde{\theta}} = \frac{R_o^2 - R_i^2\left(\tilde{\theta}\right)}{2} \tag{212}$$

Substituting Eqs. (211) and (212) into Eq. (210), and then solving for $R_{\mathrm{ip}}\left(\tilde{\theta}\right)$ gives:

$$R_{ip}\left(\tilde{\theta}\right)=\sqrt{R_{op}^2-\mathrm{DDR}\left[R_o^2-R_i^2\left(\tilde{\theta}\right)\right]} \tag{213}$$

where the drawdown ratio is defined by:

$$\mathrm{DDR}\equiv\left\langle \breve{v}_z\right\rangle_{\tilde{\theta}}/\breve{V} \tag{214}$$

Eq. (213) is thus the main result of this section. We will use Eq. (213) to convert from extrudate shape to pipe shape in Figure 29.

5.3 Results

Using Eq. (201), we plot Figure 30, from which we learn that a Newtonian extrudate will never knuckle. Extrudate knuckling thus comes from the non-Newtonian contribution. Using Eq. (202), we plot Figure 31, from which we learn that the fluid elasticity, identified by σ, causes extrudate knuckling. This is why, to avoid knuckles, engineers must sometimes reformulate the plastics.

From Figure 30 and Figure 31, we also learn that extrudate knuckling never happens in the upper quadrants ($\pi/2>\tilde{\theta}>3\pi/2$) of the pipe. Thus, when extrudate knuckling does happen, it always happens in the lower quadrants ($\pi/2\le\tilde{\theta}\le 3\pi/2$). These findings agree with industrial experience.

From Figure 32, we learn that the critical value of $(1-\sigma)S$ above which extrudate knuckling happens, $\mathbb{K}$, descends with ξ_i and increases with ξ_o. For any pair (ξ_i,ξ_o), the value of $(1-\sigma)S$ must subceed the value of $\mathbb{K}$ interpolated from Figure 32:

$$(1-\sigma)S<\mathbb{K} \tag{215}$$

which is working inequality for suppressing extrudate knuckling. Eq. (215), along with its companion Figure 32, illustrates the *extrudate knuckling criterion* (Eqs. (205), (206) and (207) [or Eq. (208)]), which is the main result of this thesis.

To deepen the reader's understanding of how Figure 32 was constructed, we provide Figure 33, and we recall:

$$\frac{\partial\langle\breve{v}_z\rangle_\theta}{\partial\theta}=\frac{\partial\langle\breve{v}_z\rangle_{\theta,0}}{\partial\theta}+(1-\sigma)S\frac{\partial\langle\breve{v}_z\rangle_{\theta,1}}{\partial\theta} \tag{196}$$

where $\partial\langle\breve{v}_z\rangle_\theta/\partial\theta$ is the extrudate shape gradient (ESG), $\partial\langle\breve{v}_z\rangle_{\theta,0}/\partial\theta$ is the Newtonian contribution to the ESG, and $\partial\langle\breve{v}_z\rangle_{\theta,1}/\partial\theta$ is part of the non-Newtonian contribution. Specifically, Figure 33 shows how one point, the **red** point on the ordinate $(\xi_i,\mathbb{K})=(0.01,0.018)$, in Figure 32 was obtained. When $\partial\langle\breve{v}_z\rangle_{\theta,0}/\partial\theta$ intersects $\partial\langle\breve{v}_z\rangle_{\theta,1}/\partial\theta$ at $\theta<\pi$, $(1-\sigma)S>\mathbb{K}$ (see, for example, the isopleth of $(1-\sigma)S=0.01$). When $\partial\langle\breve{v}_z\rangle_{\theta,0}/\partial\theta$ and $\partial\langle\breve{v}_z\rangle_{\theta,1}/\partial\theta$ do not intersect, $(1-\sigma)S<\mathbb{K}$ (see, for example, the isopleth of $(1-\sigma)S=0.001$). When $\partial\langle\breve{v}_z\rangle_{\theta,0}/\partial\theta$ intersects $\partial\langle\breve{v}_z\rangle_{\theta,1}/\partial\theta$ at precisely $\theta=\pi$, $(1-\sigma)S=\mathbb{K}$ (see the $(1-\sigma)S=0.00263=\mathbb{K}$ isopleth).

Figure 34 shows that extrudate knuckling, predicted by Eq. (205), happens in concert with a local maximum in pipe thickness at the bottom of the pipe. From Figure 34, we also learn that increasing $(1-\sigma)S$ worsens the extrudate knuckling. Figure 29 compares the initial condition normally assumed for numerical simulation of sag (**red** curve) [8], with the new initial condition that this thesis

offers (**blue** curve): the extrudate shape entering the cooling chamber (predicted by Eq. (213) [with Eq. (193)]). Specifically, from Figure 29, we see why the initial condition that is normally assumed for numerical simulation of sag over-predicts the pipe bottom thickness.

5.4 Worked Example

An engineer observes the pipe knuckling (shown in Figure 2) in high-density polyethylene pipe extrusion. For sag compensation, her mandrel has been shifted downward by $\delta = 0.0118\,\mathrm{m}$, with mandrel and die radii of $R_i = 0.351\mathrm{m}$ and $R_o = 0.440\mathrm{m}$. For her analysis, the engineer choses the corotational Maxwell model (see Subsection 2.2; also [44,45]), with $\eta_0 = 9.6\,\mathrm{MPa{\cdot}s}$ and $\lambda_1 = 2.38\,\mathrm{s}$ for her molten high-density polyethylene. Does extrudate knuckling cause her the knuckling that she observes in her fully solidified pipe (pipe knuckling)?

She first calculates the corresponding inner and outer contours by substituting R_i, R_o and δ into Eqs. (7), (79) and (81) to get:

$$a = 5.91\,\mathrm{m} \tag{216}$$

$$\xi_i = 0.0592 \tag{217}$$

and:

$$\xi_o = 0.0740 \tag{218}$$

She measures the pressure drop per unit length across her annular die of:

$$P = 8.46\times10^5\,\mathrm{Pa/m} \tag{219}$$

Using Eq. (219) and the given material properties to calculate the non-Newtonian coefficient, $(1-\sigma)S$, gives:

$$(1-\sigma)S = \frac{(2.38\,\mathrm{s})^2 (5.91\,\mathrm{m})^2 (8.46\times10^5\,\mathrm{Pa/m})^2}{16(9.6\times10^6\,\mathrm{Pa\cdot s})^2} = 0.0960 \tag{220}$$

Next, she uses Eqs. (217) and (218) to interpolate the critical value of $(1-\sigma)S$ from Figure 32 to get:

$$\mathbb{K} = 0.00557 \tag{221}$$

Since this is smaller than 0.0246, she concludes that her pipe knuckling is indeed caused by the knuckling of her extrudate.

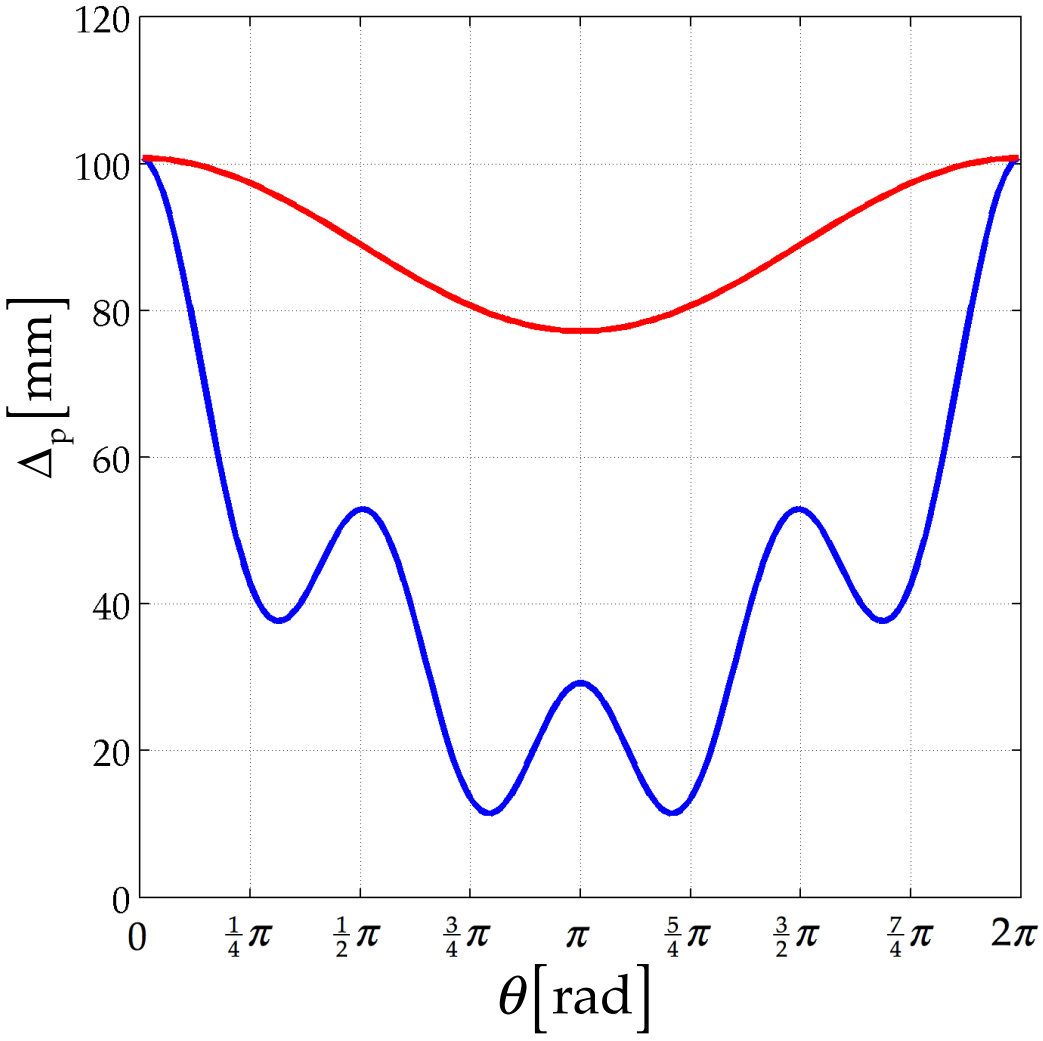

Figure 29: Thickness distribution of the extrudate entering the cooling chamber, $\Delta_p = R_{op} - R_{ip}$, (**blue**) predicted from Eq. (213) [with Eq. (193)] using $P = 8.46\times10^5\,\text{Pa/m}$, $\eta_0 = 9.6\,\text{MPa·s}$, $V = 1.98\times10^{-5}\,\text{m/s}$, $R_i = 0.351\,\text{m}$, $R_o = 0.44\,\text{m}$, $R_{op} = 0.44\,\text{m}$, $\delta = 0.0118\,\text{m}$, $\lambda_1 = 2.38\,\text{s}$, $\lambda_2 = \mu_0 = \mu_1 = \mu_2 = \nu_1 = \nu_2 = 0$ *versus* the die shape (**red**).

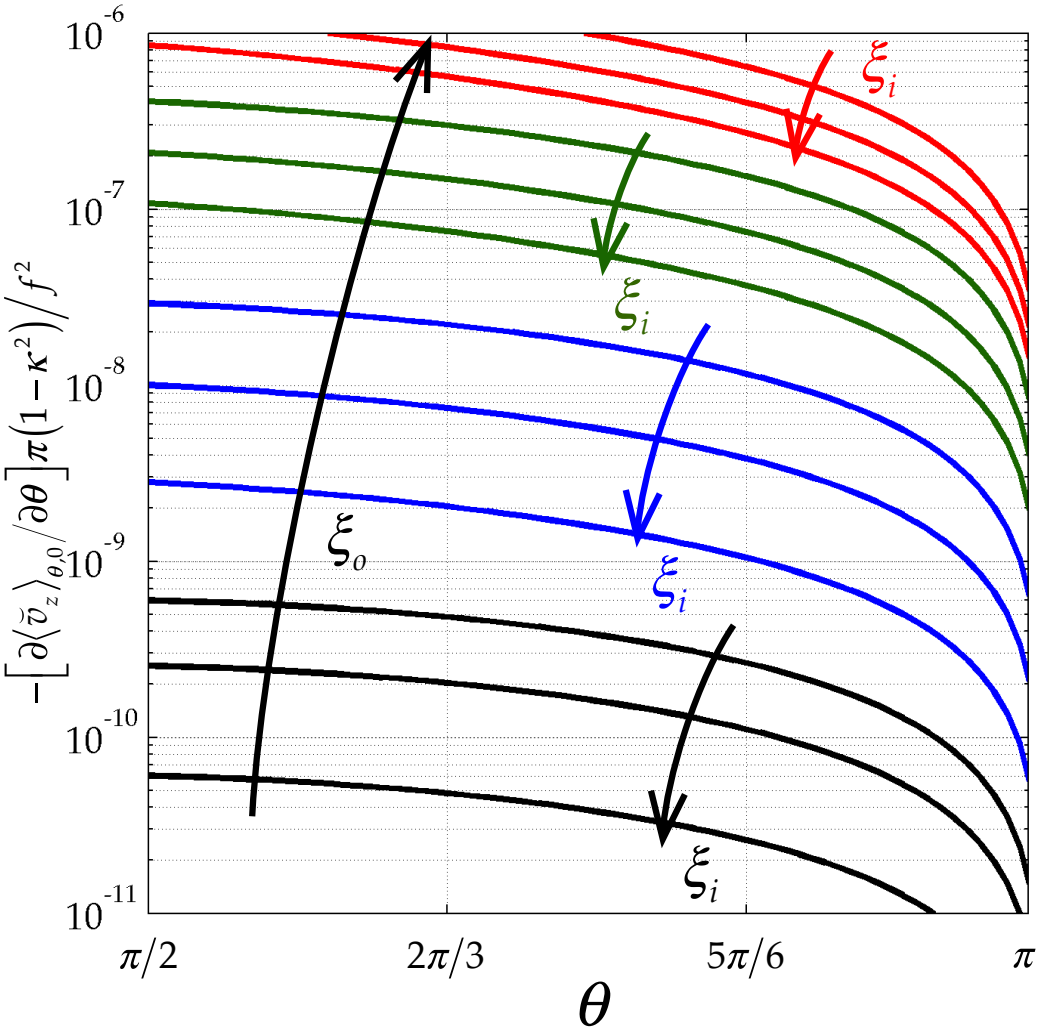

Figure 30: Newtonian contribution to the extrudate shape gradient. Four sets of increasing parametrized curves of ξ_i from top to bottom [Eq. (201)]. ξ_o is increasing from bottom to top.

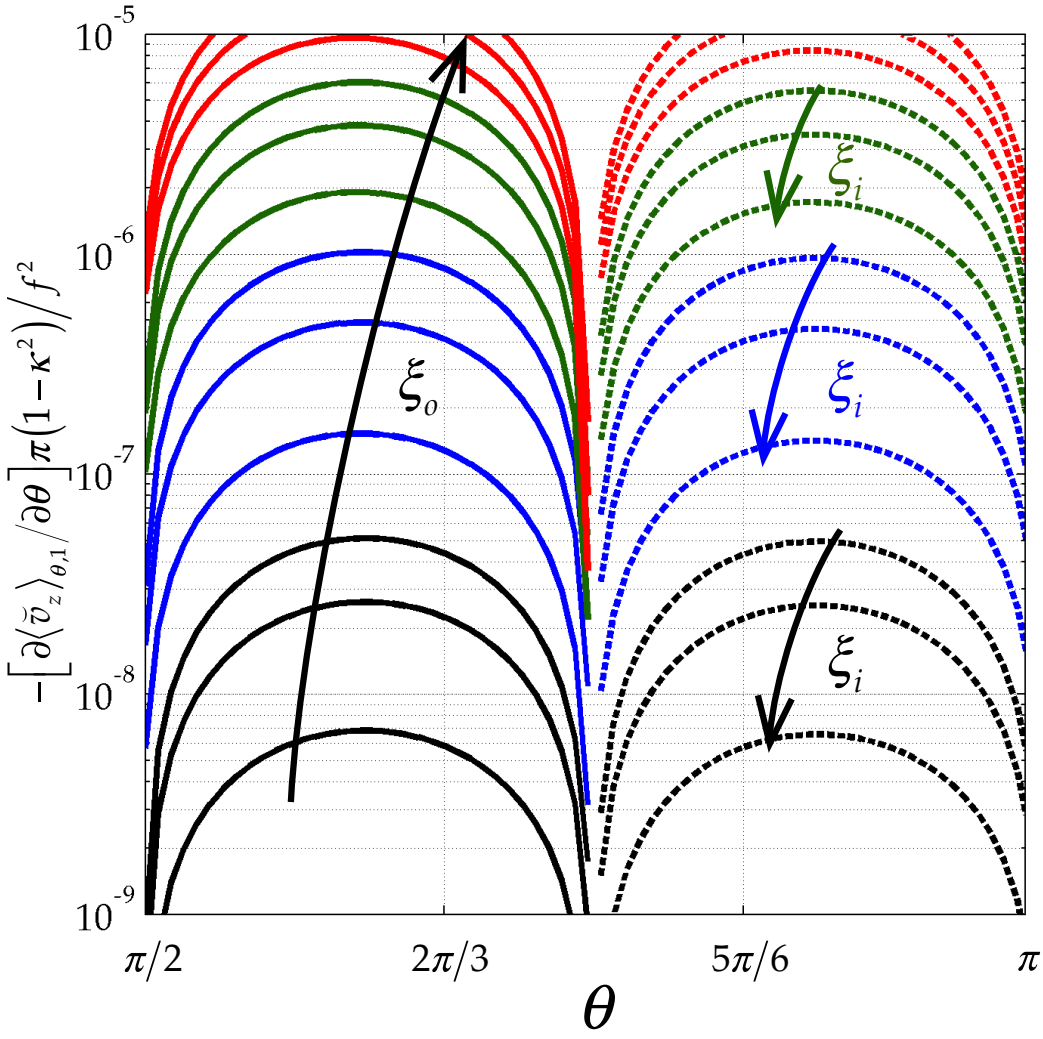

Figure 31: Non-Newtonian contribution to extrudate shape gradient. Four sets of increasing parametrized curves of ξ_i (top to bottom). ξ_o is increasing from bottom to top. Dashed curves are for the negative part of $-\partial\langle\breve{v}\rangle_{\theta,1}/\partial\theta$ [Eq. (202)].

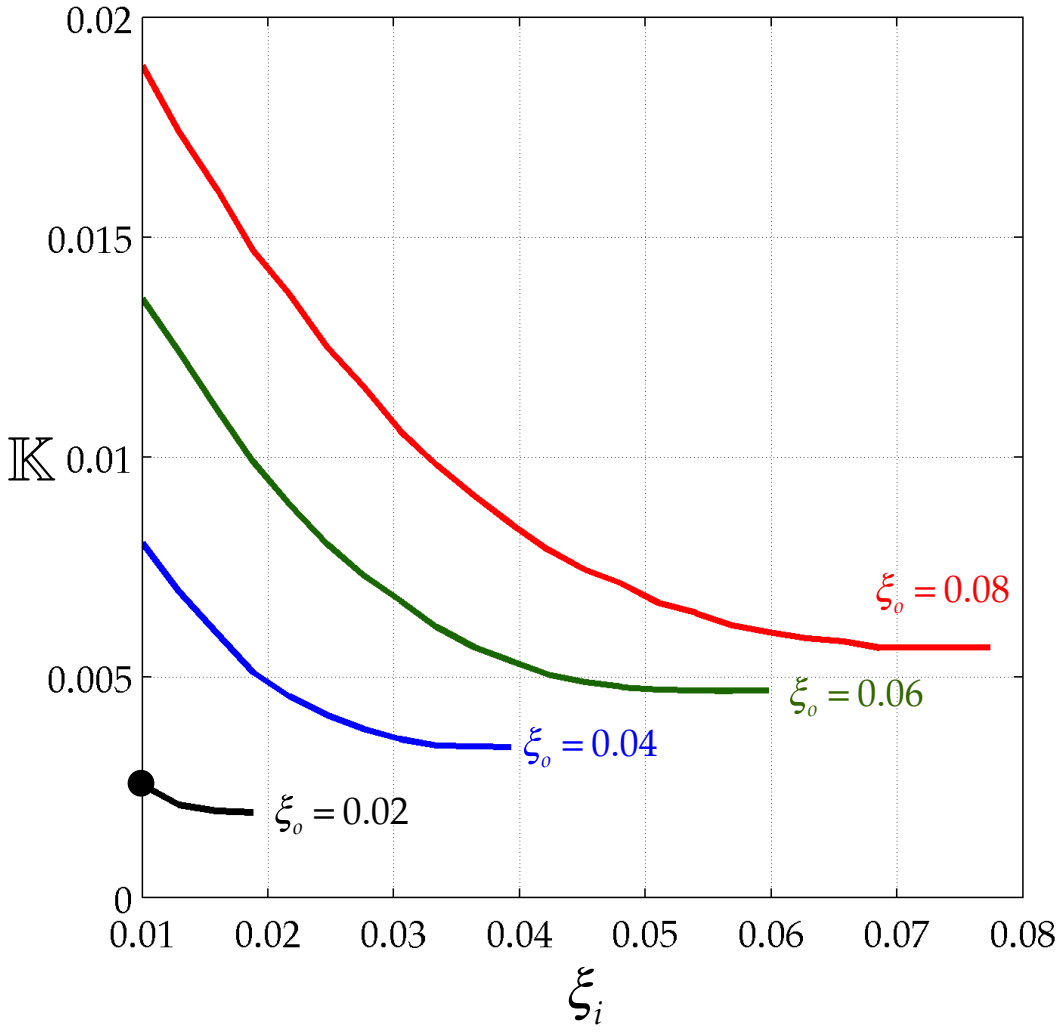

Figure 32: Knuckling suppression map of the critical values of $(1-\sigma)S$, $\mathbb{K}$, *versus* inner contour, ξ_i, parametrized with ξ_o [Eq. (205)]. **Black** dot illustrates the critical value for Figure 33.

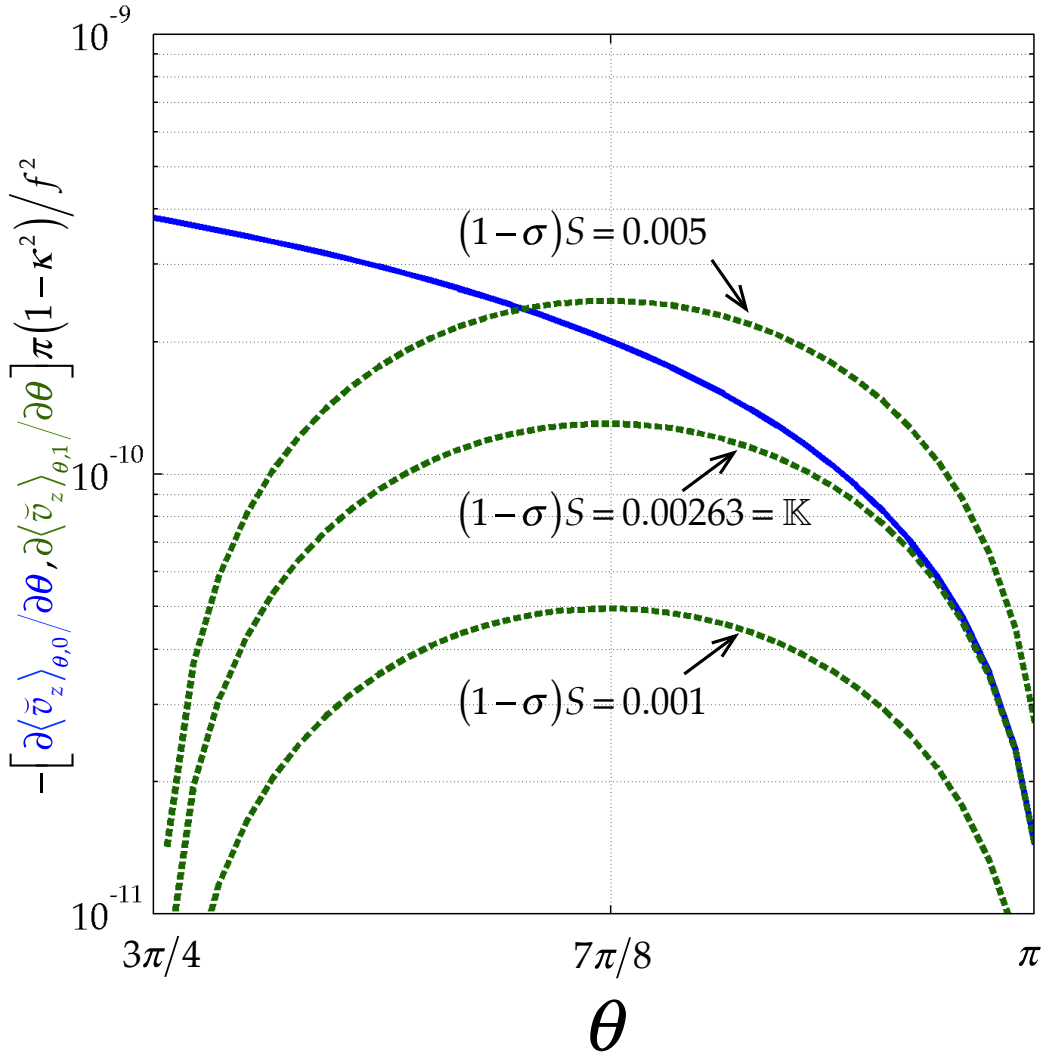

Figure 33: Suppressing extrudate knuckles. **Blue** curves are the Newtonian (negative) contribution to extrudate shape gradient [Eq. (201)], and the **green** ones, non-Newtonian [Eq. (202)], using $(\xi_i, \xi_o) = (0.01, 0.02)$. Critical value is $\mathbb{K} = 0.00263$. Suppressing by decreasing $(1-\sigma)S$. Dashed curves are for the negative part of $-\partial\langle\tilde{v}\rangle_{\theta,1}/\partial\theta$.

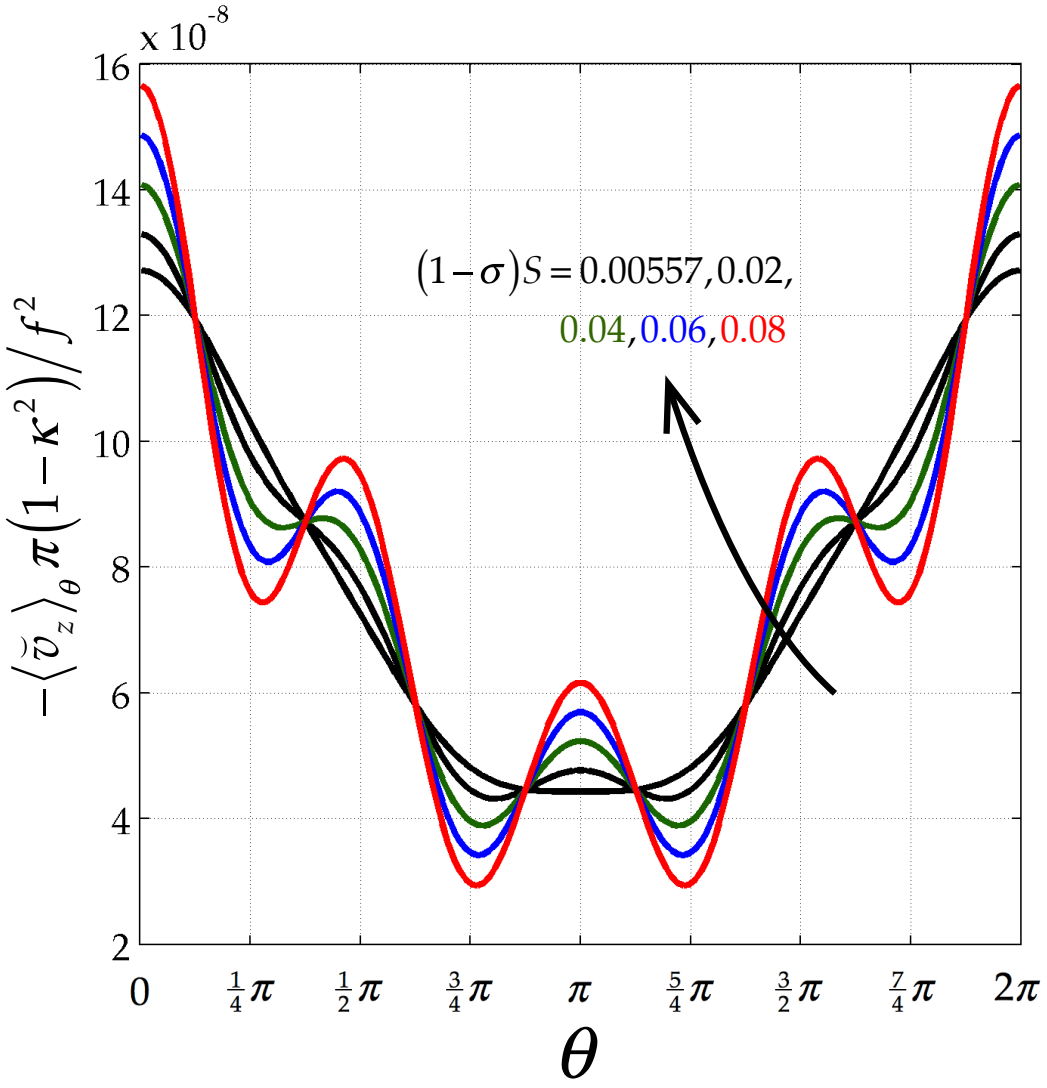

Figure 34: Average velocity of each slice θ *versus* eccentric angular position, θ, with curves of constant $(1-\sigma)S = 0.00557$, 0.02, 0.04, 0.06, 0.08 [Eq. (205)]. The smoothest curve, $(1-\sigma)S = \mathbb{K} = 0.00557$, represents the critical extrudate knuckling.

Chapter 6 Conclusion

We report a new expression for the lateral force exerted on a pipe extrusion die by an elastic liquid obeying any model in the Oldroyd 8-constant framework [Eq. (160) with Eqs. (162)-(163)]. Our analysis corrects the previous contribution [see rapid convergence approximation in Eq. (88)] due to Jones [16]. For Newtonian or shear-thinning fluids ($\sigma \leq 1$), we find the sign of the lateral force to be decentering. We find that the physics of pressure driven flow of a non-Newtonian fluid through an eccentric annulus revolves, rather beautifully, around the product $(1-\sigma)S$.

We have succeeded in splitting each quantity calculated in this thesis, including the (i) throughput, (ii) extrudate shape, (iii) stresses in the melt, and (iv) forces on the mandrel, F_x and F_z, into both Newtonian and non-Newtonian contributions [see subhead to Section 3.2 above]. Furthermore, each of these contributions includes a factor that depends only on geometry. This factorability allows us to summarize our results into convenient graphs for those solving pipe extrusion problems. Specifically, our graphs help engineers address problems arising when plastic pipe is extruded from eccentric dies, and precisely for the (i) throughput (Figure 23), (ii) extrudate shape [Figure 24, Figure 25], (iii) stresses in the melt (Figure 26), and (iv) forces on the mandrel, F_x (Figure 27) and F_z (Figure 28). The factorability of our answers arises by virtue of our choice of the polymer process partitioning method, a method perfectly suited to the rich diversity of constitutive equations encompassed by the Oldroyd 8-constant constitutive

framework (see Section 2.2 above). The polymer process partitioning method involves splitting the velocity field into the Newtonian and non-Newtonian contributions.

We further employ our analytical solution for the pressure-driven flow of a non-Newtonian fluid through an eccentric annulus to analyze the shape of extrudate emerging from a pipe die. We find that extrudate knuckling is governed by (i) melt elasticity, (ii) pressure gradient across the die and (iii) die geometry including especially its eccentricity (without which, we find that, no extrudate knuckling can arise, see Fig. 3 of [8]). Further, we arrive at a new criterion for extrudate knuckling (Eqs. (205), (206) and (207) [or Eq. (208)]). This criterion yields a working inequality, Eq. (215), for suppressing extrudate knuckling. Figure 32 illustrates this new working inequality, and plastics engineers can use it to predict extrudate knuckling.

This novel analysis of knuckling offers significant improvement over the initial condition normally used for numerical simulation of sag in plastic pipe extrusion. The new initial condition not only includes extrudate knuckling, but also promises a solution to the over-prediction of the pipe bottom thickness (see Figure 29; and Fig. 6 of [8]).

Though the polymer process partitioning method has been called "complex mathematically" (see last paragraph, p. 125 of [33]), we conclude that the especially useful form of the results make its complexity worthwhile. We produce this thesis with detail sufficient for graduate students to teach themselves the polymer process partitioning method, and to deepen their

understanding of polymer flow through straight eccentric annular dies. Further, we provide the following worked examples to teach practitioners how to use our results to help them extrude plastic pipe from eccentric dies.

We now turn our attention to the future. We recommend combining our velocity profile [Eq. (62) with Eqs. (75) through (78) and with Eqs. (92) through (273)] with the energy equation in eccentric cylindrical coordinates (Eq. (19) of [30]) to explore the role of melt viscoelasticity on the temperature rise in eccentric annular pipe die.

Some special cases of the Oldroyd 8-constant model (corotational Maxwell or corotational Jeffreys), are used with multiple relaxation times, λ_1. Extending the results of this work to multiple λ_1 might thus be a useful next step, and for this, we would begin with the Spriggs relations (see Eqs. (6.1-14) and (6.1-15) of [31]). Of course, other special cases of the Oldroyd 8-constant model (Johnson-Segalman or Gordon-Schowalter) are often useful without extension to multiple λ_1. As a practical matter, we would expect our single λ_1 results to be immediately useful by replacing λ_1 with some average value.

Finally, we would expect our revised polymer process partitioning method to be equally useful for the analysis of the wire coating, where the wire and the die are eccentric [33].

References

1 Giacomin, A.J., T. Habinak and S.R. Doshi, "Dies for Pipe Extrusion Which Compensate for Gravity Flow," Proceedings, Polymer Processing Society, Fourth Annual Meeting, Orlando, FL (May 8-11, 1988), p. 4/15.

2 Githuku, D.N. and A.J. Giacomin, "A Spectral Element Simulation of Gravitational Flow During Plastic Pipe Extrusion," *Journal of Engineering Materials and Technology*, **115**(4), 433–439 (1993).

3 Githuku, D.N. and A.J. Giacomin, "Elimination of Sag in Plastic Pipe Extrusion," *International Polymer Processing*, **VII**(2), 140–143 (1992).

4 Githuku, D.N. and Giacomin, A.J., "Elimination of Sag in Plastic Pipe Extrusion," Proceedings, Polymer Processing Society, Seventh Annual Meeting, Hamilton, CANADA (April 21-24, 1991), p. 260.

5 Pittman, J.F.T. and I.A. Farah, "Production of Pipe with Uniform Wall Thickness: How to Compensate for Gravity Sag," *International Polymer Processing*, **15**(3), 260–267 (2000).

6 Giacomin, A.J., and S.R. Doshi, "Analysis of Slump in Plastic Pipe Extrusion," In *SPE Tech. Paper*, **XXXIV**, *Society of Plastics Engineers, Proc. 46th Annual Tech. Conf. & Exhib., Atlanta, GA*, pp. 38–40 (1988).

7 Githuku, D.N., "Simulation of Sag in Plastic Pipe Extrusion," PhD Thesis, Texas A&M University, Mechanical Engineering Dept., College Station, TX (1992).

8 Githuku, D.N. and A.J. Giacomin, "Simulation of Slump in Plastic Pipe Extrusion," *Journal of Engineering Materials and Technology*, **114**(1), 81–83 (1992).

9 Githuku, D.N. and A.J. Giacomin, "Heat Transfer Considerations in Gravitational Flows During Plastic Pipe Extrusion," Proc., First International Conference on Transport Phenomena in Processing, Pacific Institute for Thermal Engineering, Honolulu, HI (March 22-26, 1992), S.I. Guceri, ed., Technomic Publishers Inc., Lancaster, PA (1992), pp. 997–1012.

10 Kolitawong, C., A.J. Giacomin and U. Nontakaew, "Viscous Dissipation in Plastic Pipe Extrusion," *Polymer Engineering & Science*, **53**(10), 2205–2218 (2013).

11 Pittman, J.F.T., G.P. Whitham, S. Beech and D. Gwynn, "Cooling and Wall Thickness Uniformity in Plastic Pipe Manufacture: An Experimental Study and Computer Simulations," *International Polymer Processing*, **9**(2), 130–140 (1994).

12 Pittman, J.F.T. and I.A. Farah, "Comprehensive Simulation of Cooling Process in Plastic Pipe Manufacture," *Plastics, Rubber and Composites: Processing and Applications*, **25**(6), 305–312 (1996).

13 Pittman, J.F.T., G.P. Whitham, and I.A. Farah, "Wall Thickness Uniformity in Plastic Pipes: Computer Simulations of the Effectiveness of Die Mandrel Offsetting and Pipe Rotation in Combatting Sag," *Polymer Engineering & Science*, **35**(11), 921–928 (1995).

14 Pittman, J.F.T. and I.A. Farah, "Computer Simulation of the Cooling Process in Plastic Pipe Manufacture, Including Sag, Thermal Stress and Morphology," *Proc. Plastic Pipes IX (Inst. Materials) Edinburgh* 364 (1995).

15 DesLauriers, P.J., M.P. McDaniel, D.C. Rohlfing, R.K. Krishnaswamy, S.J. Secora, E.A. Benham, P.L. Maeger, A.R. Wolfe, A.M. Sukhadia and B.B. Beaulieu,

"A Comparative Study of Multimodal vs. Bimodal Polyethylene Pipe Resins for PE-100 Applications," *Polymer Engineering & Science*, **45**(9), 1203–1213 (2005).

16 Jones, J.R., "Flow of Elastico-Viscous Liquids in Pipes with Cores (PART ONE)," *Journal de Mécanique*, **3**(1), 79–99 (March, 1964). Errata: In Eqs. (20) and (22a), "*a* const.," should be "a const.,"; In Eq. (15), "$9\sigma_2 \geq \sigma_1 \geq 0$" should be "$9\sigma_2 \geq \sigma_1 \geq 1$"; In Eq. (54), "$\psi_n =$" should be "$\Psi_n =$"; In Eq. (3.5), "$\omega_{ij} =$" should be "$\omega_{ik} =$"; In Eq. (16), "$Z^* = x + iy$" should be "$Z^* = x - iy$."; The first term on RHS of Eq. (23) "γ_2" should be "γ^2"; The expression for $F_1^{(4)}$ in Eq. (56), "r^{-4}" should be "$r-4$".

17 Jones, J.R., "Flow of Elastico-Viscous Liquids in Pipes with Cores (PART TWO)," *Journal de Mécanique*, **4**(1), 121–132 (1965).

18 Camilleri, C.J. and J.R. Jones, "The Effect of a Pressure Gradient on the Secondary Flow of Non-Newtonian Liquids between Non-Intersecting Cylinders," *Zeitschrift für angewandte Mathematik und Physik*, **17**(1), 78–90 (1966).

19 Jones, J.R. and R.S. Jones, "Flow of Elastico-Viscous Liquids in Pipes with Cores (Part III)," *Journal de Mécanique*, **5**(3), 375–395 (1966).

20 Jones, R.S., "Flow of an Elastico-Viscous Liquid in a Corrugated Pipe," *Journal de Mécanique*, **6**(3), 443–448 (1967).

21 Thomas, R.H. and K. Walters, "On the Flow of an Elastico-Viscous Liquid in a Curved Pipe under a Pressure Gradient," *Journal of Fluid Mechanics*, **16**(2), 228–242 (1963).

22 Thomas, R.H. and K. Walters, "On the flow of an Elastico-Viscous Liquid in a Curved Pipe of Elliptic Cross-Section under a Pressure-Gradient," *Journal of Fluid Mechanics*, **21**(1), 173–182 (1965).

23 Jones, J.R. and M.K. Lewis, "Non-Newtonian Effects in Flows of some Elastico-viscous Liquids in Curved Channels," *Zeitschrift für angewandte Mathematik und Physik*, **19**(5), 746–760 (1968).

24 Jones, J.R., "Remarks on Flows of Elastic Fluids along Cylindrical Boundaries," *Zeitschrift für angewandte Mathematik und Physik*, **53**(3), 518–532 (2002).

25 Camilleri, C.J. and J.R. Jones, "Secondary Flow of Non-Newtonian Liquids between Confocal Elliptic Cylinders in Relative Motion," *Zeitschrift für angewandte Mathematik und Physik*, **16**(5), 582–594 (1965).

26 Fischer, P, "Computer-Control on Extrusion Lines," *Kunststoffe-German Plastics*, **74**(7), 362–366 (1984).

27 Schmalzer, A.M., A.M. Mertz, D.N. Githuku and A.J. Giacomin, "Solidifying Plastic Pipe," *Journal of Advanced Engineering (先進工程學刊)*, **7**(3), 135–143 (2012).

28 Saengow, C., P. Poungthong, C. Kolitawong and A.J. Giacomin, "Plastic Pipe Solidification: Exact Solutions in Cylindrical Coordinates," *Journal of Advanced Engineering (先進工程學刊)*, **11**(4), (accepted in July, 2016).

29 Saengow, C., P. Poungthong, C. Kolitawong and A.J. Giacomin, "Plastic Pipe Solidification: Exact Solutions in Cylindrical Coordinates," PRG Report No.

019, QU-CHEE-PRG-TR--2015-19, Polymers Research Group, Chemical Engineering Dept., Queen's University, Kingston, CANADA (October, 2015), pp. 0–43.

30 Gilbert, P.H., C. Saengow and A.J. Giacomin, "Transport Phenomena in Eccentric Cylindrical Coordinates," PRG Report No. 024, QU-CHEE-PRG-TR--2016-24, Polymers Research Group, Chemical Engineering Dept., Queen's University, Kingston, CANADA (September, 2016), pp. 0–46.

31 Bird, R.B., R.C. Armstrong and O. Hassager, Dynamics of Polymeric Liquids, Vol. 1, 1st ed., Wiley, New York (1977).

32 Bird, R.B., R.C. Armstrong and O. Hassager, Dynamics of Polymeric Liquids, Vol. 1, 2nd ed., Wiley, New York (1987).

33 Tadmor, Z. and R.B. Bird, "Rheological Analysis of Stabilizing Forces in Wire Coating Dies," *Polymer Engineering & Science*, **14**(2), 124–136 (1974).

34 Tadmor, Z. and C.G. Gogos, Principles of Polymer Processing, Wiley-Interscience, 2nd ed., Hoboken, NJ (2006).

35 Kolitawong, C. and A.J. Giacomin, "Dynamic Response of A Shear Stress Transducer in the Sliding Plate Rheometer," *Journal of non-newtonian fluid mechanics*, **102**(1), 71–96 (2002).

36 Kolitawong, C., "Local Shear Stress Transduction in Sliding Plate Rheometry," PhD Thesis, University of Wisconsin, Mechanical Engineering Dept., University of Wisconsin, Madison, WI (December, 2002).

37 Kolitawong, C. and A.J. Giacomin, "Axial Flow between Eccentric Cylinders," *Polymer-Plastics Technology and Engineering*, **40**(3), 373–394 (2001).

Errata: in Ref. 9 and ***Table 1.***, "Buckes" should be "Guckes"; in Ref. 11 and ***Table 1.***, "1932" should be "1930"; in Ref. 11, "J. J." should be "J., J.".

38 Moon, P. and D.E. Spencer, Field Theory Handbook: Including Coordinates Systems Differential Equations and Their Solutions, Springer-Verlag, Berling, (1961).

39 Moon, P. and D.E. Spencer, Field Theory for Engineers, Van Nostrand, NJ (1961).

40 Bird, R.B., W.E. Stewart and E.N. Lightfoot, Transport Phenomena, Revised 2nd ed., Wiley & Sons, New York (2007).

41 Oldroyd, J.G., "Non-Newtonian Effects in Steady Motion of Some Idealized Elastico-Viscous Liquids," *Proceedings of the Royal Society of London*, **245**, 278–297 (1958).

42 Saengow, C., A.J. Giacomin, P.H. Gilbert and C. Kolitawong, "Reflections on Inflections," *Korea-Australia Rheology Journal*, **27**(4), 267–285 (2015). Errata: In Eq. (12), both occurrences of "$\boldsymbol{\tau}$" should be "$\mathbf{b}$".

43 Saengow, C., A.J. Giacomin, P.H. Gilbert and C. Kolitawong, "Reflections on Inflections," PRG Report No. 015, QU-CHEE-PRG-TR--2015-15, Polymers Research Group, Chemical Engineering Dept., Queen's University, Kingston, CANADA (July, 2015), pp. 0–49.

44 Giacomin, A.J., R.B. Bird, L.M. Johnson and A.W. Mix, "Large-Amplitude Oscillatory Shear Flow from the Corotational Maxwell Model," *Journal of Non-Newtonian Fluid Mechanics*, **166**(19–20), 1081–1099 (2011).

45 Saengow, C., A.J. Giacomin and C. Kolitawong, "Exact Analytical Solution for Large-Amplitude Oscillatory Shear Flow," *Macromolecular Theory and Simulations*, **24**, 352–392 (2015). Erratum: In Eqs. (47) and (48), each τ in the integrands should be τ'.

46 Saengow, C., A.J. Giacomin and C. Kolitawong, "Exact Analytical Solution for Large-Amplitude Oscillatory Shear Flow," PRG Report No. 008, QU-CHEE-PRG-TR--2014-8, Polymers Research Group, Chemical Engineering Dept., Queen's University, Kingston, CANADA (November, 2014), pp. 0–89.

47 Giacomin, A.J., C. Saengow, M. Guay and C. Kolitawong, "Padé Approximants for Large-Amplitude Oscillatory Shear Flow," *Rheologica Acta*, **54**, 679–693 (2015).

48 Giacomin, A.J., C. Saengow, M. Guay and C. Kolitawong, "Padé Approximants for Large-Amplitude Oscillatory Shear Flow," PRG Report No. 009, QU-CHEE-PRG-TR--2014-9, Polymers Research Group, Chemical Engineering Dept., Queen's University, Kingston, CANADA (November, 2014), pp. 0–37.

49 Walters, K., Rheometry, Wiley, New York (1975).

50 Tanner, R.I., Engineering Rheology, Clarendon, Oxford (1985).

51 Carreau, P.J., D.C.R. De Kee and R.P. Chhabra, Rheology of Polymeric System: Principles and Applications, Hanser, Munich (1997).

52 Agassant, J.-F., P. Avenas, J.-Ph. Sergent and P.J. Carreau, Polymer Processing: Principle and Modeling, Hanser, Munich (1991).

53 Larson, R.G., Constitutive Equations for Polymer Melts and Solutions, Butterworths, Boston (1988).

54 Barnes, H.A., J.F. Hutton and K. Walters, An Introduction to Rheology, Elsevier, Amsterdam (1989).

55 Abdel-Khalik, S.I., O. Hassager and R.B. Bird, "The Goddard Expansion and the Kinetic Theory for Solutions of Rodlike Macromolecules," *The Journal of Chemical Physics*, **61**(10), 4312–4316 (1974).

56 Bird, R.B., O. Hassager and S.I. Abdel-Khalik, "Co-Rotational Rheological Models and the Goddard Expansion," *AIChE Journal*, **20**(6), 1041–1066 (1974).

57 Bird, R.B. "A Modification of the Oldroyd Model for Rigid Dumbbell Suspensions with Brownian Motion," *Zeitschrift für angewandte Mathematik und Physik (ZAMP)*, **23**(1), 157–159 (1972).

58 Bird, R.B. and A.J. Giacomin, "Polymer Fluid Dynamics: Continuum and Molecular Approaches," *Annual Review of Chemical and Biomolecular Engineering*, **7**, 479–507 (2016).

59 Lumley, J.L., "Applicability of the Oldroyd Constitutive Equation to Flow of Dilute Polymer Solutions," *Physics of Fluids (1958-1988)*, **14**(11), 2282–2284 (1971).

60 Lumley, J.L., "Erratum: Applicability of the Oldroyd Constitutive Equation to Flow of Dilute Polymer Solutions," *Physics of Fluids (1958-1988)*, **15**(11), 2081–2081 (1972).

61 Bird, R.B., O. Hassager, R.C. Armstrong, C. Curtiss, Dynamics of Polymeric Liquids, Vol. 2, 1st ed., Wiley, New York (1977).

62 Bird, R.B. and R.C. Armstrong, "Time-Dependent Flows of Dilute Solutions of Rodlike Macromolecules," *The Journal of Chemical Physics*, **56**(7), 3680–3682 (1972).

63 Caldwell, J.J., "The Hydraulic Mean Depth as a Basis for Form Comparison in the Flow of Fluids in Pipes," *Journal of The Royal Technical College (Glasgow)*, **2**, 203–220 (1930).

64 Piercy, N.A.V., M.S. Hooper and H.F. Winny, "LIII. Viscous Flow Through Pipes with Cores," *The London, Edinburgh, and Dublin Philosophical Magazine and Journal of Science*, **15**(99), 647–676 (1933).

65 Oldroyd, J.G., "Rectilinear Plastic Flow of a Bingham Solid I. Flow Between Eccentric Circular Cylinders in Relative Motion," *Mathematical Proceedings of the Cambridge Philosophical Society*, **43**(4), 521–532 (1947).

66 Heyda, J.F., "A Green's Function Solution for the Case of Laminar Incompressible Flow Between Non-Concentric Circular Cylinders," *Journal of the Franklin Institute*, **267**(1), 25–34 (1959).

67 Berker, R. "Intégration des Équation du Movement d'un Fluide Visqueux Incompressible," *Handbuch Der Phyisik*, Stromungsmechanik II, Flugge, S., Ed. Springer-Verlag, Berlin, **VIII**/2, (1963).

68 Snyder, W.T. and G.A. Goldstein, "An Analysis of Fully Developed Laminar Flow in an Eccentric Annulus," *AIChE Journal*, **11**(3), 462–467 (1965).

69 Guckes, T.L., "Laminar Flow of Non-Newtonian Fluids in an Eccentric Annulus," *Journal of Manufacturing Science and Engineering*, **97**(2), 498–506 (1975).

70 Ballal, B.Y., and R.S. Rivlin, "Flow of a Newtonian Fluid between Eccentric Rotating Cylinders: Inertial Effects," *Archive for Rational Mechanics and Analysis*, **62**(3), 237–294 (1976).

71 Zidan, M. and A.A. Hassan, "Flow of a Viscoelastic Fluid between Eccentric Cylinders," *Rheologica acta*, **24**(2), 127–133 (1985).

72 Saengow, C., A.J. Giacomin and C. Kolitawong, "Extruding Plastic Pipe from Eccentric Dies," *Journal of Non-Newtonian Fluid Mechanics*, **223**, 176–199 (2015).

73 Saengow, C., A.J. Giacomin and C. Kolitawong, "Extruding Plastic Pipe from Eccentric Dies," PRG Report No. 011, QU-CHEE-PRG-TR--2015-11, Polymers Research Group, Chemical Engineering Dept., Queen's University, Kingston, CANADA (March, 2015), pp. 0–73.

74 Saengow, C., A.J. Giacomin and C. Kolitawong, "Knuckle Formation from Melt Elasticity in Plastic Pipe Extrusion," PRG Report No. 022, QU-CHEE-PRG-TR--2016-22, Polymers Research Group, Chemical Engineering Dept., Queen's University, Kingston, CANADA (July, 2016), pp. 1–48.

75 Gordon, R.J. and W.R. Schowalter, "Anisotropic Fluid Theory: a Different Approach to the Dumbbell Theory of Dilute Polymer Solutions," *Transactions of The Society of Rheology (1957-1977)*, **16**(1), 79–97 (1972).

76 Johnson, M.W. and D. J. Segalman, "A Model for Viscoelastic Fluid Behavior which Allows Non-Affine Deformation," *Journal of Non-Newtonian fluid mechanics*, **2**(3), 255–270 (1977).

77 Johnson, M.W. and D.J. Segalman, "Description of the Non-Affine Motions of Dilute Polymer Solutions by the Porous Molecule Model," *Journal of Non-Newtonian Fluid Mechanics*, **9**(1), 33–56 (1981).

78 Jeffreys, H., The Earth: Its Origin, History and Physical Constitution, Cambridge, London (1924).

79 Jeffreys, H., The Earth: Its Origin, History and Physical Constitution, 2nd ed., Cambridge, London (1929).

80 Williams, M.C. and R.B. Bird, "Three-Constant Oldroyd Model for Viscoelastic Fluids," *Physics of Fluids (1958-1988)*, **5**(9), 1126-1128 (1962).

81 Williams, M.C. and R.B. Bird, "Erratum: Three-Constant Oldroyd Model for Viscoelastic Fluids," *Physics of Fluids (1958-1988)*, **6**(2), 314-314 (1963).

82 Ultman, J. S. and M. M. Denn, "Slow Viscoelastic Flow Past Submerged Objects," The Chemical Engineering Journal, **2**(2), 81-89 (1971).

83 Larson, Ronald G., Constitutive Equations for Polymer Melts and Solutions: Butterworths Series in Chemical Engineering, Butterworth-Heinemann, 2013.

84 Apelian, M.R., R.C. Armstrong and R.A. Brown, "Impact of the Constitutive Equation and Singularity on the Calculation of Stick-Slip Flow: the Modified Upper-Convected Maxwell Model (MUCM)," *Journal of Non-Newtonian Fluid Mechanics*, **27**(3), 299-321 (1988).

85 Clutton, E.Q., and J.G. Williams, "On the Measurement of Residual Stress in Plastic Pipes," *Polymer Engineering & Science*, **35**(17), 1381–1386 (1995).

86 Williams, J.G., J.M. Hodgkinson and A. Gray, "The Determination of Residual Stresses in Plastic Pipe and Their Role in Fracture," *Polymer Engineering & Science*, **21**(13), 822–828 (1981).

87 Hodgkinson, J.K. and J.G. Williams, "Residual Stresses in Plastic Pipes," 5th International Conference on Deformation, Yield and Fracture of Polymers, Plastics and Rubber Institute, Cambridge, Cambridgeshire (1982), pp. 35.1–35.7.

88 Doshi, S.R., "Prediction of Residual Stress Distribution in Plastic Pipe Extrusion," *Journal of Vinyl Technology*, **11**(4), 190–194 (1989).

89 Guan, Z.W. and J.C. Boot, "A Method to Predict Triaxial Residual Stresses in Plastic Pipes," *Polymer Engineering & Science*, **44**(10), 1828–1838 (2004).

90 Pittman, J.F.T. and I.A. Farah, "A Linear Viscoelastic Model for Solid Polyethylene," *Rheologica Acta* **36**(4), 462–471 (1997).

91 Tanner, R.I. and K. Walters, Rheology: An Historical Perspective, Elsevier, Amsterdam (1998).

92 Giacomin, A.J., D.N. Githuku, K. Hartwig and K. Stanfill, "Measuring Melt Viscosity Using a Sliding Plate Rheometer with a Shear Stress Transducer," in V.K. Stokes, ed., Plastics and Plastic Composites: Material Properties, Part Performance, and Process Simulation, MD-Vol. 29, Proc., Symp. on Mechanics of Plastics and Plastic Composites, ASME Winter Annual Meeting, Atlanta, GA, 387–396 (1991).

93 Doshi, R.S., "A Novel Coextrusion Process for the Manufacture of Short Fiber-Reinforced Thermoplastic Pipe," PhD Thesis, Department of Chemical Engineering, McGill University, Montreal, Canada (1986).

94 Haberman, R., Elementary Applied Partial Differential Equations, 2nd ed., Prentice Hall, Englewood Cliffs, NJ (1987).

95 Abramowitz, M. and I.A. Stegun, Handbook of Mathematical Functions: with Formulas, Graphs, and Mathematical Tables, Vol. 55, Courier Corporation, MA (1964)

96 Osswald, T.A. and G. Menges, Materials Science of Polymers for Engineers, Hanser, Munich (1996).

97 Luo, X.L. and E.J. Mitsoulis, "Memory Phenomena in Extrudate Swell Simulations for Annular Dies," *Journal of Rheology*, **33**(8), 1307–1327 (1989).

98 Gander, W. and W. Gautschi, "Adaptive Quadrature—Revisited," *BIT Numerical Mathematics*, **40**(1), 84–101 (2000).

99 Goettler, L.A., A.J. Lambright, R.I. Leib and P.J. DiMauro, "Extrusion-Shaping of Curved Hose Reinforced with Short Cellulose Fibers," *Rubber Chemistry and Technology*, **54**(2), 277–301 (1981).

100 Goettler, L.A., R.I. Leib and A.J. Lambright, "Short Fiber Reinforced Hose-A New Concept in Production and Performance," *Rubber Chemistry and Technology*, **52**(4), 838–863 (1979).

101 Baird, D.G. and D.I. Collias, Polymer Processing: Principles and Design, John Wiley & Sons, New York (2014).

102 Denn, M.M., "Extrusion Instabilities and Wall Slip," *Annual Review of Fluid Mechanics*, **33**(1), 265–287 (2001).

103 Hade, A.J., A.J. Giacomin, J.C. Slattery and D.N. Githuku, "Postdie Extrusion of Plastic Pipe," *Polymer-Plastics Technology and Engineering*, **39**(1), 23–46 (2000).

104 Hade, A.J. and A.J. Giacomin, "Power Law Numerical Solution for Post-Die Extrusion of Plastic Pipe," *Polymer-Plastics Technology and Engineering*, **41**(1), 1–17 (2002).

105 Hade, A.J., "Modeling Free Boundary Flows in Wire Coating and Pipe Extrusion," PhD Thesis, University of Wisconsin, Mechanical Engineering Dept., University of Wisconsin, Madison, WI (2003).

Appendix I. Solving Eq. (68)

In this appendix, we will solve Eq. (68) analytically. We first recall Eq. (68):

$$\frac{\partial^2 v_0}{\partial\zeta\,\partial\zeta^*} = -\left(1-\zeta\right)^{-2}\left(1-\zeta^*\right)^{-2} \tag{68}$$

The solution to Eq. (68) has a form of:

$$v_0 = v_{0,h} + v_{0,p} \tag{222}$$

For the particular part, $v_{0,p}$, integrating Eq. (68) twice gives:

$$v_{0,p} = \frac{-1}{\left(1-\zeta\right)\left(1-\zeta^*\right)} \tag{223}$$

Substituting Eqs. (66) and (67) into Eq. (223) and using Euler Formula (see Eq. (4.3.47) in [95]):

$$e^{i\theta} = \cos\theta + i\sin\theta \tag{224}$$

gives:

$$v_{0,p} = \frac{-1}{1-2\xi\cos\theta+\xi^2} \tag{225}$$

the **second** term in Eq. (75). We then rewrite Eq. (225) as the Fourier series with respect to θ to get:

$$\begin{aligned} v_{0,p} = {} & \frac{1}{2\pi}\int_0^{2\pi}\frac{-1}{1-2\xi\cos\theta+\xi^2}d\theta \\ & + \frac{1}{\pi}\sum_{n=1}^{\infty}\int_0^{2\pi}\frac{-\cos\theta}{1-2\xi\cos\theta+\xi^2}d\theta\cos\theta + \int_0^{2\pi}\frac{-\sin\theta}{1-2\xi\cos\theta+\xi^2}d\theta\sin\theta \end{aligned} \tag{226}$$

Evaluating the integrations gives:

$$v_{0,p} = \frac{-1}{1-\xi^2} + \sum_{n=1}^{\infty}\frac{-2\xi^n}{1-\xi^2}\cos n\theta \tag{227}$$

which we will use to determine the integration constants, α_n and β_n, below.

To calculate the homogeneous part, letting the right side of Eq. (68) to zero gives:

$$\frac{\partial^2 v_0}{\partial\zeta\,\partial\zeta^*} = 0 \tag{228}$$

From Eqs. (66) and (67), solving for ξ and θ to get:

$$\xi = \sqrt{\zeta\zeta^*} \tag{229}$$

and:

$$\theta = \frac{1}{2i}\ln\frac{\zeta}{\zeta^*} \tag{230}$$

Rewriting the equation in the footnote on p. 826 in [40] for the eccentric cylindrical coordinates gives:

$$\frac{\partial}{\partial\zeta} = \frac{\partial\xi}{\partial\zeta}\frac{\partial}{\partial\xi} + \frac{\partial\theta}{\partial\zeta}\frac{\partial}{\partial\theta} \tag{231}$$

$$\frac{\partial}{\partial\zeta^*} = \frac{\partial\xi}{\partial\zeta^*}\frac{\partial}{\partial\xi} + \frac{\partial\theta}{\partial\zeta^*}\frac{\partial}{\partial\theta} \tag{232}$$

We then prepare ingredients for Eqs. (231) and (232). Differentiating Eq. (229) with respect to ζ and ζ^* gives:

$$\frac{\partial\xi}{\partial\zeta} = \frac{1}{2}\frac{\zeta^*}{\sqrt{\zeta\zeta^*}} = \frac{1}{2}e^{-i\theta} \tag{233}$$

$$\frac{\partial\xi}{\partial\zeta^*} = \frac{1}{2}\frac{\zeta}{\sqrt{\zeta\zeta^*}} = \frac{1}{2}e^{i\theta} \tag{234}$$

and Eq. (230), gives:

$$\frac{\partial\theta}{\partial\zeta}=-\frac{ie^{-i\theta}}{2\xi} \tag{235}$$

$$\frac{\partial\theta}{\partial\zeta^*}=\frac{ie^{i\theta}}{2\xi} \tag{236}$$

Substituting Eqs. (233) and (235) into Eq. (231) gives:

$$\frac{\partial}{\partial\zeta}=\frac{1}{2}e^{-i\theta}\frac{\partial}{\partial\xi}-\frac{ie^{-i\theta}}{2\xi}\frac{\partial}{\partial\theta} \tag{237}$$

and Eqs. (234) and (236) into Eq. (232) gives:

$$\frac{\partial}{\partial\zeta^*}=\frac{1}{2}e^{i\theta}\frac{\partial}{\partial\xi}+\frac{ie^{i\theta}}{2\xi}\frac{\partial}{\partial\theta} \tag{238}$$

To solve for the homogeneous part, letting the right side of Eq. (68) to zero gives:

$$\frac{\partial^2 v_{0,h}}{\partial\zeta\,\partial\zeta^*}=0 \tag{239}$$

Applying Eqs. (237) and (238) to Eq. (239) gives:

$$\frac{\partial^2 v_{0,h}}{\partial\xi^2}+\frac{1}{\xi}\frac{\partial v_{0,h}}{\partial\xi}+\frac{1}{\xi^2}\frac{\partial^2 v_{0,h}}{\partial\theta^2}=0 \tag{240}$$

The Laplacian in eccentric cylindrical coordinates is given by (see Eq. (A.7-17) of [40]):

$$\nabla^2=\frac{1}{h_\xi h_\theta}\left[\frac{\partial}{\partial\xi}\left(\frac{h_\theta}{h_\xi}\frac{\partial}{\partial\xi}\right)+\frac{\partial}{\partial\theta}\left(\frac{h_\xi}{h_\theta}\frac{\partial}{\partial\theta}\right)\right] \tag{241}$$

Substituting Eqs. (11) and (12) into Eq. (241) gives:

$$\nabla^2=\frac{\left(1+\xi^2-2\xi\cos\theta\right)^2}{a^2}\left[\frac{\partial^2}{\partial\xi^2}+\frac{1}{\xi}\frac{\partial}{\partial\xi}+\frac{1}{\xi^2}\frac{\partial^2}{\partial\theta^2}\right] \tag{242}$$

Eq. (240) thus has a form of Laplace equation in eccentric cylindrical coordinates. The solution to Eq. (240) is thus unique (see Subsection 2.5.3 in [94]) and has a form of:

$$v_{0,h} = \sum_{n=0}^{\infty} \phi_n \cos n\theta \tag{243}$$

We choose $\cos n\theta$ as basis to satisfy these two boundary conditions (x-symmetry, see Figure 4):

$$\left. \frac{\partial v_{0,h}}{\partial \theta} \right|_{\theta=0} = 0 \tag{244}$$

and:

$$\left. \frac{\partial v_{0,h}}{\partial \theta} \right|_{\theta=\pi} = 0 \tag{245}$$

Substituting Eq. (243) into Eq. (240) gives:

$$\sum_{n=0}^{\infty} \left[\phi_n'' + \frac{1}{\xi} \phi_n' - \frac{n^2}{\xi^2} \phi_n \right] = 0 \tag{246}$$

the ordinary differential equation that we will solve for ϕ_n. Solve Eq. (246) gives Eq. (76) in Subsection 4.1 above.

$$\phi_n = \begin{cases} \alpha_0 + \beta_0 \ln \xi^2 & ; n = 0 \\ 2\alpha_n \xi^n + 2\beta_n \xi^{-n} & ; n \geq 1 \end{cases} \tag{247}$$

We then determine the integration constants in Eq. (247). Substituting Eqs. (227) and (243) [together with Eq. (247)] into Eq. (222) gives:

$$v_0 = \sum_{n=0}^{\infty} \phi_n \cos n\theta + \frac{-1}{1-\xi^2} + 2\sum_{n=1}^{\infty} \frac{-\xi^n}{1-\xi^2} \cos n\theta \tag{248}$$

$$v_0 = \phi_0 + \frac{-1}{1-\xi^2} + \sum_{n=1}^{\infty} \phi_n \cos n\theta + \sum_{n=1}^{\infty} \frac{-2\xi^n}{1-\xi^2} \cos n\theta \tag{249}$$

$$v_0 = \alpha_0 + \beta_0 \ln \xi^2 + \frac{-1}{1-\xi^2} + \sum_{n=1}^{\infty} \left[2\alpha_n \xi^n + 2\beta_n \xi^{-n} + \frac{-2\xi^n}{1-\xi^2} \right] \cos n\theta \tag{250}$$

the complete solution to Eq. (68) that is subjected to:

$$v_0\left(\xi_i, \theta\right) = 0 \tag{251}$$

and:

$$v_0\left(\xi_o, \theta\right) = 0 \tag{252}$$

the boundary conditions at the inner and outer wall of the extrudate (see Figure 3). Applying Eqs. (251) and (252) into the zeroth harmonic of Eq. (250) gives:

$$0 = \alpha_0 + \beta_0 \ln \xi_i^2 + \frac{-1}{1-\xi_i^2} \tag{253}$$

$$0 = \alpha_0 + \beta_0 \ln \xi_o^2 + \frac{-1}{1-\xi_o^2} \tag{254}$$

Solving Eqs. (253) and (254) gives:

$$\alpha_0 = \frac{\xi_i^2 \ln \xi_i^2 + \ln \xi_o^2 - \xi_o^2 \ln \xi_o^2 - \ln \xi_i^2}{\left(-\ln \xi_o^2 + \xi_o^2 \ln \xi_o^2 + \ln \xi_i^2 - \xi_o^2 \ln \xi_i^2\right)\left(-1 + \xi_i^2\right)} \tag{255}$$

and:

$$\beta_0 = \frac{\xi_o^2 - \xi_i^2}{\left(-\ln \xi_o^2 + \xi_o^2 \ln \xi_o^2 + \ln \xi_i^2 - \xi_o^2 \ln \xi_i^2\right)\left(-1 + \xi_i^2\right)} \tag{256}$$

Similarly for any n- harmonic, solving Eq. (250) subjects to Eqs. (251) and (252) gives:

$$\alpha_n = \frac{\xi_i^2 \xi_o^{2n} - \xi_o^{2n} + \xi_i^{2n} - \xi_o^2 \xi_i^{2n}}{\left(\xi_o^{2n} - \xi_o^{2n+2} - \xi_i^{2n} + \xi_o^2 \xi_i^{2n}\right)\left(-1 + \xi_i^2\right)} \quad n \geq 1 \tag{257}$$

$$\beta_n = \frac{-\xi_i^n \xi_o^n \left(\xi_o^2 - \xi_i^2\right)}{\left(-\xi_o^n \xi_i^{-n} + \xi_o^{n+2} \xi_i^{-n} + \xi_o^{-n} \xi_i^n - \xi_o^{-n+2} \xi_i^n\right)\left(-1 + \xi_i^2\right)} \quad n \geq 1 \tag{258}$$

Combining Eqs. (255) with (257), and Eqs. (256) with (258) gives Eqs. (77) and (78).

Appendix II. $C_{mn,\ell}$

$$C_{12,\ell}=\left\{\begin{array}{l}\left(-8\alpha_2+6\alpha_\infty+2\alpha_1\right)_1,\left(2\beta_1-6\alpha_1+4\alpha_2\right)_2,\left(-4\beta_1-8\alpha_2+12\alpha_1\right)_3,\\ \left(-4+4\alpha_1-12\beta_1+8\beta_2\right)_4,\left(-8\beta_2+2\beta_1\right)_5\end{array}\right\} \tag{259}$$

$$C_{22,\ell}=\left\{\begin{array}{l}\left(-\tfrac{10}{3}\alpha_\infty+\tfrac{10}{3}\alpha_2\right)_1,\left(\alpha_1-4\alpha_2+3\alpha_\infty\right)_2,\left(-4\alpha_1+16\alpha_2-12\alpha_\infty\right)_3,\\ \left(-2\alpha_1+2\alpha_2-2\beta_1+2\beta_2\right)_4,\left(\beta_1-4\beta_2\right)_5,\left(4\beta_1-16\beta_2\right)_6\end{array}\right\} \tag{260}$$

$$C_{32,\ell}=\left\{\left(\tfrac{4}{3}\alpha_2-\tfrac{4}{3}\alpha_\infty\right)_1,\left(-8\alpha_2+8\alpha_\infty\right)_2\right\} \tag{261}$$

$$C_{03,\ell}=\left\{\begin{array}{l}\left(\tfrac{8}{3}\alpha_2^2-\tfrac{16}{3}\alpha_2\alpha_\infty+\tfrac{8}{3}\alpha_\infty^2\right)_1,\left(6\alpha_1\alpha_\infty+16\alpha_2^2+\alpha_1^2+9\alpha_\infty^2-8\alpha_1\alpha_2-24\alpha_2\alpha_\infty\right)_2,\\ \left(-6\alpha_\infty\beta_1+8\alpha_2\beta_1+8\alpha_2^2-16\alpha_1\alpha_2+9\alpha_1^2+8\alpha_\infty\beta_2-2\alpha_1\beta_1-8\alpha_2\beta_2\right)_3,\\ \left(8\alpha_2\beta_2-2\beta_1-8\beta_2^2+16\beta_1\beta_2+2\alpha_1\beta_1-9\beta_1^2-8\alpha_1\beta_2\right)_4,\left(8\beta_1\beta_2-16\beta_2^2-\beta_1^2\right)_5\end{array}\right\} \tag{262}$$

$$C_{13,\ell}=\left\{\begin{array}{l}\left(-10\alpha_\infty^2-\tfrac{40}{3}\alpha_2^2+\tfrac{10}{3}\alpha_1\alpha_2-\tfrac{10}{3}\alpha_1\alpha_\infty+\tfrac{70}{3}\alpha_2\alpha_\infty\right)_1,\\ \left(-7\alpha_1^2-24\alpha_2^2+32\alpha_1\alpha_2-18\alpha_1\alpha_\infty+18\alpha_2\alpha_\infty-2\alpha_2\beta_1+2\alpha_\infty\beta_1\right)_2,\\ \left(-2\alpha_1+4\alpha_1^2+4\alpha_2-4\alpha_1\alpha_2-16\alpha_2\beta_2+4\alpha_1\beta_2-8\alpha_1\beta_1+12\alpha_\infty\beta_2+8\alpha_2\beta_1\right)_3,\\ \left(-16\alpha_2\beta_1-8\alpha_1\beta_2+32\alpha_2\beta_2-24\alpha_\infty\beta_2+16\alpha_1\beta_1+8\alpha_1\alpha_2+4+4\alpha_1-8\alpha_2-8\alpha_1^2\right)_4,\\ \left(-16\alpha_1\beta_2+32\alpha_2\beta_2-24\alpha_\infty\beta_2-8\alpha_2\beta_1+16\alpha_1\beta_1-8\beta_1^2-4\beta_1+8\beta_1\beta_2\right)_5,\\ \left(24\beta_2^2+7\beta_1^2+2\alpha_1\beta_2-32\beta_1\beta_2-2\beta_2\right)_6,\left(\tfrac{40}{3}\beta_2^2-\tfrac{10}{3}\beta_1\beta_2\right)_7\end{array}\right\} \tag{263}$$

$$C_{23,\ell}=\left\{\begin{array}{l}\left(\tfrac{1}{3}\alpha_1^2+\tfrac{38}{3}\alpha_1\alpha_\infty-\tfrac{40}{3}\alpha_1\alpha_2+12\alpha_2^2-\tfrac{32}{3}\alpha_2\alpha_\infty\right)_1,\left(-\tfrac{1}{3}\beta_1^2-12\beta_2^2+\tfrac{40}{3}\beta_1\beta_2\right)_2,\\ \left(4\alpha_1\alpha_2+3\alpha_\infty\beta_1-3\alpha_1\alpha_\infty-4\alpha_2\beta_1+3\alpha_\infty+\alpha_1\beta_1-2\alpha_2-\alpha_1^2\right)_3,\\ \left(-16\alpha_1\alpha_2-12\alpha_\infty+4-12\alpha_\infty\beta_1+8\alpha_2+12\alpha_\infty\alpha_1+16\alpha_2\beta_1+4\alpha_1^2-4\alpha_1\beta_1\right)_4,\\ \left(-\beta_1^2+8\alpha_\infty\beta_2-2\alpha_1+8\alpha_2\beta_1-1+\alpha_1^2-8\alpha_1\beta_2-6\alpha_\infty\beta_1\right)_5,\\ \left(\beta_1^2+4\alpha_1\beta_2-2-\alpha_1\beta_1-4\beta_1\beta_2-2\beta_2+\beta_1\right)_6,\\ \left(16\alpha_1\beta_2+4\beta_1^2-16\beta_1\beta_2-8\beta_2+4\beta_1-4\alpha_1\beta_1\right)_7\end{array}\right\} \tag{264}$$

$$C_{33,\ell}=\left\{\begin{array}{l}\left(-2\alpha_2^2+\alpha_1\alpha_2+3\alpha_2\alpha_\infty-\alpha_1\alpha_\infty\right)_1,\left(\frac{4}{3}\alpha_2\beta_1+\frac{4}{3}\alpha_1\alpha_\infty-\frac{4}{3}\alpha_1\alpha_2-\frac{4}{3}\alpha_\infty\beta_1+\frac{2}{3}\alpha_\infty\right)_2,\\ \left(8\alpha_1\alpha_2-8\alpha_1\alpha_\infty+4-8\alpha_2\beta_1-4\alpha_\infty+8\alpha_\infty\beta_1\right)_3,\\ \left(-4\alpha_\infty\beta_1-8\alpha_2\beta_2+2\alpha_1\beta_2-\alpha_1^2-2\alpha_1\beta_1+6\alpha_\infty\beta_2-2\alpha_2+6\alpha_2\beta_1+2\alpha_1\alpha_2\right)_4,\\ \left(\beta_1^2-2+8\alpha_2\beta_2-2\beta_1\beta_2-2\alpha_2\beta_1-6\alpha_1\beta_2+2\alpha_1\beta_1\right)_5,\left(-\beta_1\beta_2+2\beta_2^2\right)_6,\\ \left(\frac{4}{3}\beta_2-\frac{4}{3}\alpha_1\beta_2+\frac{4}{3}\beta_1\beta_2-\frac{4}{3}\right)_7,\left(-8\alpha_1\beta_2+8\beta_2+8\beta_1\beta_2\right)_8\end{array}\right\} \quad (265)$$

$$C_{43,\ell}=\left\{\begin{array}{l}\left(\frac{9}{5}\alpha_\infty^2-\frac{8}{5}\alpha_\infty\alpha_2+\frac{4}{5}\alpha_2^2\right)_1,\left(\begin{array}{l}\frac{1}{3}-\frac{16}{3}\alpha_\infty\beta_2+\frac{1}{3}\alpha_1^2+\frac{16}{3}\alpha_2\beta_2-2\alpha_\infty+\frac{16}{3}\alpha_\infty\beta_1\\ -\frac{8}{3}\alpha_1\alpha_2+2\alpha_1\alpha_\infty-\frac{16}{3}\alpha_2\beta_1+\frac{4}{3}\alpha_2^2\end{array}\right)_2,\\ \left(-\frac{4}{3}\beta_2^2-\frac{16}{3}\alpha_2\beta_2-\frac{1}{3}\beta_1^2-2+\frac{16}{3}\alpha_1\beta_2+\frac{8}{3}\beta_1\beta_2\right)_3\end{array}\right\} \quad (266)$$

$$C_{53,\ell}=\left\{\begin{array}{l}\left(\alpha_1\alpha_2-2\alpha_\infty+\frac{1}{2}+3\alpha_\infty\alpha_2-\alpha_1\alpha_\infty-2\alpha_2^2\right)_1,\left(2\beta_2^2-2-\beta_1\beta_2\right)_2,\\ \left(\frac{2}{3}\alpha_2\beta_1-\frac{2}{3}-\frac{2}{3}\alpha_\infty\beta_1-\frac{8}{3}\alpha_2\beta_2+\frac{8}{3}\alpha_\infty\beta_2\right)_3,\left(-1-2\alpha_\infty\beta_2-\frac{2}{3}\alpha_1\beta_2+\frac{8}{3}\alpha_2\beta_2\right)_4\end{array}\right\} \quad (267)$$

$$C_{04,\ell}=\left\{\begin{array}{l}\left(-\frac{16}{3}\alpha_1\alpha_2^2+\frac{28}{3}\alpha_\infty\alpha_1\alpha_2-\frac{8}{3}\alpha_\infty\alpha_2^2+\frac{2}{3}\alpha_1^2\alpha_2-4\alpha_\infty^2\alpha_1+\frac{8}{3}\alpha_2^3-\frac{2}{3}\alpha_\infty\alpha_1^2\right)_1,\\ \left(\begin{array}{l}-2\alpha_1\alpha_2\beta_1-14\alpha_\infty\alpha_2\beta_1+2\alpha_\infty^2+8\alpha_2^2\beta_1-8\alpha_1\alpha_2^2-6\alpha_\infty\alpha_2-\alpha_1^3\\ +6\alpha_\infty^2\beta_1+2\alpha_\infty\alpha_1\beta_1+6\alpha_1^2\alpha_2+6\alpha_1\alpha_2\alpha_\infty-3\alpha_1^2\alpha_\infty+4\alpha_2^2\end{array}\right)_2,\\ \left(\begin{array}{l}-16\alpha_2^2\beta_2+2\alpha_1^2+2\alpha_1^2\alpha_2+16\alpha_1\alpha_2\beta_2+12\alpha_1\alpha_\infty\beta_1+16\alpha_2\alpha_\infty\beta_2-2\alpha_1^3-4\alpha_1\alpha_2\\ +2\alpha_\infty+2\alpha_\infty^2+16\alpha_2^2\beta_1-20\alpha_1\alpha_2\beta_1-2\alpha_2+4\alpha_1^2\beta_1-16\alpha_1\alpha_\infty\beta_2-12\alpha_2\alpha_\infty\beta_1\end{array}\right)_3,\\ \left(4\alpha_1-8\beta_2-12\alpha_\infty+8\alpha_2-4\beta_1\right)_4,\left(\beta_1+3\alpha_\infty-2\alpha_2-\alpha_1+2\beta_2\right)_5,\\ \left(4\alpha_1\beta_1^2-16\alpha_2\beta_2^2-2\beta_1^2+2\beta_2\beta_1^2+16\alpha_1\beta_2^2-2\beta_1^3-20\alpha_1\beta_1\beta_2+16\alpha_2\beta_1\beta_2\right)_6,\\ \left(2\beta_1\beta_2-\beta_1^3+8\alpha_1\beta_2^2+6\beta_1^2\beta_2-2\alpha_1\beta_1\beta_2-4\beta_2^2-8\beta_1\beta_2^2\right)_7,\\ \left(\frac{2}{3}\beta_1^2\beta_2-\frac{16}{3}\beta_1\beta_2^2+\frac{8}{3}\beta_2^3\right)_8\end{array}\right\} \quad (268)$$

$$C_{14,\ell}=\left\{\begin{array}{l}\left(-4\alpha_2^3-4\alpha_1\alpha_2\alpha_\infty+2\alpha_1\alpha_2^2+10\alpha_2^2\alpha_\infty+2\alpha_1\alpha_\infty^2-6\alpha_2\alpha_\infty^2\right)_1,\\ \left(\begin{array}{l}16\alpha_1\alpha_2^2+2\alpha_2\alpha_\infty+5\alpha_1^2\alpha_\infty-\frac{16}{3}\alpha_2^3+4\alpha_2^2\alpha_\infty+8\alpha_2\alpha_\infty\beta_1+\frac{1}{3}\alpha_1^3\\ +6\alpha_1\alpha_\infty^2-4\alpha_\infty^2\beta_1-20\alpha_1\alpha_2\alpha_\infty-6\alpha_1^2\alpha_2-2\alpha_\infty^2-4\alpha_2^2\beta_1\end{array}\right)_2,\\ \left(\begin{array}{l}4\alpha_1\alpha_2^2-10\alpha_1^2\alpha_2+2\alpha_\infty-4\alpha_2^2+52\alpha_2\alpha_\infty\beta_1-16\alpha_1\alpha_\infty\beta_1+24\alpha_\infty^2\beta_2\\ +3\alpha_1^3-6\alpha_1\alpha_\infty+6\alpha_1\alpha_2-18\alpha_\infty^2\beta_1-56\alpha_2\alpha_\infty\beta_2-8\alpha_1\alpha_2\beta_2-36\alpha_2^2\beta_1\\ +4\alpha_\infty^2+3\alpha_1^2\alpha_\infty-2\alpha_1^2\beta_1+8\alpha_1\alpha_\infty\beta_2+32\alpha_2^2\beta_2-2\alpha_2\end{array}\right)_3,\\ \left(\begin{array}{l}-6\alpha_\infty+4\alpha_2-24\alpha_1\alpha_\infty\beta_2+40\alpha_1\alpha_2\beta_2+2\alpha_1-16\alpha_1\alpha_2\beta_1+8\alpha_1^2\beta_1\\ +8\alpha_2^2\beta_1+24\alpha_2\alpha_\infty\beta_2-8\alpha_1^2\beta_2-32\alpha_2^2\beta_2\end{array}\right)_4,\\ \left(\begin{array}{l}-4\beta_1-8\beta_2-48\alpha_2\alpha_\infty\beta_2+32\alpha_1\alpha_2\beta_1-80\alpha_1\alpha_2\beta_2\\ +48\alpha_1\alpha_\infty\beta_2+16\alpha_1^2\beta_2+64\alpha_2^2\beta_2-16\alpha_2^2\beta_1-16\alpha_1^2\beta_1\end{array}\right)_5,\\ \left(\beta_1+3\alpha_\infty-2\alpha_2-\alpha_1+2\beta_2\right)_6,\left(18\alpha_\infty+6\beta_1-6\alpha_1-12\alpha_2+12\beta_2\right)_7,\\ \left(\beta_1+3\alpha_\infty-2\alpha_2-\alpha_1+2\beta_2\right)_8,\left(\begin{array}{l}-16\alpha_2\beta_1^2+48\alpha_\infty\beta_2^2+80\alpha_2\beta_1\beta_2-32\alpha_1\beta_1\beta_2\\ -64\alpha_2\beta_2^2+16\alpha_1\beta_2^2-48\alpha_\infty\beta_1\beta_2+16\alpha_1\beta_1^2\end{array}\right)_9,\\ \left(\begin{array}{l}-2\alpha_1\beta_1^2-36\alpha_1\beta_2^2+3\beta_1^3+2\beta_1^2+32\alpha_2\beta_2^2+4\beta_1\beta_2^2\\ -8\alpha_2\beta_1\beta_2-6\beta_1\beta_2-10\beta_1^2\beta_2+20\alpha_1\beta_1\beta_2\end{array}\right)_{10},\\ \left(\frac{1}{3}\beta_1^3-\frac{16}{3}\beta_2^3+16\beta_2^2\beta_1-6\beta_1^2\beta_2+4\beta_2^2-4\alpha_1\beta_2^2\right)_{11},\left(2\beta_1\beta_2^2-4\beta_2^3\right)_{12},\\ \left(4\alpha_\infty^2-2\alpha_\infty\right)_{13},\left(-8\alpha_\infty^2+2\right)_{14},\left(2\alpha_\infty+4\alpha_\infty^2\right)_{15}\end{array}\right\} \quad (269)$$

$$
C_{24,\ell} = \left\{
\begin{array}{l}
\left(\frac{34}{5}\alpha_2\alpha_\infty^2 - \frac{18}{5}\alpha_\infty^3 + \frac{8}{5}\alpha_2^3 - \frac{24}{5}\alpha_2^2\alpha_\infty\right)_1, \\
\left(\begin{array}{l}\alpha_1^2\alpha_2 + 8\alpha_2^3 + 10\alpha_1\alpha_2\alpha_\infty - \alpha_1^2\alpha_\infty - 3\alpha_1\alpha_\infty^3 - 2\alpha_\infty^2 - 18\alpha_2^2\alpha_\infty + 9\alpha_2\alpha_\infty^2 \\ -6\alpha_1\alpha_2^2 + 2\alpha_2\alpha_\infty\end{array}\right)_2, \\
\left(\begin{array}{l}-6\alpha_1^2\alpha_\infty - 2\alpha_2 - 16\alpha_2^2\beta_2 - 8\alpha_1\alpha_2^2 + 8\alpha_1^2\alpha_2 + 32\alpha_2\alpha_\infty\beta_2 + 4\alpha_\infty^2 \\ +4\alpha_1\alpha_2\alpha_\infty - 28\alpha_2\alpha_\infty\beta_1 - 4\alpha_1\alpha_2\beta_1 + 12\alpha_\infty^2\beta_1 - 4\alpha_2\alpha_\infty + 2\alpha_\infty \\ -\frac{2}{3}\alpha_1^3 + 16\alpha_2^2\beta_1 - 16\alpha_\infty^2\beta_2 + 4\alpha_1\alpha_\infty\beta_1 + \frac{8}{3}\alpha_2^3\end{array}\right)_3, \\
\left(\begin{array}{l}-16\alpha_1\alpha_2\beta_2 + 2\alpha_1^2\beta_2 + \alpha_1 + 2\alpha_2 - 2\alpha_1^2\beta_1 + 32\alpha_2^2\beta_2 - 3\alpha_\infty + 10\alpha_1\alpha_2\beta_1 \\ -8\alpha_2^2\beta_1 - 6\alpha_1\beta_1\alpha_\infty + 6\alpha_2\alpha_\infty\beta_1 + 12\alpha_1\alpha_\infty\beta_2 + 18\alpha_\infty^2\beta_2 \\ -48\alpha_2\alpha_\infty\beta_2\end{array}\right)_4, \\
\left(\begin{array}{l}-8\beta_2 - 4\beta_1 + 24\alpha_1\alpha_\infty\beta_1 + 64\alpha_1\alpha_2\beta_2 - 40\alpha_1\alpha_2\beta_1 + 192\alpha_2\alpha_\infty\beta_2 \\ -48\alpha_1\alpha_\infty\beta_2 + 32\alpha_2^2\beta_1 - 128\alpha_2^2\beta_2 + 8\alpha_1^2\beta_1 - 8\alpha_1^2\beta_2 - 72\alpha_\infty^2\beta_2\end{array}\right)_5, \\
\left(-\alpha_1 + 3\alpha_\infty + 2\beta_2 - 2\alpha_2 + \beta_1\right)_6, \\
\left(\begin{array}{l}14\alpha_2\beta_1^2 + 2\alpha_\infty^2 - 32\alpha_1\alpha_2\beta_2 + 4\alpha_1\beta_1\beta_2 - 32\alpha_2\beta_1\beta_2 + 28\alpha_\infty\beta_1\beta_2 \\ +14\alpha_1^2\beta_2 - 4\alpha_2\beta_1 + 16\alpha_2\beta_2^2 - 16\alpha_\infty\beta_2^2 + 4\beta_2 + 2\beta_1 - 2\alpha_1\beta_1^2 \\ -2\alpha_1^2\beta_1 + 16\alpha_2^2\beta_2 - 2\alpha_\infty - 12\alpha_\infty\beta_1^2 + 4\alpha_1\alpha_2\beta_1\end{array}\right)_7, \\
\left(\begin{array}{l}2\alpha_2\beta_1^2 + 32\alpha_2\beta_2^2 - 24\alpha_\infty\beta_2^2 - 2\alpha_1\beta_1^2 - 8\alpha_1\beta_2^2 + 6\alpha_\infty\beta_1\beta_2 + 10\alpha_1\beta_1\beta_2 \\ -16\alpha_2\beta_1\beta_2\end{array}\right)_8, \\
\left(\begin{array}{l}128\alpha_2\beta_2^2 - 8\alpha_1\beta_1^2 - 96\alpha_\infty\beta_2^2 - 32\alpha_1\beta_2^2 + 24\alpha_\infty\beta_1\beta_2 \\ -64\alpha_2\beta_1\beta_2 + 40\alpha_1\beta_1\beta_2 + 8\alpha_2\beta_1^2\end{array}\right)_9, \\
\left(-\alpha_1 + 3\alpha_\infty + 2\beta_2 - 2\alpha_2 + \beta_1\right)_{10}, \left(\begin{array}{l}-4\alpha_1\beta_1\beta_2 + 8\beta_1^2\beta_2 + \frac{8}{3}\beta_2^3 + 16\alpha_1\beta_2^2 \\ -\frac{2}{3}\beta_1^3 + 4\beta_1\beta_2 - 16\alpha_2\beta_2^2 - 8\beta_1\beta_2^2\end{array}\right)_{11}, \\
\left(-6\beta_1\beta_2^2 + \beta_1^2\beta_2 + 8\beta_2^3\right)_{12}, \left(-4\alpha_2 + 4\beta_2 + 4\alpha_\infty + 2\beta_1 - 2\alpha_1 + 2\alpha_\infty^2\right)_{13}, \\
\left(4\alpha_1 - 8\beta_2 - 6\alpha_\infty^2 + 8\alpha_2 - 4\beta_1 - 6\alpha_\infty\right)_{14}, \left(10\alpha_\infty^2 - 2\alpha_\infty\right)_{15}, \\
\left(3 - 4\alpha_1 + 4\beta_1 + 10\alpha_\infty - 8\alpha_2 - 10\alpha_\infty^2 + 8\beta_2\right)_{16}, \\
\left(-1 + 4\alpha_2 - 2\beta_1 - 6\alpha_\infty - 4\beta_2 + 2\alpha_1 + 4\alpha_\infty^2\right)_{17}
\end{array}
\right\} \quad (270)
$$

$$C_{34,\ell}=\left\{\begin{array}{l}
\left(2\alpha_2\alpha_\infty^2-2\alpha_\infty^3\right)_1,\left(\begin{array}{l}\frac{44}{5}\alpha_\infty\alpha_2^2+\frac{4}{5}\alpha_1\alpha_2^2+\frac{27}{5}\alpha_\infty^3+\frac{9}{5}\alpha_1\alpha_\infty^2-12\alpha_2\alpha_\infty^2\\+2\alpha_2\alpha_\infty-2\alpha_\infty^2-\frac{16}{5}\alpha_2^3-\frac{8}{5}\alpha_1\alpha_2\alpha_\infty\end{array}\right)_2,\\
\left(\begin{array}{l}-4\alpha_2\alpha_\infty+2\alpha_\infty-4\alpha_2^3-2\alpha_2+6\alpha_2^2\alpha_\infty\\+2\alpha_1^2\alpha_\infty+6\alpha_1\alpha_2^2-8\alpha_1\alpha_2\alpha_\infty-2\alpha_1^2\alpha_2+4\alpha_\infty^2\end{array}\right)_3,\\
\left(\begin{array}{l}\frac{8}{3}\alpha_1\alpha_\infty\beta_1-\frac{8}{3}\alpha_1\beta_2\alpha_\infty-\frac{8}{3}\alpha_2\alpha_\infty\beta_1+\frac{56}{3}\alpha_2\alpha_\infty\beta_2+\frac{4}{3}\alpha_2\\+\frac{8}{3}\alpha_1\alpha_2\beta_2-\frac{8}{3}\alpha_1\alpha_2\beta_1-2\alpha_\infty-8\alpha_\infty^2\beta_2+\frac{2}{3}\alpha_1-\frac{32}{3}\alpha_2^2\beta_2+\frac{8}{3}\alpha_2^2\beta_1\end{array}\right)_4,\\
\left(\begin{array}{l}-16\alpha_2^2\beta_1+16\alpha_1\alpha_\infty\beta_2-16\alpha_1\alpha_\infty\beta_1-16\alpha_1\alpha_2\beta_2+16\alpha_1\alpha_2\beta_1\\+64\alpha_2^2\beta_2+16\alpha_2\alpha_\infty\beta_1-8\beta_2-112\alpha_2\alpha_\infty\beta_2-4\beta_1+48\alpha_\infty^2\beta_2\end{array}\right)_5,\\
\left(-\alpha_1+3\alpha_\infty+2\beta_2-2\alpha_2+\beta_1\right)_6,\\
\left(\begin{array}{l}\frac{5}{3}\beta_1+\alpha_\infty\beta_1^2-3\alpha_\infty+2\alpha_2\beta_1-6\alpha_1^2\beta_2+36\alpha_1\alpha_2\beta_2-24\alpha_1\alpha_\infty\beta_2+\frac{10}{3}\beta_2\\+\frac{4}{3}\alpha_\infty^2+\frac{1}{3}\alpha_1-\alpha_1\beta_1^2-6\alpha_\infty\beta_1+6\alpha_\infty\alpha_1\beta_1-4\alpha_\infty\beta_1\beta_2+\frac{2}{3}\alpha_2-4\alpha_1\alpha_2\beta_1\\+4\alpha_2\beta_1\beta_2-32\alpha_2^2\beta_2+24\alpha_2\alpha_\infty\beta_2\end{array}\right)_7,\\
\left(\begin{array}{l}\frac{8}{3}\alpha_\infty^2-2\alpha_1\beta_2-32\alpha_2\beta_2^2+4\alpha_1\alpha_2\beta_2+36\alpha_2\beta_1\beta_2+32\alpha_\infty\beta_2^2-\frac{2}{3}\alpha_1\\-4\alpha_2\beta_2-6\alpha_2\beta_1^2+\frac{10}{3}\beta_2-\frac{4}{3}-\frac{1}{3}\beta_1-32\alpha_\infty\beta_1\beta_2+2\alpha_1\beta_1-4\alpha_1\beta_1\beta_2\\-\frac{4}{3}\alpha_2-\alpha_1^2\beta_1+6\alpha_\infty\beta_1^2+\frac{2}{3}\alpha_\infty\end{array}\right)_8,\\
\left(-\frac{32}{3}\alpha_2\beta_2^2+8\alpha_\infty\beta_2^2-\frac{8}{3}\alpha_1\beta_1\beta_2+\frac{8}{3}\alpha_2\beta_1\beta_2+\frac{8}{3}\alpha_1\beta_2^2\right)_9,\\
\left(16\alpha_2\beta_1\beta_2+48\alpha_\infty\beta_2^2-64\alpha_2\beta_2^2+16\alpha_1\beta_2^2-16\alpha_1\beta_1\beta_2\right)_{10},\\
\left(-\alpha_1+3\alpha_\infty+2\beta_2-2\alpha_2+\beta_1\right)_{11},\\
\left(-2\beta_1^2\beta_2+6\beta_1\beta_2^2-4\beta_2^3\right)_{12},\left(\frac{4}{5}\beta_1\beta_2^2-\frac{16}{5}\beta_2^3\right)_{13},\\
\frac{2}{3}\left(2\beta_1-2\alpha_1+4\alpha_\infty^2+4\beta_2-4\alpha_2\right)_{14},\\
\frac{2}{3}\left(4\alpha_1+8\alpha_2-1-10\alpha_\infty^2+5\alpha_\infty-4\beta_1-8\beta_2\right)_{15},\\
\frac{2}{3}\left(4\beta_2+2\beta_1-9\alpha_\infty+6\alpha_\infty^2+3-4\alpha_2-2\alpha_1\right)_{16},\\
\frac{2}{3}\left(-3+6\alpha_\infty+8\alpha_\infty^2+4\alpha_2-2\beta_1+2\alpha_1-4\beta_2\right)_{17},\\
\frac{2}{3}\left(7+4\beta_1-14\alpha_\infty^2+\alpha_\infty-4\alpha_1-8\alpha_2+8\beta_2\right)_{18},\\
\frac{2}{3}\left(-3+4\alpha_2-2\beta_1-3\alpha_\infty-4\beta_2+2\alpha_1+6\alpha_\infty^2\right)_{19}
\end{array}\right\} \quad (271)$$

$$C_{44,\ell}=\left\{\begin{array}{l}\left(2\alpha_2\alpha_\infty^2-2\alpha_\infty^3\right)_1,\left(\alpha_1\alpha_\infty^2+2\alpha_2\alpha_\infty-2\alpha_\infty^2-4\alpha_2\alpha_\infty^2+3\alpha_\infty^3\right)_2,\\ \left(\begin{array}{l}2\alpha_\infty-2\alpha_2-4\alpha_2\alpha_\infty+\frac{16}{5}\alpha_1\alpha_2\alpha_\infty+\frac{8}{5}\alpha_2^3+\frac{18}{5}\alpha_2\alpha_\infty^2-\frac{8}{5}\alpha_1\alpha_2^2\\ +4\alpha_\infty^2-\frac{16}{5}\alpha_2^2\alpha_\infty-\frac{18}{5}\alpha_1\alpha_\infty^2\end{array}\right)_3,\\ \left(\frac{1}{2}\alpha_1-\frac{3}{2}\alpha_\infty+\alpha_2\right)_4,\left(-4\beta_1-8\beta_2\right)_5,\left(-\alpha_1+3\alpha_\infty+2\beta_2-2\alpha_2+\beta_1\right)_6,\\ \left(\begin{array}{l}-\frac{2}{3}\alpha_1^2\beta_2+\frac{8}{3}\alpha_2^2\beta_1+\frac{10}{3}\beta_2+\frac{2}{3}\alpha_1^2\beta_1+\frac{40}{3}\alpha_2^2\beta_2+\frac{1}{3}\alpha_1+\frac{2}{3}\alpha_2\\ -\frac{4}{3}\alpha_1\alpha_2\beta_1-4\alpha_\infty\beta_1+\alpha_\infty^2+2\alpha_\infty\beta_1^2-2\alpha_2\beta_1^2-3\alpha_\infty-16\alpha_2\alpha_\infty\beta_2\\ +12\alpha_1\alpha_\infty\beta_2-\frac{32}{3}\alpha_1\alpha_2\beta_2+\frac{5}{3}\beta_1\end{array}\right)_7,\\ \left(\begin{array}{l}-2\alpha_2\beta_1^2+2\alpha_\infty^2-2\alpha_1\beta_1\beta_2+2\alpha_\infty\beta_1\beta_2-2\alpha_1^2\beta_2+2\alpha_2\beta_1+2\beta_2\\ -\beta_1-\frac{3}{2}+\alpha_1\beta_1^2+\alpha_1^2\beta_1-2\alpha_\infty+\alpha_\infty\beta_1^2-2\alpha_1\alpha_2\beta_1-6\alpha_\infty\beta_2\\ +6\alpha_1\alpha_\infty\beta_2\end{array}\right)_8,\\ \left(\begin{array}{l}-3+\frac{8}{3}\alpha_1\beta_2^2+\frac{40}{3}\alpha_2\beta_2^2-16\alpha_\infty\beta_2^2-\frac{4}{3}\alpha_1\beta_1\beta_2+3\alpha_\infty^2-2\alpha_1^2\beta_2+\beta_1\\ -\frac{32}{3}\alpha_2\beta_1\beta_2+4\alpha_1\beta_2-\frac{2}{3}\alpha_2\beta_1^2-2\alpha_2+\frac{2}{3}\alpha_1\beta_1^2-\alpha_1+3\alpha_\infty+12\alpha_\infty\beta_1\beta_2\end{array}\right)_9,\\ \left(-\alpha_1+3\alpha_\infty+2\beta_2-2\alpha_2+\beta_1\right)_{10},\left(-\frac{8}{5}\beta_1\beta_2^2+\frac{8}{5}\beta_2^3\right)_{11},\\ \frac{1}{2}\left(-6\alpha_\infty+6\alpha_\infty^2+2\beta_1-2\alpha_1-4\alpha_2+4\beta_2\right)_{12},\\ \frac{1}{2}\left(4\alpha_1-4\beta_1-14\alpha_\infty^2-3-8\beta_2+8\alpha_2+20\alpha_\infty\right)_{13},\\ \frac{1}{2}\left(7-18\alpha_\infty+2\beta_1+8\alpha_\infty^2-4\alpha_2-2\alpha_1+4\beta_2\right)_{14},\\ \frac{1}{2}\left(-3+2\alpha_1+14\alpha_\infty+10\alpha_\infty^2-4\beta_2+4\alpha_2-2\beta_1\right)_{15},\\ \frac{1}{2}\left(12-8\alpha_2+8\beta_2-18\alpha_\infty^2-4\alpha_1+4\beta_1-12\alpha_\infty\right)_{16},\\ \frac{1}{2}\left(-6-2\beta_1+8\alpha_\infty^2-4\beta_2+4\alpha_2+2\alpha_1+2\alpha_\infty\right)_{17}\end{array}\right\} \quad (272)$$

$$C_{54,\ell}=\left\{\begin{array}{l}
\left(2\alpha_2\alpha_\infty^2-2\alpha_\infty^3\right)_1,\left(\alpha_1\alpha_\infty^2+2\alpha_2\alpha_\infty-2\alpha_\infty^2-4\alpha_2\alpha_\infty^2+3\alpha_\infty^3\right)_2,\\
\left(-2\alpha_2+2\alpha_2\alpha_\infty^2+2\alpha_\infty-4\alpha_2\alpha_\infty-2\alpha_\infty^2\alpha_1+4\alpha_\infty^2\right)_3,\left(\frac{2}{5}\alpha_1-\frac{6}{5}\alpha_\infty+\frac{4}{5}\alpha_2\right)_4,\\
\left(-4\beta_1-8\beta_2\right)_5,\left(-\alpha_1+3\alpha_\infty+2\beta_2-2\alpha_2+\beta_1\right)_6,\\
\left(\begin{array}{l}-2\alpha_1\alpha_2\beta_2+6\alpha_2\alpha_\infty\beta_1-4\alpha_\infty\beta_1+4\alpha_2^2\beta_2+\frac{3}{10}\alpha_1+\frac{17}{5}\beta_2+2\alpha_1\alpha_\infty\beta_2-4\alpha_2^2\beta_1\\+\frac{4}{5}\alpha_\infty^2+\frac{17}{10}\beta_1+2\alpha_1\alpha_2\beta_1-6\alpha_2\alpha_\infty\beta_2+\frac{3}{5}\alpha_2-2\alpha_1\alpha_\infty\beta_1-\frac{29}{10}\alpha_\infty\end{array}\right)_7,\\
\left(\begin{array}{l}-\frac{14}{5}\alpha_\infty-\frac{20}{3}\alpha_1\alpha_2\beta_2+\frac{26}{15}\beta_2+\frac{8}{5}\alpha_\infty^2-6\alpha_\infty\beta_2-4\alpha_2\beta_1\beta_2-2\alpha_\infty\beta_1^2-\frac{1}{3}\alpha_1^2\beta_1\\+2\alpha_\infty\beta_1+4\alpha_\infty\beta_1\beta_2+\frac{8}{3}\alpha_1\alpha_2\beta_1+4\alpha_1\alpha_\infty\beta_2-2\alpha_1\alpha_\infty\beta_1+\frac{16}{3}\alpha_2^2\beta_2+2\alpha_2\beta_1^2\\+\frac{2}{15}\alpha_1-\frac{17}{15}\beta_1+\frac{4}{15}\alpha_2-\frac{4}{3}\alpha_2^2\beta_1-\frac{8}{5}+\frac{4}{3}\alpha_1^2\beta_2\end{array}\right)_8,\\
\left(\begin{array}{l}\frac{4}{3}\alpha_2\beta_1^2-\frac{2}{5}\alpha_2-\frac{18}{5}+\frac{16}{3}\alpha_2\beta_2^2+\frac{1}{5}\beta_1-\alpha_\infty\beta_1^2+4\alpha_2\beta_2+\frac{12}{5}\alpha_\infty^2-\frac{4}{3}\alpha_1\beta_2^2\\+2\alpha_1^2\beta_2-\frac{1}{3}\alpha_1\beta_1^2-\frac{3}{5}\alpha_\infty-\frac{1}{5}\alpha_1+4\alpha_\infty\beta_1\beta_2-4\alpha_1\alpha_2\beta_2+\frac{8}{3}\alpha_1\beta_1\beta_2-4\alpha_\infty\beta_2^2\\-\frac{8}{5}\beta_2-\frac{20}{3}\alpha_2\beta_1\beta_2\end{array}\right)_9,\\
\left(\begin{array}{l}-\frac{6}{5}\alpha_1+4\alpha_2\beta_2^2+\frac{16}{5}\alpha_\infty^2+\frac{6}{5}\beta_1-\frac{24}{5}+2\alpha_1\beta_1\beta_2-2\alpha_2\beta_1\beta_2+\frac{26}{5}\alpha_\infty-4\alpha_1\beta_2^2\\+\frac{12}{5}\beta_2-\frac{12}{5}\alpha_2\end{array}\right)_{10},\\
\left(-\alpha_1+3\alpha_\infty+2\beta_2-2\alpha_2+\beta_1\right)_{11},\frac{2}{5}\left(-2\alpha_1+2\beta_1-14\alpha_\infty+4\beta_2-4\alpha_2+8\alpha_\infty^2\right)_{12},\\
\frac{2}{5}\left(-6-18\alpha_\infty^2-4\beta_1+39\alpha_\infty-8\beta_2+4\alpha_1+8\alpha_2\right)_{13},\\
\frac{2}{5}\left(2\beta_1-2\alpha_1+4\beta_2-4\alpha_2+10\alpha_\infty^2+12-29\alpha_\infty\right)_{14},\\
\frac{2}{5}\left(-4\beta_2+2\alpha_1+4\alpha_2-3-2\beta_1+12\alpha_\infty^2+24\alpha_\infty\right)_{15},\\
\frac{2}{5}\left(-22\alpha_\infty^2-8\alpha_2+8\beta_2-29\alpha_\infty-4\alpha_1+18+4\beta_1\right)_{16},\\
\frac{2}{5}\left(-10-2\beta_1+9\alpha_\infty+10\alpha_\infty^2+4\alpha_2+2\alpha_1-4\beta_2\right)_{17}
\end{array}\right\} \quad (273)$$

Appendix III. $\phi'(\xi)$ and $\psi'(\xi)$

Differentiating Eqs. (76) and (93) with respect to ξ gives:

$$\phi_n' \equiv \frac{d\phi_n}{d\xi} \equiv \begin{cases} 2\beta_0 \xi^{-1} & ;\, n=0 \\ 2n\alpha_n \xi^{n-1} + 2n\beta_n \xi^{-n-1} & ;\, n \geq 1 \end{cases} \tag{274}$$

where α_n and β_n are defined in Eqs. (77) and (78), and:

$$\psi_n' \equiv \frac{d\psi_n}{d\xi} \equiv \beta_0^3 \frac{d\psi_n^{(1)}}{d\xi} + \beta_0^2 \frac{d\psi_n^{(2)}}{d\xi} + \beta_0 \frac{d\psi_n^{(3)}}{d\xi} + \frac{d\psi_n^{(4)}}{d\xi} \tag{275}$$

where:

$$\frac{d\psi_n^{(m)}}{d\xi} = \begin{cases} 2\mathrm{B}_0^{(m)} \xi^{-1} + \dfrac{dv_{1p,0}^{(m)}}{d\xi} & ;\, n=0 \quad ;\, m=1,2,3,4 \\ n\mathrm{A}_n^{(m)} \xi^{n-1} + n\mathrm{B}_n^{(m)} \xi^{-n-1} + \dfrac{dv_{1p,n}^{(m)}}{d\xi} & ;\, n \geq 1 \quad ;\, m=1,2,3,4 \end{cases} \tag{276}$$

where $A_n^{(m)}$ and $B_n^{(m)}$ are defined in Eqs. (95) and (96). The derivative of the particular parts of the first group $d\psi_n^{(1)}/d\xi$ defined in Eq. (276) are given by:

$$\frac{dv_{1p,0}^{(1)}}{d\xi} = 2\xi + 2\xi^{-3} \tag{277}$$

$$\frac{dv_{1p,1}^{(1)}}{d\xi} = -2 - 4\ln\xi + 4\xi^{-2}\ln\xi - 4\xi^{-2} \tag{278}$$

and the particular parts of the second group $d\psi_n^{(2)}/d\xi$ in Eq. (276):

$$\frac{dv_{1p,0}^{(2)}}{d\xi} = (12\alpha_2 - 12\alpha_1)\xi - (12\beta_2 - 12\beta_1)\xi^{-3} \tag{279}$$

$$\frac{dv_{1p,1}^{(2)}}{d\xi} = 3C_{12,1}\xi^2 + C_{12,2} + C_{12,3}\ln\xi + C_{12,3} - C_{12,4}\xi^{-2}\ln\xi + C_{12,4}\xi^{-2} - 3C_{12,5}\xi^{-4} \tag{280}$$

$$\begin{aligned}\frac{dv_{1p,2}^{(2)}}{d\xi} &= 4C_{22,1}\xi^3 + 2C_{22,2}\xi + 2C_{22,3}\xi\ln\xi + C_{22,3}\xi - 2C_{22,5}\xi^{-3} - 2C_{22,6}\xi^{-3}\ln\xi \\ &\quad + C_{22,6}\xi^{-3} + \tfrac{40}{3}\beta_2\xi^{-5}\end{aligned} \tag{281}$$

$$\frac{dv_{1p,3}^{(2)}}{d\xi} = 3C_{32,1}\xi^2 + 3C_{32,2}\xi^2\ln\xi + C_{32,2}\xi^2 - 24\beta_2\xi^{-4}\ln\xi + 4\beta_2\xi^{-4} \tag{282}$$

$$\frac{dv_{1p,4}^{(2)}}{d\xi} = \left(-\tfrac{4}{3}\alpha_2 + \tfrac{4}{3}\alpha_\infty\right)\xi + \tfrac{4}{3}\beta_2\xi^{-3} \tag{283}$$

where $C_{12,\ell}$, $C_{22,\ell}$ and $C_{32,\ell}$ are defined in Eqs. (259)-(261), and the particular parts of the third group $d\psi_n^{(3)}/d\xi$ in Eq. (276):

$$\frac{dv_{1p,0}^{(3)}}{d\xi} = 6C_{03,1}\xi^5 + 4C_{03,2}\xi^3 + 2C_{03,3}\xi + 4\xi^{-1} - \frac{4\xi}{\xi^2-1} - 2C_{03,4}\xi^{-3} - 4C_{03,5}\xi^{-5} + 16\beta_2^2\xi^{-7} \tag{284}$$

$$\begin{aligned}\frac{dv_{1p,1}^{(3)}}{d\xi} &= 5C_{13,1}\xi^4 + \xi^{-2}\ln\left(\xi^2-1\right)^2 - \frac{4}{\xi^2-1} - \ln\left(\xi^2-1\right)^2 - \frac{4\xi^2}{\left(\xi^2-1\right)} + 3C_{13,2}\xi^2 + C_{13,3} \\ &\quad + C_{13,4}\ln\xi + C_{13,4} + 6\xi^{-2} - C_{13,5}\xi^{-2}\ln\xi + C_{13,5}\xi^{-2} - 3C_{13,6}\xi^{-4} - 5C_{13,7}\xi^{-6}\end{aligned} \tag{285}$$

$$\begin{aligned}\frac{dv_{1p,2}^{(3)}}{d\xi} &= 4C_{23,1}\xi^3 - 4C_{23,2}\xi^{-5} + 2C_{23,3}\xi - 2\xi\ln\left(\xi^2-1\right)^2 - \frac{4\xi^3}{\left(\xi^2-1\right)} + 2C_{23,4}\xi\ln\xi + C_{23,4}\xi \\ &\quad - 2C_{23,6}\xi^{-3} + 2\xi^{-3}\ln\left(\xi^2-1\right)^2 - \frac{4}{\xi\left(\xi^2-1\right)} - 2C_{23,7}\xi^{-3}\ln\xi + C_{23,7}\xi^{-3}\end{aligned} \tag{286}$$

$$\begin{aligned}\frac{dv_{1p,3}^{(3)}}{d\xi} &= 5C_{33,1}\xi^4 - 3\xi^2\ln\left(\xi^2-1\right)^2 - \frac{4\xi^4}{\xi^2-1} + 3C_{33,2}\xi^2 + 3\xi^{-4}\ln\left(\xi^2-1\right)^2 \\ &\quad - \frac{4}{\xi^2\left(\xi^2-1\right)} + 3C_{33,3}\xi^2\ln\xi + C_{33,3}\xi^2 + C_{33,4} - C_{33,5}\xi^{-2} - 5C_{33,6}\xi^{-6} \\ &\quad - 3C_{33,7}\xi^{-4} - 3C_{33,8}\xi^{-4}\ln\xi + C_{33,8}\xi^{-4}\end{aligned} \tag{287}$$

$$\frac{dv_{1p,4}^{(3)}}{d\xi}=6C_{43,1}\xi^5+2\alpha_\infty\xi^3+4\left(4-4\alpha_\infty\right)\xi^3\ln\xi+\left(4-4\alpha_\infty\right)\xi^3-4\xi^3\ln\left(\xi^2-1\right)^2$$
$$-\frac{4\xi^5}{\xi^2-1}+2C_{43,2}\xi-2C_{43,3}\xi^{-3}+4\xi^{-5}+4\xi^{-5}\ln\left(\xi^2-1\right)^2-\frac{4}{\xi^3\left(\xi^2-1\right)}+\tfrac{24}{5}\beta_2^2\xi^{-7} \tag{288}$$

$$\frac{dv_{1p,5}^{(3)}}{d\xi}=7\alpha_\infty^2\xi^6+2\alpha_\infty\xi^4-5\xi^4\ln\left(\xi^2-1\right)^2-\frac{4\xi^6}{\xi^2-1}+5\left(4-4\alpha_\infty\right)\xi^4\ln\xi+\left(4-4\alpha_\infty\right)\xi^4$$
$$+5\xi^{-6}\ln\left(\xi^2-1\right)^2-\frac{4}{\xi^4\left(\xi^2-1\right)}+\frac{4}{\xi^6}+3C_{53,1}\xi^2-3C_{53,2}\xi^{-4}+C_{53,3}-C_{53,4}\xi^{-2} \tag{289}$$

where $C_{03,\ell}$, $C_{13,\ell}$, $C_{23,\ell}$, $C_{33,\ell}$, $C_{43,\ell}$ and $C_{53,\ell}$ in Eqs. (262)-(267), and the particular parts of the fourth group $d\psi_n^{(4)}/d\xi$ in Eq. (276):

$$\frac{dv_{1p,0}^{(4)}}{d\xi}=6C_{04,1}\xi^5+4C_{04,2}\xi^3+2C_{04,3}\xi+C_{04,4}\xi^{-1}+\frac{4C_{04,5}\xi}{\xi^2-1}-2C_{04,6}\xi^{-3}$$
$$-4C_{04,7}\xi^{-5}-6C_{04,8}\xi^{-7}+\frac{\xi+4\alpha_\infty\xi+8\alpha_\infty{}^2\xi^3-8\alpha_\infty{}^2\xi}{\left(\xi^2-1\right)^3} \tag{290}$$
$$-\frac{3\xi\left(1+\xi^2-4\alpha_\infty+4\alpha_\infty\xi^2+4\alpha_\infty{}^2\xi^4+4\alpha_\infty{}^2-8\alpha_\infty{}^2\xi^2\right)}{\left(\xi^2-1\right)^4}$$

$$\frac{dv_{1p,1}^{(4)}}{d\xi}=7C_{14,1}\xi^6+5C_{14,2}\xi^4+3C_{14,3}\xi^2+C_{14,4}+C_{14,5}\ln\xi+C_{14,5}+C_{14,6}\ln\left(\xi^2-1\right)^2$$
$$+\frac{4C_{14,6}\xi^2}{\xi^2-1}-C_{14,7}\xi^{-2}-C_{14,8}\xi^{-2}\ln\left(\xi^2-1\right)^2+\frac{4C_{14,8}}{\xi^2-1}-C_{14,9}\xi^{-2}\ln\xi+C_{14,9}\xi^{-2} \tag{291}$$
$$-3C_{14,10}\xi^{-4}-5C_{14,11}\xi^{-6}-7C_{14,12}\xi^{-8}-C_{14,13}\xi^{-2}\left(\xi^2-1\right)^{-3}-6C_{14,13}\left(\xi^2-1\right)^{-4}$$
$$+C_{14,14}\left(\xi^2-1\right)^{-3}-6C_{14,14}\xi^2\left(\xi^2-1\right)^{-4}+3C_{14,15}\xi^2\left(\xi^2-1\right)^{-3}-6C_{14,15}\xi^4\left(\xi^2-1\right)^{-4}$$

$$\frac{dv_{1p,2}^{(4)}}{d\xi} = 8C_{24,1}\xi^7 + 6C_{24,2}\xi^5 + 4C_{24,3}\xi^3 + 2C_{24,4}\xi + 2C_{24,5}\xi\ln\xi + C_{24,5}\xi$$
$$+2C_{24,6}\xi\ln\left(\xi^2-1\right)^2 + 4C_{24,6}\xi^3\left(\xi^2-1\right)^{-1} - 2C_{24,8}\xi^{-3} - 2C_{24,9}\xi^{-3}\ln\xi + C_{24,9}\xi^{-3}$$
$$-2C_{24,10}\xi^{-3}\ln\left(\xi^2-1\right)^2 + 4C_{24,10}\xi^{-1}\left(\xi^2-1\right)^{-1} - 4C_{24,11}\xi^{-5} - 6C_{24,12}\xi^{-7} - \tfrac{64}{5}\beta_2^3\xi^{-9} \qquad (292)$$
$$+\frac{6C_{24,13}\xi^5 + 4C_{24,14}\xi^3 + 2C_{24,15}\xi - 2C_{24,17}\xi^{-3}}{\left(\xi^2-1\right)^3}$$
$$\frac{-6C_{24,13}\xi^7 - 6C_{24,14}\xi^5 - 6C_{24,15}\xi^3 - 6C_{24,16}\xi - 6C_{24,17}\xi^{-1}}{\left(\xi^2-1\right)^4}$$

$$\frac{dv_{1p,3}^{(4)}}{d\xi} = 9C_{34,1}\xi^8 + 7C_{34,2}\xi^6 + 5C_{34,3}\xi^4 + 3C_{34,4}\xi^2 + 3C_{34,5}\xi^2\ln\xi + C_{34,5}\xi^2$$
$$+3C_{34,6}\xi^2\ln\left(\xi^2-1\right)^2 + 4C_{34,6}\xi^4\left(\xi^2-1\right) + C_{34,7} - C_{34,8}\xi^{-2} - 3C_{34,9}\xi^{-4}$$
$$-3C_{34,10}\xi^{-4}\ln\xi + C_{34,10}\xi^{-4} - 3C_{34,11}\xi^{-4}\ln\left(\xi^2-1\right)^2 + 4C_{34,11}\xi^{-2}\left(\xi^2-1\right)^{-1}$$
$$-5C_{34,12}\xi^{-6} - 7C_{34,13}\xi^{-8} \qquad (293)$$
$$+\frac{7C_{34,14}\xi^6 + 5C_{34,15}\xi^4 + 3C_{34,16}\xi^2 + C_{34,17} - C_{34,18}\xi^{-2} - 3C_{34,19}\xi^{-4}}{\left(\xi^2-1\right)^3}$$
$$+\frac{-6C_{34,14}\xi^8 - 6C_{34,15}\xi^6 - 6C_{34,16}\xi^4 - 6C_{34,17}\xi^2 - 6C_{34,18} - 6C_{34,19}\xi^{-2}}{\left(\xi^2-1\right)^4}$$

$$\frac{dv_{1p,4}^{(4)}}{d\xi} = 10C_{44,1}\xi^9 + 8C_{44,2}\xi^7 + 6C_{44,3}\xi^5 + 4C_{44,4}\xi^3 + 4C_{44,5}\xi^3\ln\xi + C_{44,5}\xi^3$$
$$+4C_{44,6}\xi^3\ln\left(\xi^2-1\right)^2 + 4C_{44,6}\xi^5\left(\xi^2-1\right)^{-1} + 2C_{44,7}\xi - 2C_{44,9}\xi^{-3}$$
$$-4C_{44,10}\xi^{-5}\ln\left(\xi^2-1\right)^2 + 4C_{44,10}\xi^{-3}\left(\xi^2-1\right)^{-1} - 6C_{44,11}\xi^{-7} \qquad (294)$$
$$+\frac{8C_{44,12}\xi^7 + 6C_{44,13}\xi^5 + 4C_{44,14}\xi^3 - 2C_{44,16}\xi^{-3} - 4C_{44,17}\xi^{-5} - 6\xi}{\left(\xi^2-1\right)^3}$$
$$+\frac{-6C_{44,12}\xi^9 - 6C_{44,13}\xi^7 - 6C_{44,14}\xi^5 - 6C_{44,15}\xi - 6C_{44,16}\xi^{-1} - 6C_{44,17}\xi^{-3} + 18\xi^3}{\left(\xi^2-1\right)^4}$$

$$\frac{dv_{1p,5}^{(4)}}{d\xi} = 11C_{54,1}\xi^{10} + 9C_{54,2}\xi^{8} + 7C_{54,3}\xi^{6} + 5C_{54,4}\xi^{4} + 5C_{54,5}\xi^{4}\ln\xi + C_{54,5}\xi^{4}$$
$$+5C_{54,6}\xi^{4}\ln\left(\xi^{2}-1\right)^{2} + 4C_{54,6}\xi^{6}\left(\xi^{2}-1\right)^{-1} + 3C_{54,7}\xi^{2} + C_{54,8} - C_{54,9}\xi^{-2}$$
$$-3C_{54,10}\xi^{-4} - 5C_{54,11}\xi^{-6}\ln\left(\xi^{2}-1\right)^{2} + 4C_{54,11}\xi^{-4}\left(\xi^{2}-1\right)^{-1} \tag{295}$$
$$+\frac{9C_{54,12}\xi^{8} + 7C_{54,13}\xi^{6} + 5C_{54,14}\xi^{4} - C_{54,15}\xi^{-2} - 3C_{54,16}\xi^{-4} - 5C_{54,17}\xi^{-6} - \frac{18}{5}\xi^{2} - \frac{6}{5}}{\left(\xi^{2}-1\right)^{3}}$$
$$+\frac{-6C_{54,12}\xi^{10} - 6C_{54,13}\xi^{8} - 6C_{54,14}\xi^{6} - 6C_{54,15} - 6C_{54,16}\xi^{-2} - 6C_{54,17}\xi^{-4} + \frac{36}{5}\xi^{4} + \frac{36}{5}\xi^{2}}{\left(\xi^{2}-1\right)^{4}}$$

where $C_{04,\ell}$, $C_{14,\ell}$, $C_{24,\ell}$, $C_{34,\ell}$, $C_{44,\ell}$ and $C_{54,\ell}$ in Eqs. (268)-(273).

Appendix IV. Relationship between θ and $\tilde{\theta}$

In this appendix, we derive the relationship between the cylindrical angular, $\tilde{\theta}$ and eccentric cylindrical angular coordinates θ. We begin by relating the Cartesian coordinate x in Figure 4 (to which the eccentric cylindrical coordinates are referred) with the Cartesian coordinate $\tilde{x}$ in Figure 8 (to which the cylindrical coordinates are referred):

$$x = \tilde{x} + x_c \tag{296}$$

where the circle center is given by $x_c = a/\left(1-\xi^2\right)$ (from Eq. (6) of [72]).

Substituting this into Eq. (296) gives:

$$x = \tilde{x} + \frac{a}{1-\xi_o^2} \tag{297}$$

where (see Eq. (A.6-1) in [40]):

$$\tilde{x} \equiv r\cos\tilde{\theta} \tag{298}$$

Substituting Eqs. (1) and (298) into Eq. (297), and solving for θ gives:

$$\theta = \arccos\left(\frac{\left(1+\xi^2\right)\left(\frac{R}{a}\cos\tilde{\theta}+\frac{1}{1-\xi^2}\right)-1}{2\xi\left(\frac{R}{a}\cos\tilde{\theta}+\frac{1}{1-\xi^2}\right)-\xi}\right) \tag{299}$$

Since the origin of the cylindrical coordinates is at the outer circle center, Eq. (299) becomes:

$$\theta = \arccos\left(\frac{\left(1+\xi_o^2\right)\left(\frac{R_o}{a}\cos\tilde{\theta}+\frac{1}{1-\xi_o^2}\right)-1}{2\xi_o\left(\frac{R_o}{a}\cos\tilde{\theta}+\frac{1}{1-\xi_o^2}\right)-\xi_o}\right) \tag{300}$$

or for $\tilde{\theta}$:

$$\tilde{\theta} = \arccos\left(\frac{a}{R_o} \frac{1 - \xi_o \cos\theta}{1 - 2\xi_o \cos\theta + \xi_o^2} - \frac{a}{R_o} \frac{1}{1 - \xi_o^2} \right) \tag{301}$$

Eqs. (300) [Eq. (301)] can be used to convert from θ to $\tilde{\theta}$ [*vice versa*].